ISSN 0352-9045

Informacije MIDEM

Journal of Microelectronics, Electronic Components and Materials
Vol. 52, No. 1(2022), March 2022

Revija za mikroelektroniko, elektronske sestavne dele in materiale
letnik 52, številka 1(2022), Marec 2022

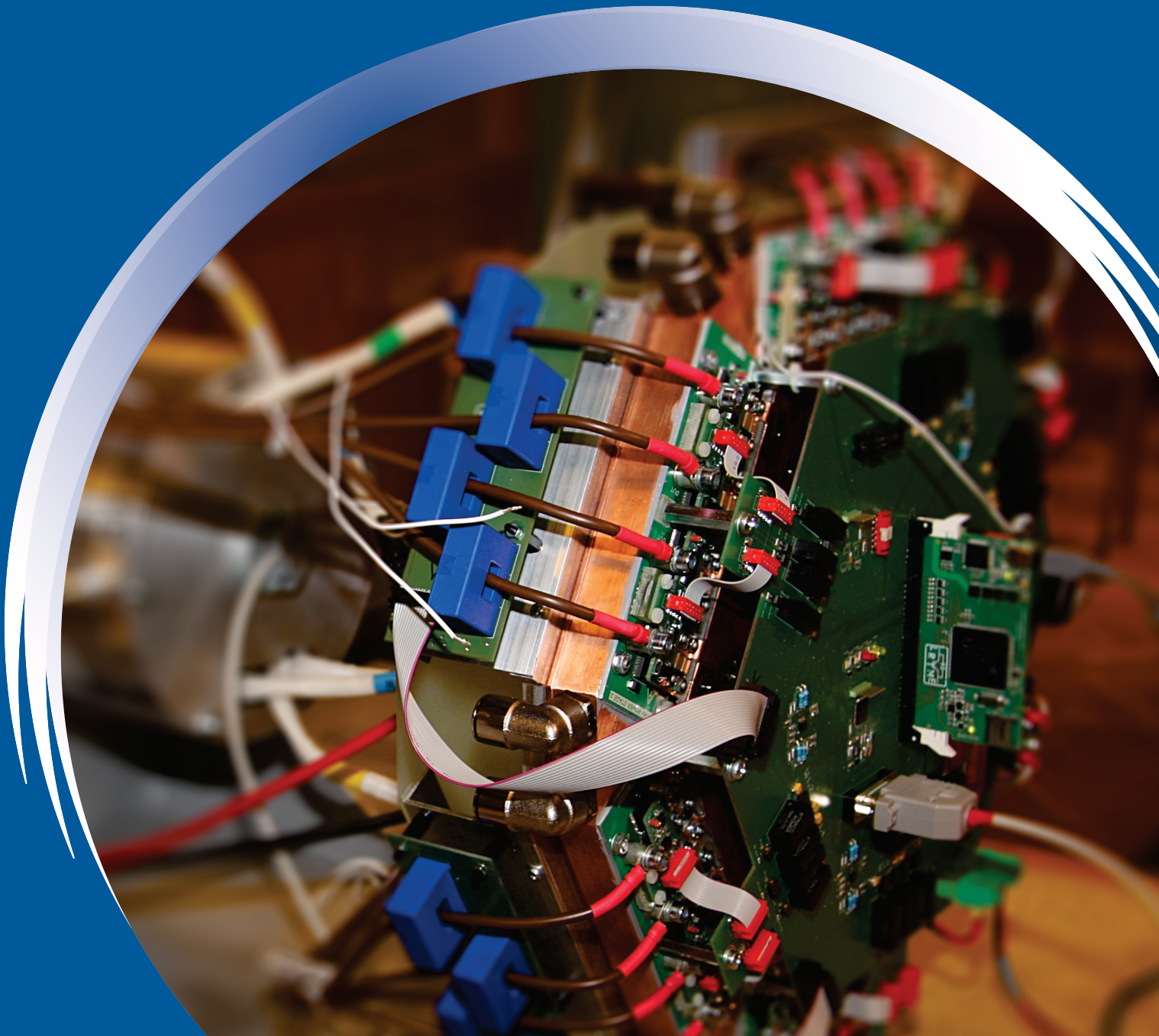

UDK 621.3:(53+54+621+66)(05)(497.1)=00 ISSN 0352-9045

Informacije MIDEM *1-2022*

Journal of Microelectronics, Electronic Components and Materials

VOLUME 52, NO. 1(181), LJUBLJANA, MARCH 2022 | LETNIK 52, NO. 1(181), LJUBLJANA, MAREC 2022

Published quarterly (March, June, September, December) by Society for Microelectronics, Electronic Components and Materials - MIDEM.

Headquarters | Naslov uredništva
Uredništvo Informacije MIDEM
MIDEM pri MIKROIKS
Stegne 11, 1521 Ljubljana, Slovenia
T. +386 (0)1 513 37 68
F. + 386 (0)1 513 37 71
E. info@midem-drustvo.si
www.midem-drustvo.si

Annual subscription rate is 160 EUR, separate issue is 40 EUR. MIDEM members and Society sponsors receive current issues for free. Scientific Council for Technical Sciences of Slovenian Research Agency has recognized Informacije MIDEM as scientific Journal for microelectronics, electronic components and materials. Publishing of the Journal is cofinanced by Slovenian Research Agency and by Society sponsors. Scientific and professional papers published in the journal are indexed and abstracted in COBISS and INSPEC databases. The Journal is indexed by ISI® for Sci Search®, Research Alert® and Material Science Citation Index™. |
Letna naročnina je 160 EUR, cena posamezne številke pa 40 EUR. Člani in sponzorji MIDEM prejemajo posamezne številke brezplačno. Znanstveni svet za tehnične vede je podal pozitivno mnenje o reviji kot znanstveno-strokovni reviji za mikroelektroniko, elektronske sestavne dele in materiale. Izdajo revije sofinancirajo ARRS in sponzorji društva. Znanstveno-strokovne prispevke objavljene v Informacijah MIDEM zajemamo v podatkovne baze COBISS in INSPEC. Prispevke iz revije zajema ISI® v naslednje svoje produkte: Sci Search®, Research Alert® in Materials Science Citation Index™.

Design | Oblikovanje: Snežana Madić Lešnik; Printed by | tisk: Biro M, Ljubljana; Circulation | Naklada: 1000 issues | izvodov; Slovenia Taxe Percue | Poštnina plačana pri pošti 1102 Ljubljana

Informacije MIDEM
Journal of Microelectronics,
Electronic Components and Materials
vol. 52, No. 1(2022)

Content | Vsebina

Original scientific papers | Izvirni znanstveni članki

Editorial | Uvodnik

Dear reader,

Isn't it amazing how time flies? Another covid-19 year is around, another year of restrictions and limitations both in private life as well as in professional life including science. For our journal it was quite a regular year. All operations and processes ran smoothly and I am grateful to EB members, reviewers and technical support team for their valuable contribution to the success. All papers published are open-access and accessible in WoS, Scopus, DOAJ or on the journal web pages by a single mouse click. Do open-access papers help us in wider dissemination and larger readership? We are tracking the numbers and the trends look promising.

In 2021 we received more than 141 manuscripts, out of which only 22 have been accepted for publication so far, while 25 were out of scope and 56 manuscripts were rejected. The success rate remains low (below 20% in 2021) primarily because we receive many manuscripts that do not meet the quality and scientific originality that we aim at. Citation metrics with JCR IF-2020=0.442, SNIP-2020=0.284 and CiteScore-2020=0.80 is an important performance indicator. In 2021 we published 2 review scientific papers (on microfluidics and on nanotechnology and nanoscience) and 22 original scientific papers.

We commit ourselves to continue serving you as a part of your success in science and engineering and look forward to receiving your future manuscript(s) on our submission page (http://ojs.midem-drustvo.si/).

Stay safe and healthy!

Prof. Marko Topič
Editor-in-Chief

23 March 2022

Original scientific paper
https://doi.org/10.33180/InfMIDEM2022.101

Informacije MIDEM
Journal of Microelectronics,
Electronic Components and Materials
Vol. 52, No. 1(2022), 3 – 9

Design and optimization of a microfluidic-based inductor used as a multifunction-sensor

Nizar Habbachi[1], Hatem Boussetta[1], Mohamed Adel Kallala[1], Kamel Besbes[1,2]

[1]Microelectronics and Instrumentation Laboratory, University of Monastir, Tunisia.
[2]Center for Research on Microelectronics Nanotechnology, CRMN Sousse TechnoPark.

Abstract: A planar miniaturized inductor has been designed in order to realize some transduction functions linked to the presence of fluids. Its electrical behavior has been studied for two liquids: Galinstan (an alloy of GALium INdium STANum) and salted water. Their presence between metallic armatures modifies the inductance value at a nominal frequency, chosen at 2GHz. By using a FEM software, the spatial distributions of magnetic field and surface current density in the entire device have been modelized for six arbitrary positions of these liquids in inductor microchannels. The geometrical aspects of the device have been studied and their influence examined for each liquid. We show that the inductor performances are influenced by the spiral width variations and the inter-turn distances of the coil. Considering the device as a sensor, we have evaluated the variations of two parameters: inductance and quality factors, which can respectively attain 664% (for Galinstan) and 175% (for salted water) from their nominal values.

Keywords: Variable inductor; sensor; micro-fluids

Zasnova in optimizacija mikrofluidne tuljave za večfunkcijski senzor

Izvleček: Zasnovana je bil planarna miniaturna tuljava, ki omogoča izvajanje nekaterih prenosnih funkcij, povezanih s prisotnostjo tekočin. Njeno električno obnašanje je bilo preučeno za dve tekočini: Galinstan (zlitina GALija INdija in STANija) in slano vodo. Njuna prisotnost med kovinskimi armaturami spremeni induktivnost pri izbrani nazivni frekvenci (2 GHz). S programsko opremo FEM so bile modelirane prostorske porazdelitve magnetnega polja in gostote površinskega toka v celotni napravi za šest poljubnih položajev teh tekočin v mikrokanalih tuljave. Preučeni so bili geometrijski vidiki naprave in njihov vpliv za vsako tekočino. Pokazalo se je, da na delovanje tuljave vplivajo spremembe širine spirale in razdalje med zavoji navitja. Če napravo obravnavamo kot senzor, smo ocenili spremembe dveh parametrov: induktivnosti in faktorjev kakovosti, ki lahko dosežejo 664% (za Galinstan) oziroma 175% (za slano vodo) svojih nazivnih vrednosti.

Ključne besede: spremenljiva tuljava; sensor; mikrofluidika

** Corresponding Author's e-mail: habbachinizar@yahoo.fr*

1 Introduction

In the large domain of instrumentation, particularly those devoted to the high-frequency spectrum it is necessary to conduct studies in order to develop components, circuits and systems whose characteristics will be used for different applications. Among the passive electronic components, the inductor is largely used in the communication domains, particularly those developed by using microsystem technologies. The objective of this miniaturization is twofold: integration and parameterization of the different operating modes linked to a given application. In the field of RF applications, like those researched in embedded electronics, the need for continuously variable micro-nano devices is crucial [1-3].

In the continuity of our previous works on MEMS devices, particularly those using 'microfluidic technology', we propose, by using FEM software, a modeling approach to design and optimize a variable micro-in-

How to cite:
N. Habbachi et al., "Design and optimization of a microfluidic-based inductor used as a multifunction-sensor", Inf. Midem-J. Microelectron. Electron. Compon. Mater., Vol. 52, No. 1(2022), pp. 3–9

ductor. The inductance variations can be based on the dielectric properties of fluids and their positions in the inner channel constructed between the metallic armatures of the device. This choice, based on previously realized devices, will constitute the transducer element used not only in continuously variable electronic components, but also as a multifunction's sensor.

The choice of conductive liquid is important, especially for RF applications: 'metal' liquids are appropriate due to their high electrical conductivity, their held at high temperatures, supporting hence high electric power, and providing low losses. However, the high melting temperature of metals (~1000 °C for gold and ~660 °C for aluminum) presents a real obstacle prohibiting their exploitation in microfluidic systems. GALINSTAN (GALium INdium STANum) has attractive characteristics: low melting temperature -19°C, high electrical conductivity σ = 3.46 106 S/m. Galinstan has become the most widely used metallic conductive liquid in radio-frequency applications such as: antennas, RF filters, and RF switches [4-10]. There are other possible alternatives to Galinstan, e.g. "Gallium-Indium-Tin (GaInSn) alloy", with similar properties and would presumably perform similarly to Galinstan. Other, low or non-conductive liquids like Ethanol and similar would not affect the behavior of the inductor very much and would therefore not be a good choice.

We have focalized our study on the behavior of a 6 turns coil inductor incorporating 3-turns microfluidic channels partially or totally filled with liquids [11-14].

Two liquids have been tested, saturated saline water (357 g/L), and Galinstan, chosen for their particular dielectric properties. By modifying their quantity present in the channels, the core permeability will be modified, given hence noticeable variations of the nominal value of inductance. Their presence and positions in the channel should modify the distributions of the magnetic field and electric current density, giving indirect information on the nature of the liquid, and/or the parts of the channel containing air or liquid and their spatial repartitions.

On another hand, in order to assure the inclusion of the device as an active element of an RF circuit, we choose to operate at 2 GHz (resonant frequency of the microfluidic inductor). A frequency conversion, by means of a passive resonator containing the liquid-based inductor, allows to use it in applications associating tuning/sensing or quality factor.

2 Microfluidic inductor as a sensor

2.1 Variation principle

The projected device is based on a miniaturized coil used as a micro-sensor. Its schematic principle is represented in Fig. 1: it has a dual system of channels in which a microfluid can circulate, occupying partially or totally the space between metallic plots, called 'spiral 1' and 'spiral 2'.

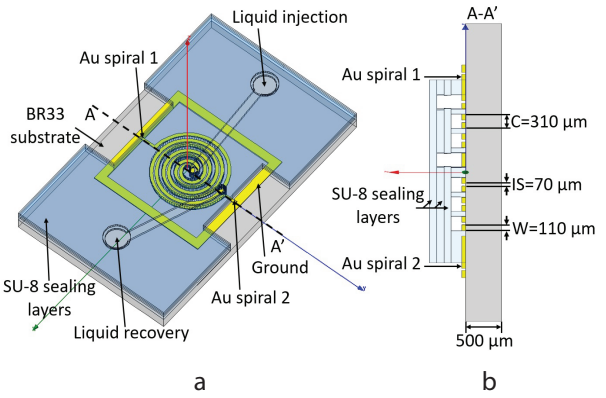

Figure 1: A five-turns MEMS microfluidic inductor: (a) 3D view perspective (b) cross-section.

The particular dielectric properties of fluids and their positions in the channel (between 'injection hole' and 'exit hole') will be chosen according to the device's intended use. As can be seen in equation (1), the intrinsic value of the inductance L is affected not only by its dimensions (length l, number of spires N, and surface S) but also by the permeability μ_r of the fluid present in the channel:

$$L = \mu_0 \mu_r N^2 S/l \quad (1)$$

The dielectric properties of liquid and air in the channel modify the electrical behavior of the inductance. Also, by aging on the fluid circulating or positioned in different parts of the channel, it will be possible to use the device as a sensor not only to detect the presence or absence of fluids/air, but equally to indicate the respective position of each of them.

Consequently, the electric current distribution in spirals is affected by the presence or absence of liquid between the channel.

2.2 Design characteristics

The cross-section of the device (Fig. 1(b)) shows different elements constituting the inductor: spiral-shaped channels designed by using the photosensitive polymer SU8 [14,15], with gold electrodes; these elements are disposed on a dielectric glass substrate Borofloat 33 [14,15]. This insolating support is used instead of common substrate

for its good RF characteristics such as a low relative permittivity ε = 4.6 and an almost zero dielectric loss (tanδ = 0.0037); the choice of Au for metallic lines is based on its resistance to corrosion and its high electrical conductivity (σ = 41.106 S/m). Furthermore, the liquid is in direct contact with the inductor core, therefore, we use Deionized water before new measurements in order to clean microfluidic channels from some saltwater residual parts.

3 Theoretical approach

Used as a sensor, this passive electrical component will be necessary in physical contact with liquid samples [15-18]. In order to predict its electrical behavior or its performances for a particular use, it is necessary to study some parameters like the magnetic field distribution and current density in the channel for a particular liquid, Galinstan (σ = 3.46 10^6 S/m) [21-23].

3.1 Spatial distribution of magnetic field lines

We have studied the spatial distribution of the magnetic field for six Galinstan positions in the channel: different results obtained at 2 GHz excitation frequency are reported in Fig. 2.

As shown in Fig. 2 (a), when the microfluidic channel is empty, magnetic field lines cover the entire coil surface with an almost uniform distribution. The insertion of conductive liquid between inductor turns will gradually and continuously change the magnetic field distribution. The first position presented in Fig. 2 (b) shows the absence of magnetic field lines in the inductor center. With Galinstan displacement from POS1 to POS6, the field lines will be canceled on the entire surface occupied but their level increases more near the ground (Fig. 2(e-f)). When the channel is completely filled with Galinstan, Fig. 2 (g) shows that the magnetic field is completely removed from the winding; it is maximum elsewhere.

3.2 Surface electric current density

We also studied the change of electric current density on the micro-inductor caused by the Galinstan displacements. The results are summarized in Fig. 3 for six positions.

When the inductor is empty (Fig. 3 (a)), the electric current density is maximum at the inductor center. On the other hand, the current value is low in the last coil turn and it is almost zero at the ground. This result explains the presence of magnetic field lines in inductor winding and its absence next to the ground when it is empty (Fig. 2 (a)). For the first position of Galinstan (Fig. 3 (b)), we notice that the current density is almost zero in the area occupied by the conductive liquid. This result shows that the Galinstan penetration decreases the inductor current path surface: consequently, the inductance value decreases. Also, this result corroborates the cancellation of magnetic field lines observed in Fig. 2 (b). In Fig. 3 we can observe that if the penetration of the fluid is continuing from POS2 to POS6, the current distribution decreases more and more in the parts occupied by Galinstan.

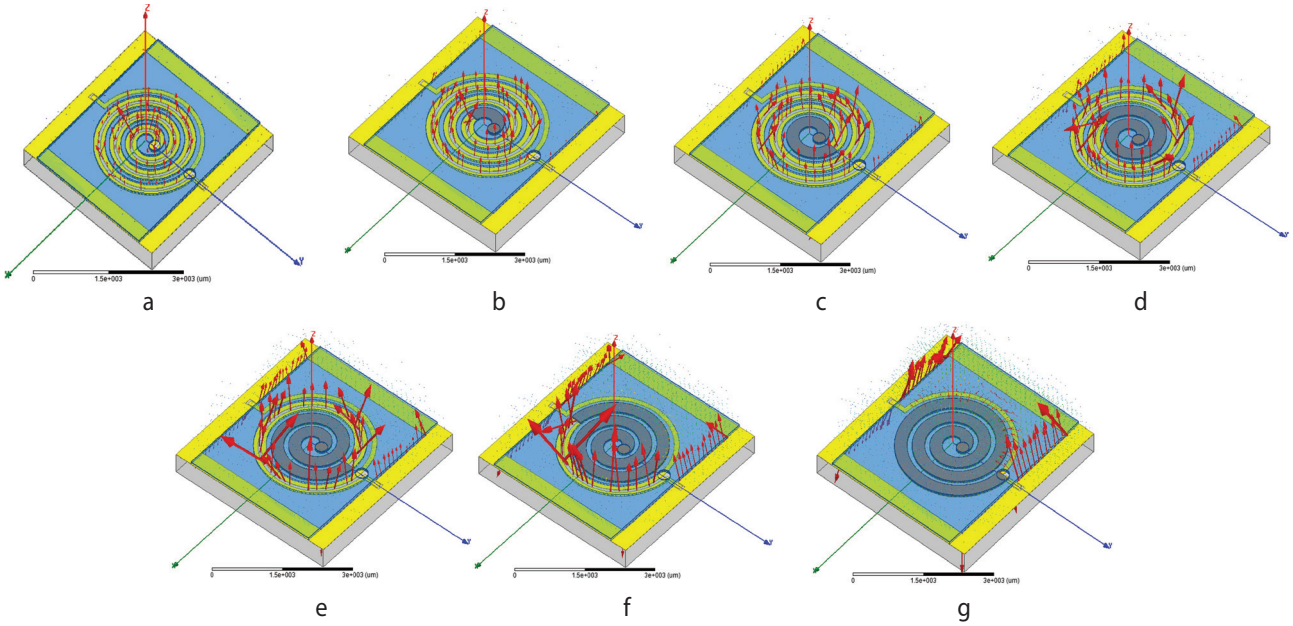

Figure 2: Magnetic field lines distribution for six arbitrary positions of Galinstan in the inductor channel: (a) no liquid (b) POS1 (c) POS2 (d) POS3 (e) POS4 (f) POS5 (g) POS6.

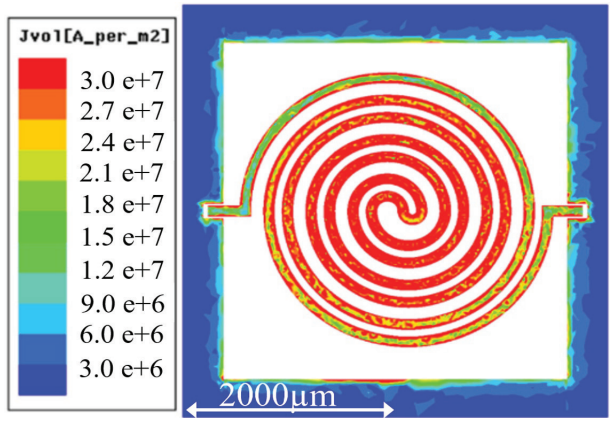

a

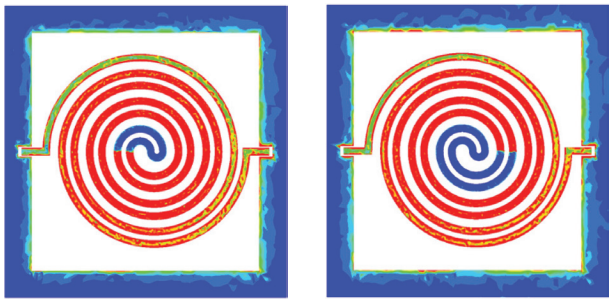

b c

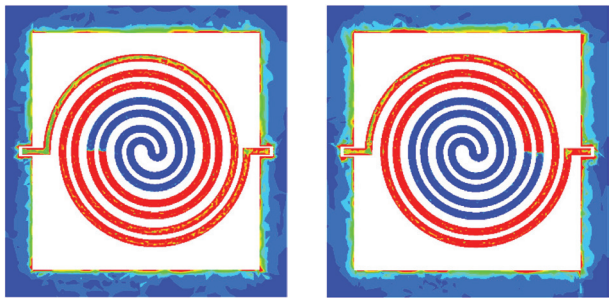

d e

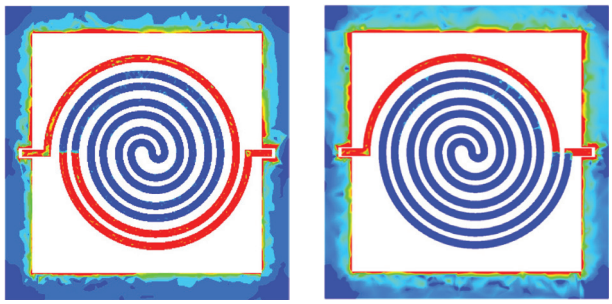

f g

Figure 3: Distribution of the electric current density for the six positions of Galinstan in the channel: (a) no liquid (b) POS1 (c) POS2 (d) POS3 (e) POS4 (f) POS5 (g) POS6.

4 Principal performances indicators

We also checked the double spiral geometric parameters variations and study their effects on the inductor performances when the microchannel is empty and when it is completely filled with Galinstan. We have applied our model to another liquid, salted water (σ = 75 S/m, when saturated), in order to study the device performances. We have varied the inter-spacing "IS" (Fig. 1(b)) from IS = 10 µm to IS = 70 µm with a step of 10 µm; and at each value of IS we change spiral width, from W = 10 µm to W = 110 µm.

4.1 Inductance value variations

For each geometric value (couple of parameters IS and W), we calculated the difference between the inductance value when it is empty and when it is fully filled with respectively Galinstan and salted water. The principal results giving the inductance variations are represented in Fig. 4: the tuning range is calculated at 2 GHz frequency.

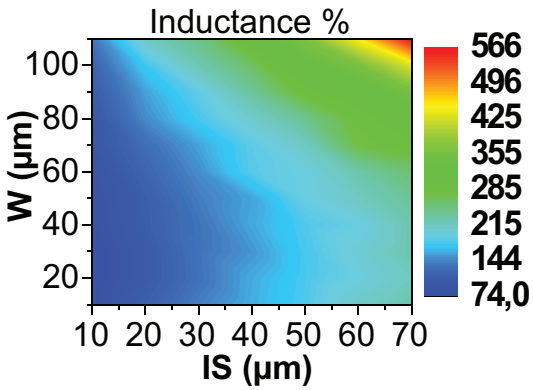

a

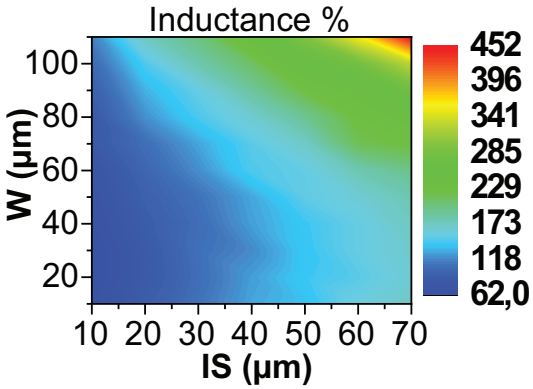

b

Figure 4: Tuning range parameters versus geometrical parameters of the inductor when the channel is fully filled with: (a) Galinstan (b) salted water.

Fig. 4 shows that the maximum tuning range is obtained for IS = 70 µm and W = 110 µm regardless of liq-

uid. In Fig. 4 (a) we note that the tuning range is comprised between Tr = 74 % and Tr = 566 % leading to a large sensitivity of 664.8 % for Galinstan. From Fig. 4 (b), the tuning range is comprised between Tr = 62 % and Tr = 452 %, for a sensitivity of 629 % when the inductor is fully filled with salted water. These results demonstrate the large tunability of the inductor and its high sensitivity to geometric variations for these two liquids.

4.2 Quality factor variation

The quality factor represents the ratio between total coil energy and dissipated energy during one cycle, we have evaluated it at 2 GHz. The results are reported in Fig. 5. for the two liquids:

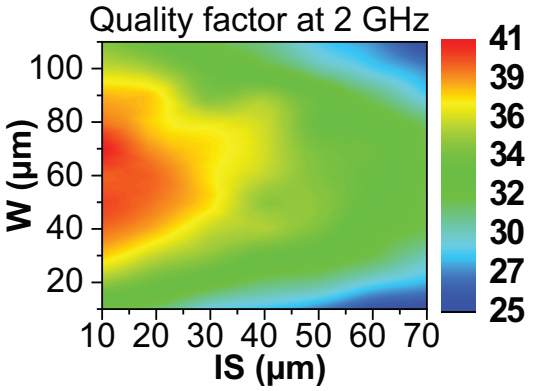

a

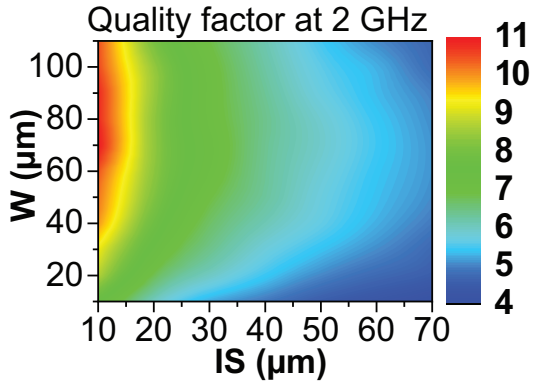

b

Figure 5: Quality factor of the inductor and its dependence on geometrical parameters "IS" and "W" when the microchannel is fully filled with: (a) Galinstan (b) salted water.

Fig. 5 (a) shows that the presence of Galinstan induces a high-quality factor for the device: it can reach Q = 41 at 2 GHz. Nevertheless, the red region area decreases and is affected by the parameter IS until a value of 30 µm. By comparing the effects of the two liquids, we observe that the quality factor values are comprised between Q_{min} = 25 and Q_{max} = 41 and between Q_{min} = 4 and Q_{max} = 11 respectively for Galinstan (Fig. 5 (a)) and salted water (Fig. 5 (b)). Quality factor values provided by salted water are significantly higher sensitive (175%) than those obtained with Galinstan (64%). We can conclude that the quality factor parameter could categorize liquids and demonstrate the multi-sensing behavior of the microfluidic inductor. Hence, the high electric conductivity liquid allows a significant improvement for the microfluidic inductor quality factor, which is moreover an essential parameter for RF applications.

5 Conclusion

An inductor based on microfluidic actuation has been studied in order to be used as a multifunctional device, able to be included in an embedded electronic circuit. It has been designed to allow the displacement of fluids, Galinstan and salted water, between the frames of a spiral coil. We have shown that their electrical (or dielectric) properties can modify not only the electromagnetic distribution in the channel, but also the influence of geometrical parameters of the channel on them: each of these aspects makes it is possible to foresee a use as a sensor for different liquids and their characteristics.

On the first hand, it has been shown that the metallic liquid Galinstan influences the magnetic field distribution and therefore the total energy stored in the coil.

Another liquid, salted water, has been tested in the model: its presence modifies the electric field distribution and consequently the coupling between two spirals of the microfluidic inductor.

The global results reveal that the electrical performances of this device are influenced differently not only by the nature of fluids or their positions in the channel, but also by the geometrical parameters of the device. This opens up the prospect of using it as a multifunctional sensor that can be integrated into an instrument circuit operating at RF frequencies.

6 Conflict of Interest

The authors declare that there is no conflict of interest for this paper. Also, there are no funding supports for this manuscript.

7 References

1. J. Kim, and D. Peroulis, "Tunable MEMS Spiral Inductors With Optimized RF Performance and Integrated Large-Displacement Electrothermal Actu-

ators", *IEEE Transactions on Microwave Theory and Techniques*, vol. 57, no. 9, pp. 2276-2283, 2009. https://doi.org/10.1109/tmtt.2009.2027153
2. S. Chang, and S. Sivoth, "A Tunable RF MEMS Inductor on Silicon Incorporating an Amorphous Silicon Bimorph in a Low-Temperature Process", *IEEE Electron Device Letters*, vol. 27, no. 11, pp. 905-907, 2006. https://doi.org/10.1109/led.2006.884712
3. B. Assadsangabi, M. Mohamed Ali and K. Takahata, "Planar Variable Inductor Controlled by Ferrofluid Actuation", IEEE Transactions on Magnetics, vol. 49, no. 4, pp. 1402-1406, 2013. https://doi.org/10.1109/tmag.2012.2228212
4. A. Pourghorban Saghati, J. Singh Batra, J. Kameoka and K. Entesari, "Miniature and Reconfigurable CPW Folded Slot Antennas Employing Liquid-Metal Capacitive Loading", IEEE Transactions on Antennas and Propagation, vol. 63, no. 9, pp. 3798-3807, 2015. https://doi.org/10.1109/tap.2015.2447002
5. M. Wang, C. Trlica, M. Khan, M. Dickey and J. Adams, "A reconfigurable liquid metal antenna driven by electrochemically controlled capillarity", Journal of Applied Physics, vol. 117, no. 19, p. 194901, 2015. https://doi.org/10.1063/1.4919605
6. D. Diedhiou, O. de Sagazan, R. Sauleau, and A. Boriskin, "Contactless Microstrip Transition for Flexible Microfluidic Circuits and Antennas", IEEE Antennas and Wireless Propagation Letters, vol. 14, pp. 1502-1505, 2015. https://doi.org/10.1109/lawp.2014.2367811
7. A. Pourghorban Saghati, J. Batra, J. Kameoka, and K. Entesari, "A Miniaturized Microfluidically Reconfigurable Coplanar Waveguide Bandpass Filter With Maximum Power Handling of 10 Watts", IEEE Transactions on Microwave Theory and Techniques, vol. 63, no. 8, pp. 2515-2525, 2015. https://doi.org/10.1109/tmtt.2015.2446477
8. G. Mumcu, A. Dey, and T. Palomo, "Frequency-Agile Bandpass Filters Using Liquid Metal Tunable Broadside Coupled Split Ring Resonators", IEEE Microwave and Wireless Components Letters, vol. 23, no. 4, pp. 187-189, 2013. https://doi.org/10.1109/lmwc.2013.2247750
9. P. Sen, and Chang-Jin Kim, "A Fast Liquid-Metal Droplet Microswitch Using EWOD-Driven Contact-Line Sliding", Journal of Microelectromechanical Systems, vol. 18, no. 1, pp. 174-185, 2009. https://doi.org/10.1109/jmems.2008.2008624
10. A. P. Saghati et al. "A microfluidically-switched CPW folded slot antenna." Antennas and Propagation Society International Symposium (APSURSI), 2014 IEEE. IEEE, 2014. https://ieeexplore.ieee.org/document/6904609
11. F. Banitorfian, et al. "A novel tunable water-based RF MEMS solenoid inductor." RSM 2013 IEEE Regional Symposium on Micro and Nanoelectronics. IEEE, 2013. https://ieeexplore.ieee.org/document/6706472
12. F. Banitorfian et al. "A novel switched-turn continuously-tunable liquid RF MEMS solenoid inductor." Proc. Int. Conf. Electron., Signal Process. Commun.. 2013. http://www.amcse.org/articles.php?id=143
13. I. El Gmati et al., "Variable RF MEMS fluidic inductor incorporating lamination process", Micro & Nano Letters, vol. 5, no. 6, p. 370, 2010. https://doi.org/10.1049/mnl.2010.0131
14. I. El Gmati et al., "Liquid RF MEMS variable inductor", Procedia Engineering, vol. 5, pp. 1380-1383, 2010. https://doi.org/10.1016/j.proeng.2010.09.372
15. N. Habbachi, H. Boussetta, A. Boukabache, M. Kallala, P. Pons, and K. Besbes, "Design and fabrication of a continuously tuned capacitor by microfluidic actuation", Journal of Micromechanics and Microengineering, vol. 28, no. 3, p. 035012, 2018. https://doi.org/10.1088/1361-6439/aaa63a
16. N. Habbachi, H. Boussetta, A. Boukabache, M. Kallala, P. Pons, and K. Besbes, "Fabrication and Modeling of a Capacitor Microfluidically Tuned by Water", IEEE Electron Device Letters, vol. 38, no. 2, pp. 277-280, 2017. https://doi.org/10.1109/led.2016.2644540
17. N. Sharafadinzadeh, M. Abdolrazzaghi, and M. Daneshmand, "Investigation on planar microwave sensors with enhanced sensitivity from microfluidic integration", Sensors and Actuators A: Physical, vol. 301, p. 111752, 2020. https://doi.org/10.1016/j.sna.2019.111752
18. A. Ebrahimi, J. Scott, and K. Ghorbani, "Microwave reflective biosensor for glucose level detection in aqueous solutions", Sensors and Actuators A: Physical, vol. 301, p. 111662, 2020. https://doi.org/10.1016/j.sna.2019.111662
19. B. Wiltshire, T. Zarifi, and M. Zarifi, "Passive Split Ring Resonator Tag Configuration for RFID-Based Wireless Permittivity Sensing", IEEE Sensors Journal, vol. 20, no. 4, pp. 1904-1911, 2020. https://doi.org/10.1109/jsen.2019.2950912
20. S. Mohammadi, R. Narang, M. Mohammadi Ashani, H. Sadabadi, A. Sanati-Nezhad, and M. Zarifi, "Real-time monitoring of Escherichia coli concentration with planar microwave resonator sensor", Microwave and Optical Technology Letters, vol. 61, no. 11, pp. 2534-2539, 2019. https://doi.org/10.1002/mop.31913
21. K. Paracha, A. Butt, A. Alghamdi, S. Babale, and P. Soh, "Liquid Metal Antennas: Materials, Fabrication, and Applications", Sensors, vol. 20, no. 1, p. 177, 2019. https://doi.org/10.3390/s20010177

22. M. Dickey, "Stretchable and Soft Electronics using Liquid Metals", Advanced Materials, vol. 29, no. 27, p. 1606425, 2017. https://doi.org/10.1002/adma.201606425
23. M. Khondoker, and D. Sameoto, "Fabrication methods and applications of microstructured gallium based liquid metal alloys", Smart Materials and Structures, vol. 25, no. 9, p. 093001, 2016. https://doi.org/10.1088/0964-1726/25/9/093001.

Arrived: 10. 09. 2021
Accepted: 15. 11. 2021

Original scientific paper
https://doi.org/10.33180/InfMIDEM2022.102

Informacije MIDEM
Journal of Microelectronics,
Electronic Components and Materials
Vol. 52, No. 1(2022), 11 – 16

A Concurrent Dual-band Low Noise Amplifier with Gain Enhancement Topology for 2.4/5.2 GHz Applications

Chun Wei[1,2], Ronghua Zhang[1,2], Zhiying Xia[1,2], Kui Cheng[1,2], Xinyu Liu[1], Weijun Luo[1]

[1]Institute of Microelectronics, Chinese Academy of Sciences, Beijing, China
[2]University of Chinese Academy of Sciences, Beijing, China.

Abstract: This paper presents a dual-band low-noise amplifier (LNA)operating at 2.4/5.2 GHz for wireless local area network (WLAN) applications. The LC parallel resonance and LC series network are adopted to achieve input impedance matching and noise matching simultaneously at dual-band. Besides, a small-size capacitor with a coupled inductor is added for gain-enhancement. The simulation results show that the LNA has gains(S21) of 17.1 dB and 8.5 dB with a noise figure of 3.6 dB and 3.3 dB at 2.4 GHz and 5.2 GHz, and input return loss(S11) of -15.6 dB and -13.8 dB while output return loss(S22) of -11.7 dB and -20.7 dB at two operating frequencies, respectively. Therefore, the proposed LNA structure is an attractive alternative to WLAN applications.

Keywords: concurrent; dual-band LNA;2.4 GHz/5.2 GHz; cascade; multi-frequencies

Sočasni dvopasovni ojačevalnik z nizkim šumom s topologijo za povečanje ojačenja za aplikacije 2,4/5,2 GHz

Izvleček: V prispevku je predstavljen dvopasovni ojačevalnik z nizkim šumom (LNA), ki deluje na frekvenci 2,4 / 5,2 GHz za aplikacije brezžičnega lokalnega omrežja (WLAN). Za simultano doseganje usklajevanja vhodne impedance in šuma pri dvopasovnem delovanju je spremenjena LC paralelna resonanca in LC serija omrežja. Poleg tega je za povečanje ojačenja dodan kondenzator majhne velikosti s povezano dušilko. Rezultati simulacije kažejo, da ima LNA povečanje (S21) 17,1 dB in 8,5 dB s šumom 3,6 dB in 3,3 dB pri 2,4 GHz in 5,2 GHz in vhodno povratno izgubo (S11) od -15,6 dB in -13,8 dB medtem ko izhodna povratne izgube (S22) znašajo -11,7 dB oziroma -20,7 dB pri dveh delovnih frekvencah. Predlagana struktura LNA je zanimiva alternativa aplikacijam WLAN.

Ključne besede: sočasnost; dvopasovni LNA;2.4 GHz/5.2 GHz; kaskada; več frekvenc

** Corresponding Author's e-mail: luoweijun@ime.ac.cn*

1 Introduction

With the development of the multiple standardization and miniaturization of a communication system [1], the multi-band RF front-end suitable for the interconnection between various applications receives noticeable attention.

As the first active stage of the RF receiver, a low noise amplifier (LNA) has a great impact on the performance of the RF front-end. Most of the articles about LNA published recently are based on reconfigurable LNA [2,3], broa dBand LNA [4] and concurrent LNA [5-7]. The advantages of reconfigurable LNA and broa dBand LNA are area consumption and bandwidth respectively, but

How to cite:
C. Wei et al., "A concurrent dual-band low noise amplifier with gain enhancement topology for 2.4/5.2 GHz applications", Inf. Midem-J. Microelectron. Electron. Compon. Mater., Vol. 52, No. 1(2022), pp. 11–16

their performance will deteriorate dramatically when applied in dual-band applications. Therefore, dual-band concurrent LNA is an attractive choice to make a trade-off between area consumption, noise, linearity and gain.

Generally, matching networks implemented in concurrent LNA are narrowband matching at input/output or inter-stage [6~9], and an external large resistor should be added for DC isolation. However, the thermal noise of the isolation resistor combining with the gate noise of MOSFET will significantly deteriorate the noise figure of LNA at high frequency. In this paper, a trap network accompanied by a series LC network is applied in the LNA for DC isolation and dual-band impedance matching, removing the effect of thermal noise of isolation resistor. Besides, a small-size capacitor with a coupled inductor is used to improve the gain.

The paper is organized as follows. Section II describes the design of the proposed circuit topology. Section III shows the layout simulation result of the LNA and section IV concludes this paper.

2 Circuit design

As shown in fig.1, the cascade structure is adopted in the proposed LNA to alleviate the Miller effect and obtain better reverse isolation. Meanwhile, the series LC combining with a parallel LC works as a dual-band impedance matching network. Besides, a capacitor with a coupled inductor is inserted to enhance the gain.

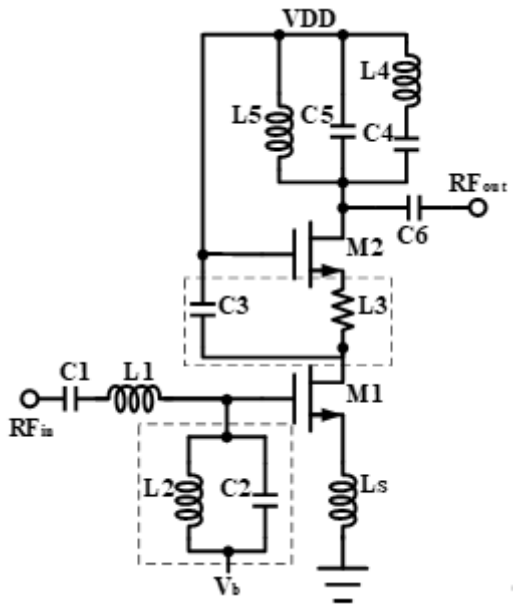

Figure 1: Schematic of the proposed dual-band LNA

2.1 Dual-band input and output impedance

Fig.2 shows the simplified small-signal equivalent circuit, and the input impedance,, can be expressed as follows:

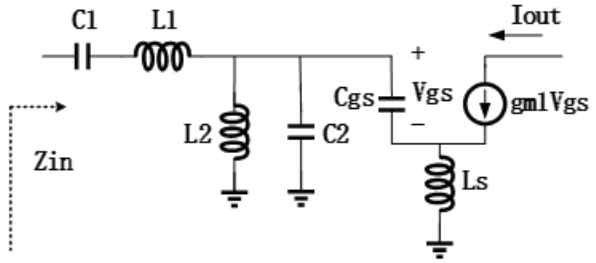

Figure 2: Small-signal equivalent circuit

$$Z_{\text{in}} = \frac{g_{m1}L_s}{C_{gs}} + j(\omega L_s - \frac{1}{\omega C_{gs}} - \frac{\omega^3 L_1 L_2 C_1 - \omega L_2}{\omega^4 L_1 L_2 C_1 C_2 - \omega^2 L_2 (C_1 + C_2) - \omega^2 L_1 C_1 + 1}) \quad (1)$$

In the equation, g_{m1} is the transconductance of M_1, Ls is the negative source fee dBack inductor, C_{gs} is the gate-source capacity of M_1, and Ω is the angular frequency related to 2.4 GHz or 5.2 GHz. To obtain dual-band impedance matching, the real part and imaginary part of Z_{in} should be equal to 50 Ω and zero respectively. And the real part of dual-band input impedance is given by:

$$\text{Re}[Z_{in}] = \frac{g_{m1}L_s}{C_{gs}} = 50\Omega \quad (2)$$

the imaginary part is given by:

$$\text{Im}[Z_{in}] = \omega L_s - \frac{1}{\omega C_{gs}} - \frac{\omega^3 L_1 L_2 C_1 - \omega L_2}{\omega^4 L_1 L_2 C_1 C_2 - \omega^2 L_2 (C_1 + C_2) - \omega^2 L_1 C_1 + 1} \quad (3)$$

As shown in Equation (4) and (5), the dual-band input impedance can be presented by the following parameters.

$$\omega_1 = (L_s, C_{gs}, L_1, L_2, C_1, C_2) \quad (4)$$

$$\omega_2 = (L_s, C_{gs}, L_1, L_2, C_1, C_2) \quad (5)$$

In the output matching network, two resonant frequencies of the network are 2.4 GHz and 5.2 GHz respectively, and Fig.3 shows how dual-frequency match-

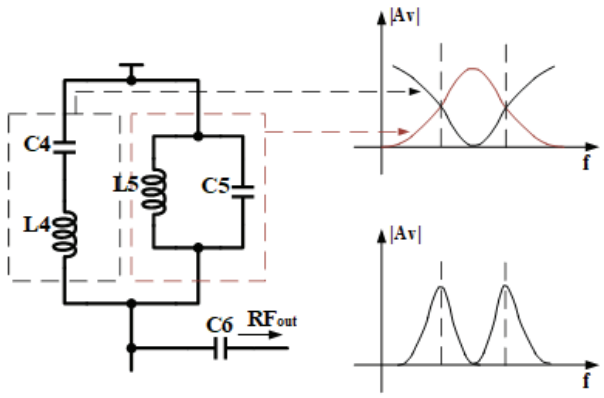

Figure 3: output matching filter

ing obtains [6]. This allows a better matching on each bandwidth.

Output impedance is described by equation(6):

$$Z_{out}=\frac{1}{j\omega C_6}+\left(\frac{j\omega L_5}{1-\omega^2 L_5 C_5}\right)\| j(\omega L_4-\frac{1}{\omega C_4}) \quad (6)$$

2.2 Noise analysis

This section describes the combination of impedance matching and noise optimization. And the equivalent circuit for noise analysis of the proposed LNA is shown in Fig.4.

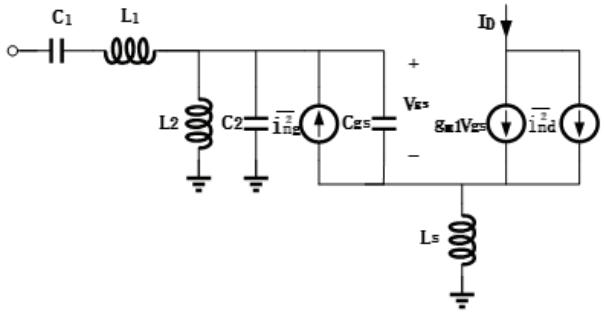

Figure 4: the equivalent circuit for noise analysis

The noise factor is described by equation [7]:

$$F=F_{\min}+\frac{R_n\,|\,Y_S-Y_{opt}\,|^2}{G_S} \quad (7)$$

In equation [7], R_n represents the source resistance, and G_s, Y_s, and Y_{opt} are the source conductance, the source admittance and the optimum source admittance respectively. And the parameters can be expressed as the following equations.

$$R_n=\frac{\gamma}{\alpha}\frac{1}{g_{m1}} \quad (8)$$

$$Y_S=Y_{\text{opt}}=\frac{1}{Z_{\text{opt}}} \quad (9)$$

In the equation, α is the constant related to the process, which $\alpha = g_m/g_{do}$, g_{do} is the drain-source conductance when the drain-source voltage Vds is equal to 0.γ is the channel noise figure of the transistor, which is related to the channel length.

When Y_s is equal to Y_{opt}, the minimum value of F is equal to F_{min}. According to Thomas theory [12], the noise factor F_{min} of the LNA can be expressed as:

$$F_{\min}=1+\frac{2}{\sqrt{5}}\frac{\omega}{g_{m1}/C_{gs}}\sqrt{\gamma\delta\left(1-|c|^2\right)} \quad (10)$$

In the equation, δ is the gate noise figure, and c is the correlation coefficient between the gate current noise and the leakage current noise, which is approximately equal to j0.395 in theory [13], reflecting the coupling capacitance between the channel and the gate induced noise source.

The optimum noise impedance is given by:

$$Z_{\text{opt}}=\frac{\alpha\sqrt{\frac{\delta}{5\gamma}(1-|c|^2)}+j(1-\alpha|c|\sqrt{\frac{\delta}{5\gamma}})^2}{\omega C_{gs}\left\{\frac{\alpha^2\delta}{5\gamma}(1-|c|^2)+\left(1-\alpha|c|\sqrt{\frac{\delta}{5\gamma}}\right)^2\right\}} - \left(j\omega L_s+\frac{j\omega L_2}{1-\omega^2 L_2C_2+\frac{\omega^2 L_2C_1}{\omega^2 L_1C_1-1}}\right) \quad (11)$$

It is obvious that Re [Y_{opt}]) Re [Z_{in}] and Im [Z_{opt}]= Im [Z_{in}]. Therefore, noise matching and impedance matching can be obtained simultaneously.

2.3 Gain enhancement technology

Generally, the LNA consists of two stages or more to obtain high gain. To reduce area consumption, a cascade structure with gm enhancement was implemented in the proposed single-stage LNA. Traditional technology adopts a cascade structure to eliminate the Miller effect and provide better reverse isolation [14]. Base on the small-signal analysis, the gain of the LNA without LC resonance network can be derived as:

$$A_{\text{v1}}=-\text{k}\bullet[1+(g_{m2}+g_{mb2})r_{o2}]g_{m1}r_{o1} \quad (12)$$

In the equation, r_{o1} is the output resistance of M_1, r_{o2}, is the output resistance of M_2, g_{m2} is the transconductance of M_2, g_{mb2} is the substrate transconductance of M_2, r_{o2} is the output resistance of M_2, and parameter k, X, β, are given by:

$$k = \frac{\chi Z_L}{r_{o2} + Z_L + [1 + (g_{m2} + g_{mb2}) r_{o2}] \cdot \beta} \tag{13}$$

$$\chi = \frac{\frac{j\omega L_s}{1 - \omega^2 L_s C_2}}{j(\omega L_1 - \frac{1}{\omega C_1} + \frac{\omega L_2}{1 - \omega^2 L_2 C_2})} \tag{14}$$

$$\beta = r_{o1} + (1 + g_{m1} r_{o1}) sL_s \tag{15}$$

When the LC resonance network is added, parameter k is expressed as k1, which is given by:

$$k_1 = \frac{\chi Z_L}{(r_{o2} + Z_L) x_1 + [1 + (g_{m2} + g_{mb2}) r_{o2}] x_2} \tag{16}$$

where, $x_1 = \left(1 + \frac{\beta}{sC_3}\right)$ and $x_2 = \left(sL_3 + \frac{L_3}{C_3}\beta\right)$. It is obvious that the gain can be enhanced by making an adjustment of L3/C3, which is presented in the simulation results.

3 Simulation results

This section presents the simulation results of the proposed dual-band LNA operating at 2.4 GHz and 5. 2 GHz.The layout of the proposed LNA is shown in Fig.5. S-parameters, NF and P1 dB of the LNA are shown in Fig 6-11 respectively. The proposed LNA is implemented on the SMIC 0.13um 1P8M CMOS process, and the chip size of the layout is 642.6 x910.1 . The simulation results of the LNA exhibits S11 of -15.6 dB and -13.8 dB, S22 of -11.7 dB and -20.7 dB at 2.4 GHz and 5.2 GHz, which are shown in Fig. 6-7. The LNA exhibits 17.1 dB of gain, 3.6 dB of noise figure, -16.49 dBm of P1 dB at 2.4 GHz; 8.5 dB of gain,3.3 dB of noise figure, -9.53 dB of P1 dB at 5.2 GHz, which are shown in Fig.7-10. With a supply voltage of 1.2V , the power consumption of the receiver is 9.8 mW. As a summation, table1 shows all the simulation results.

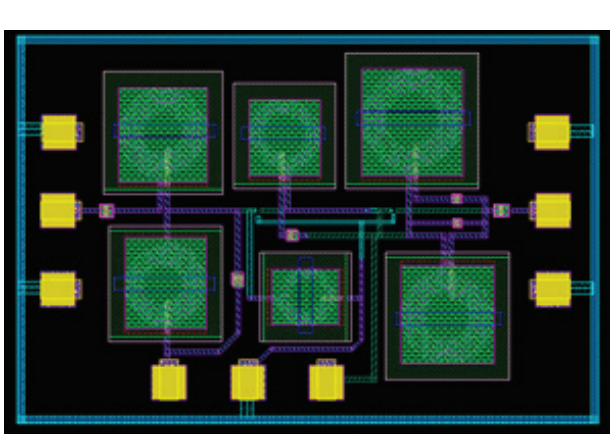

Figure 5: The layout of the Low Noise Amplifier

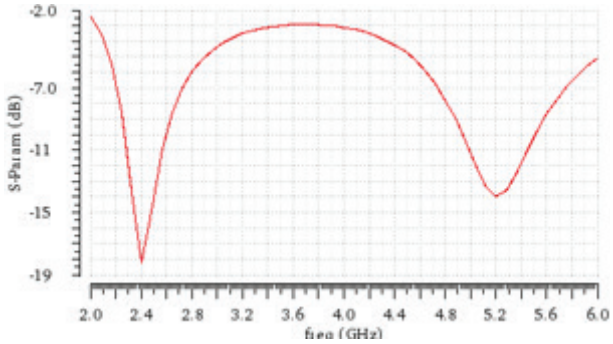

Figure 6: Simulated input loss (S11) of the dual-band LNA

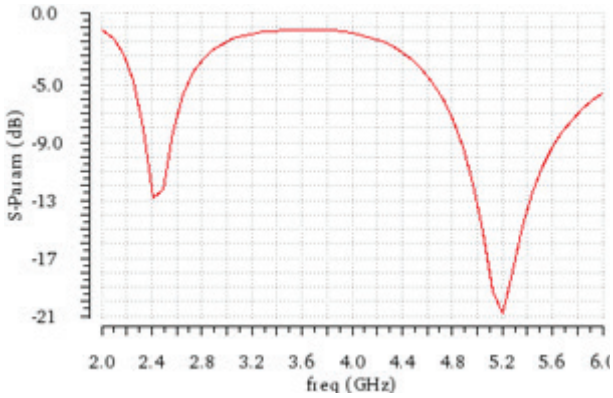

Figure 7: Simulated output loss(S22) of the dual-band LNA

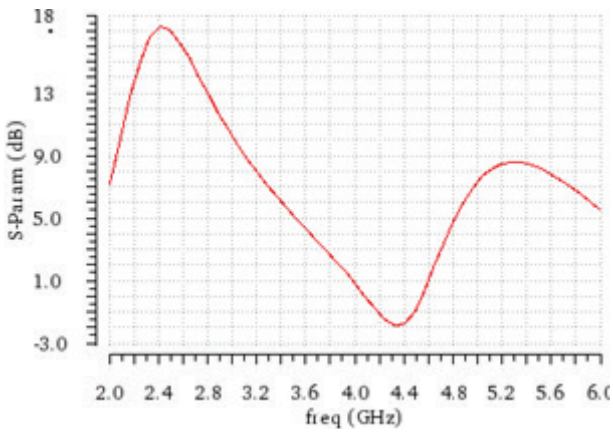

Figure 8: Simulated gain(S21) of the dual-band LNA

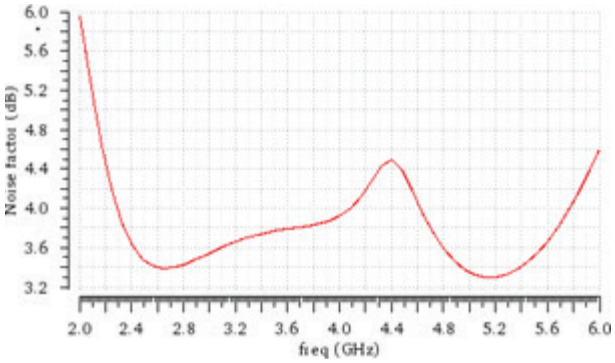

Figure 9: Simulated noise figure(NF)

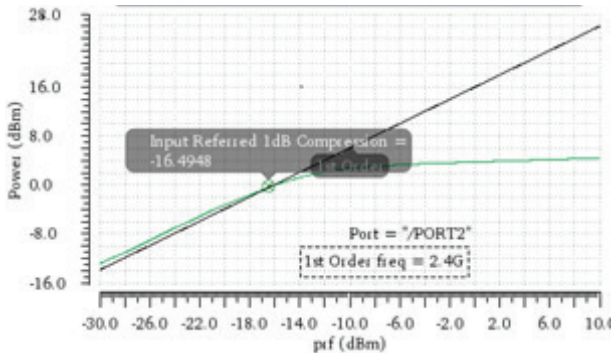

Figure 10: Simulated P1 dB compression point at 2.4 GHz

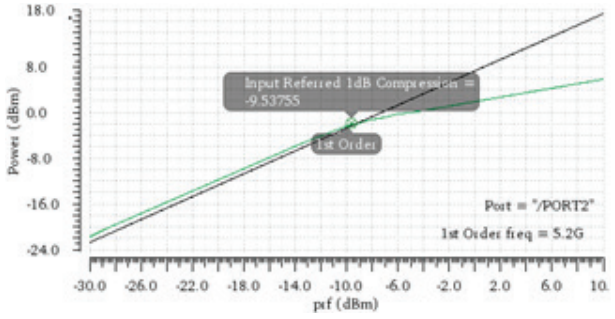

Figure 11: Simulated P1 dB compression point at 5.2 GHz

The performance of the proposed LNA is summarized in Table 1, which is compared to other papers published working at 2.4 GHz and 5. 2 GHz.The performance shows a good trade-off between impedance matching, noise, linearity and gain. However, the proposed LNA consists of one-stage, which is designed under the limitation of minimum noise figure. And multi-stage cascade structure can be adopted to reduce the design difficulty without the limitation of area consumption and power dissipation. Besides, folded cascade structure with lower supply voltage is an attractive choice for low power applications.

4 Conclusions

A dual-band concurrent LNA operating at 2.4 GHz and 5.2 GHz with gain enhancement technology is presented in this paper. The LNA designed shows a noise figure below 3.6 dB and the input /output return loss is better than-10 dB. And the power consumption is 9.8mW with a power supply voltage of 1.2V. As the performance mentioned above exhibits, the proposed concurrent dual-band LNA is suitable for multi-frequencies RF systems like WLAN.

5 Conflict of interest

We declare that we do not have any commercial or associative interest that represents a conflict of interest in connection with the work submitted.

6 Reference

1. A. Hamasawa and H. Kanaya, "Dual-band differential outputs CMOS Low Noise Amplifier," 2018 IEEE 20th Electronics Packaging Technology Conference (EPTC), Singapore, Singapore, 2018, pp. 661-664. https://doi.org/10.1109/EPTC.2018.8654309.
2. Liang-Hung Lu, Hsieh-Hung Hsieh, and Yu-Shun Wa-ng, "A compact 2.4/5.2- GHz CMOS dual-band low-noise amplifier," in IEEE Microwave and Wireless Components Letters, vol. 15, no. 10, Oct. 2005, pp. 685-687. https://doi.org/10.1109/LMWC.2005.856845.
3. O. Eslamifar and R. S. Shirazi, "Design a dual-band low-power CMOS low noise amplifier for use in WLAN applications," 2014 22nd Iranian Conference on Electrical Engineering (ICEE), Tehran,2014, pp.101-105. https://doi.org/10.1109/IranianCEE.2014.6999512.
4. S. Arshad, R. Ramzan, and Qamar-ul-Wahab, "Wide-band common gate LNA with novel input matching technique," 2016 5th International Conference on Modern Circuits and Systems Technologies (MOCAST), Thessaloniki, 2016, pp. 1-4. https://doi.org/10.1109/MOCAST.2016.7495103.
5. T. Kitano, K. Komoku, T. Morishita and N. Itoh, "A C-MOS LNA equipped with concurrent dual-band matching networks," 2017 IEEE Asia Pacific Microwave Conference (APMC), Kuala Lumpar, 2017, pp. 566-569. https://doi.org/10.1109/APMC.2017.8251508.

6. S. Sattar and T. Z. A. Zulkifli, "A 2.4/5.2- GHz Concur-rent Dual-Band CMOS Low Noise Amplifier," in IEEE Access, vol. 5, 2017, pp. 21148-21156. https://doi.org/10.1109/ACCESS.2017.2756985.
7. E. Kargaran and B. Madadi, "Design of a novel dual-band concurrent CMOS LNA with current reuse topology," 2010 International Conference on Networking and Information Technology, Manila, 2010, pp. 386-388. https://doi.org/10.1109/ICNIT.2010.5508490.
8. Hong Y J, Wang S F, Chen P T, et al. A concurrent dual-band 2.4/5.2 GHz low-noise amplifier using gain enhanced techniques[J]. 2015:231-234. https://doi.org/10.1109/APEMC.2015.7175329.
9. Khosravi H, Zandian S, Bijari A, et al. A Low Power, High Gain 2.4/5.2 GHz Concurrent Dual-Band Low Noise Amplifier[C]// 2019 IEEE 9th Annual Computing and Communication Workshop and Conference (CCWC). IEEE, 2019. https://doi.org/10.1109/CCWC.2019.8666621.
10. Wei-Chen Huang, Chen-Ming Hsu, Chien-Ming Lee, Hong-Yi Huang, and Ching-Hsing Luo, "Dual-band LNA/mixer using conjugate matching for implantable biotelemetry," 2008 IEEE International Symposium on Circuits and Systems, Seattle, WA, 2008, pp. 1764-1767. https://doi.org/ 10.1109/ISCAS.2008.4541780.
11. H. A. Haus et al., "Representation of noise in linear two ports," Proc. IRE, vol. 48, no. 1, pp. 69–74, Jan. 1960
12. Lee T H. The design of CMOS radio-frequency integrated circuits, 2nd edition[J]. Communications Engineer, 2004, 2(4):47-47. https://doi.org/ 10.1109/MCD.2006.1708388
13. Lee T H. The design of CMOS radio-frequency integrated circuits, 2nd edition[J]. Communications Engineer, 2004, 2(4):47-47.
14. Dengjun Lai, Yingmei Chen, Xiaodong Wang and Xuehui Chen, "A CMOS Single-Differential LNA and current bleeding CMOS mixer for GPS Receivers," 2010 IEEE 12th International Conference on Communication Technology, Nanjing, China, 2010, pp. 677-680, https://doi.org/10.1109/ICCT.2010.5688505.

Arrived: 09. 01. 2021
Accepted: 23. 04. 2021

Original scientific paper
https://doi.org/10.33180/InfMIDEM2022.103

Informacije MIDEM
Journal of Microelectronics,
Electronic Components and Materials
Vol. 52, No. 1(2022), 17 – 27

Operation of Permanent Magnet Synchronous Motor after Open-circuit Battery Supply Fault

Vanja Ambrožič[1], Mitja Breznik[2], Mitja Nemec[1]

[1]University of Ljubljana, Faculty of Electrical Engineering, Ljubljana, Slovenia
[2]Kolektor Group d.o.o., Idrija, Slovenia

Abstract: This paper presents a method for post-fault operation with reduced performance of a permanent magnet synchronous motor following a battery supply open circuit fault. The approach upgrades the previously developed fast model-oriented supply fault detection algorithm based on comparing actual and estimated values of a DC-link voltage. The latter is determined by the model of supply circuit and observer of battery open-circuit voltage. Implementing a post-fault concept does not require additional hardware, as it uses quantities from an already existent vector control algorithm. After the fault is detected, the algorithm is upgraded by a DC-link voltage cascade control loop. An analytical approach to parametrization of the controller, based on the linearization and the reduction of the system's transfer function, is also proposed. Simulations and experimental results have validated the performance of the post-fault algorithm.

Keywords: power supply fault; model-based detection algorithm; control loop parametrization; DC-link voltage regulator; fault-tolerant design

Delovanje sinhronskega motorja s trajnimi magneti po izpadu akumulatorskega napajanja

Izvleček: Članek predstavi metodo za nadaljevanje obratovanja sinhronskega stroja s trajnimi magneti z zmanjšano zmogljivostjo po izpadu akumulatorskega napajanja. Pristop nadgrajuje že razviti modelsko orientirani algoritem za ugotavljanje izpada napajanja, ki sloni na primerjavi dejanske in ocenjene vrednosti napetosti vmesnega tokokroga. Slednjo ugotavljamo prek modela napajalnega vezja in opazovalnika napetosti odprtih sponk akumulatorja. Implementacija koncepta obratovanja stroja po napaki ne zahteva dodatne aparaturne nadgradnje, ker uporablja že obstoječe količine, potrebne za normalno delovanje. Regulacijski algoritem po detekciji napake nadgradimo s kaskadno zanko za regulacijo napetosti vmesnega tokokroga. V članku je predstavljeno tudi analitično parametriziranje regulatorja, ki sloni na linearizaciji in redukciji sistemske prenosne funkcije. Simulacije in eksperimentalni rezultati potrjujejo učinkovitost obratovanja po napaki.

Ključne besede: izpad napajanja, modelno zasnovani detekcijski algoritem, parametriziranje regulacijske zanke, regulator napetosti vmesnega tokokroga, zasnova odporna na izpade

** Corresponding Author's e-mail: vanja.ambrozic@fe.uni-lj.si*

1 Introduction

Battery-supplied permanent magnet synchronous motor (PMSM) often appears as the main or auxiliary component in various mobility applications due to its high efficiency and high power density [1]. Therefore, research on fault mechanisms and post-fault operation of systems that enable key operational features in a vehicle is the basis for providing appropriate safety and reliability. The probability of a supply system failure has already been extensively investigated [2]. However, the development of diagnostic and post-fault operation methods for a drive in case of power supply failure

How to cite:
V. Ambrožič et al., "Operation of Permanent Magnet Synchronous Motor after Open-circuit Battery Supply Fault", Inf. Midem-J. Microelectron. Electron. Compon. Mater., Vol. 52, No. 1(2022), pp. 17–27

lags behind the successfully implemented solutions that cope with the faults in PMSM, converter, and/or appropriate sensors [3]–[10]

The interruption of the supply system can be caused by damage or change of operational state (e.g., disconnection due to safe stop) of individual drive subsystems. One of these is an intermediate DC/DC converter whose failure may prevent the proper energy flow. Method for fault detection of switching elements in a step-down converter feeding a brushless DC machine is proposed in [11]. Different fault scenarios in a parallel DC/DC converter for interconnecting electrical drive and various power sources are analyzed in [12].

The fault mechanism and consequent detection methods for battery voltage sources have been thoroughly investigated. The number of connections between individual battery cells increases the fault probability, which is reflected through galvanic interruptions, an increase of impedance, or a decrease in power capacity. The fault/breakage detection of welds between battery cells in electric vehicles, based on a statistical energy capacity determination, has been investigated in [13]. A comprehensive overview of supply systems fault diagnosis based on Li-Ion technology has been presented in [14].

A high-voltage battery system in hybrid and electric vehicles is connected to the rest of the drive through a contactor. The interruption of the contactor, with subsequent disconnection of a supply circuit, is implemented in case of a safe stop or emergency shutdown following an accident. In case of an emergency shutdown, a safe level of DC-link voltage has to be provided in conformity with ECE R94 [15]. A method for reducing the voltage without a braking resistor has been presented in [16]. Operation is based on upgrading the field-oriented control (FOC) with a DC-link voltage controller and modulation index controller. The detection method and guidelines for the determination of controller parameters are not presented.

Supervision of the energy flow and DC-link voltage level is crucial in drives with diode rectifiers. Dynamic braking of the PMSM can be achieved by directing the mechanical energy into additional Joule losses in the machine's windings. The DC-link voltage level is limited by keeping machine losses equal to braking power through stator current *d* and *q* components in the field reference frame [17]. Control algorithm for braking of switched reluctance machine is also proposed [18]. Limited braking capability and consequent regenerative performance are also present in battery-fed electrical drives that are close to energy capacity limits. In [19], the approach for limiting the energy flow into the DC supply through the increase of losses by injecting high-frequency current components into the *d* axis of an induction motor is presented.

Operating conditions, similar to those caused by the fault of the supply system, can be found in FOC doubly-fed induction generators in island operation [20]. The system provides for the DC load voltage and supplies the rotor windings with AC voltage oscillating at slip frequency. A separate control loop controls DC-link voltage, adapting it to the reference. A cascade voltage control of a three-phase rectifier DC-link voltage has been studied in [21]. The output power of the load is determined by the observer that allows for the implementation of the inner control loop based on the power reference.

Finally, it can be concluded that due to the complexity of supply systems, several sources and causes can interrupt the energy flow. If the PMSM drive operates in the regenerative mode or the field weakening region, this fault may produce secondary damage caused by the failure of electronic components due to overvoltage [9].

In this paper, a detection method and appropriate control algorithm that prevents secondary damage without the need for additional hardware modifications (e.g., braking resistors, electronic components with higher values of the maximum permitted voltages) is presented. In order to ensure a fast and robust transition to the post-fault operation, a model-oriented algorithm for real-time detection of supply interruption has been applied. As a result, the diagnostic method and post-fault algorithm constitute a fault-tolerant system, based on the most commonly used configuration of the supply system and control method for PMSM (FOC).

Post-fault control approach and analytical guidelines for controllers' parametrization provide for:

- maintaining the DC-link voltage level inside predetermined operational boundaries. The maximum voltage is defined by the maximum permitted voltage of the converter's electronic components. On the other side, the minimum voltage level is defined by the minimum supply voltage required by the converter's peripheral and logic units in the case of controllers with a single supply.
- control of PMSM electrical quantities, even in field weakening region.
- potential for upgrading the control scheme that enables the drive's deceleration by injecting the currents that cause additional losses in the system.
- sufficient time for the electronics to enter the safe-stop mode.

2 System definition

The proposed method is developed for a standard and straightforward system of battery-fed PMSM drive. The system consists of Li-Ion batteries, supply cables, inverter with accompanying capacitor bank, and a PMSM. Block scheme of individual parts of the drive with potential failure locations is depicted in Fig. 1. Although this paper presents a method designed for a specific configuration, the approach could be easily adapted to different types of machines and topologies of supply circuits, since it is based on modelling of the supply circuit and well-established control principle.

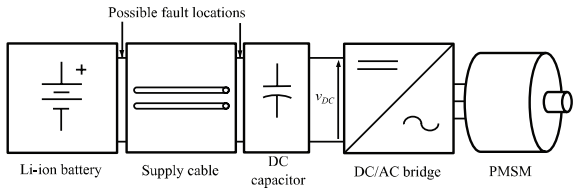

Figure 1: Graphic representation of the analyzed system.

Block scheme showing FOC of PMSM drive, capable of operating in field weakening region, is shown in Fig. 2 [22]. The scheme already includes proposed fault detection and a post-fault approach (inside a dotted rectangle), described in detail in the following sections. The symmetrical voltage model of PMSM in *d-q* rotor field coordinates is determined by (1), where v_d, v_q, i_d and i_q represent stator voltages and currents in a rotor reference frame. R_s, L_d, L_q and ψ_m denote stator resistance, inductances, and flux of the rotor's permanent magnet, respectively. Electromagnetic torque T_e in case of surface-mounted permanent magnet motor (SPM) or interior permanent magnet motor (IPM) with similar L_d and L_q can be defined by (2), where p_p is the number of pole pairs. Electric power is defined by (3).

$$\begin{bmatrix} v_d \\ v_q \end{bmatrix} = \begin{bmatrix} R_s + sL_d & -\omega L_q \\ \omega L_d & R_s + sL_q \end{bmatrix} \begin{bmatrix} i_d \\ i_q \end{bmatrix} + \begin{bmatrix} 0 \\ \omega \psi_m \end{bmatrix} \tag{1}$$

$$T_e = \frac{3}{2} p_p i_q \psi_m \tag{2}$$

$$p_e = \frac{3}{2} p_p (v_d i_d + v_q i_q) \tag{3}$$

3 Fault detection

The dynamics of post-fault response depends on fast and reliable fault detection to avoid false positives or false negatives. In this paper, the post-fault algorithm relies on the model-based detection that has been proven effective [23]. Possible open-circuit fault locations depicted in Fig. 1 can be quickly detected by monitoring the change of DC-link voltage. However, only a specific change to this phenomenon must be considered, while the changes due to regular operation should be ignored. This task can be achieved by comparing the measured DC-link voltage (measurement performed in almost every drive) to the one obtained through the model.

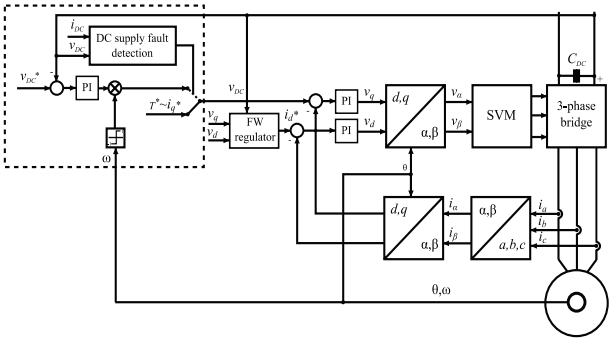

Figure 2: The control scheme of PMSM drive with added detection and post-fault control blocks.

Furthermore, the model and corresponding control circuit must be robust and self-adaptable to slow changes. These are caused by battery state-of-charge and parasitic effects, which occur during regular operation and react only to fast changes, owing to an open circuit. The model is based on a Thévenin's circuit shown in Fig. 3, where i_{batt} and v_{batt} denote battery current and voltage, i_{DC} and v_{DC} are DC-link current and voltage. v_{oc} is the battery's open-circuit voltage, and R_i is its internal resistance. Supply cable is represented by resistance R_c and inductance L_c of the transmission path, as calculated from [24]. Total capacitance C_{DC} and series resistance R_{esr} represent DC-link capacitor bank.

Since linear elements form the electrical circuit, the model estimated DC-link voltage ($\hat{v}_{DC}$) could be calculated as the sum of two terms that depend on i_{DC} and v_{oc}, respectively

$$\hat{v}_{DC} = \hat{v}_{DC}^{i_{DC}} + \hat{v}_{DC}^{v_{oc}} \tag{4}$$

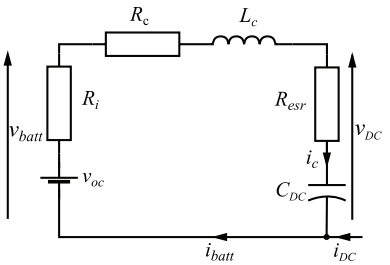

Figure 3: Lumped element electric circuit model of DC supply.

The transfer functions of the two terms are defined as

$$F_{iDC}(s)=\frac{\hat{v}_{DC}^{i_{DC}}(s)}{i_{DC}(s)}= \\ =\frac{R_i+R_c+sC_{DC}R_{esr}\left(R_c+R_i\right)+sL_c+s^2L_cC_{DC}R_{esr}}{-1-sC_{DC}\left(R_i+R_c+R_{esr}\right)-s^2L_cC_{DC}} \quad (5)$$

and

$$F_{voc}(s)=\frac{\hat{v}_{DC}^{v_{oc}}(s)}{\hat{v}_{oc}(s)}= \\ =\frac{1+sC_{DC}R_{esr}}{1+sC_{DC}\left(R_{esr}+R_i+R_c\right)+s^2L_cC_{DC}} \quad (6)$$

as represented in a block scheme in Fig. 4.

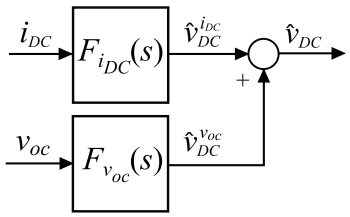

Figure 4: Block diagram of a DC supply model.

As previously mentioned, the main idea of the diagnostic approach to battery open circuit detection is to monitor the difference between the estimated and measured v_{DC} (Fig. 5). Consequently, in an open circuit, the measured and the estimated value will differ. However, the erroneous estimation may also generate the difference, thus leading to a false positive. The causes for this effect are either altered battery voltage (v_{oc}) or erroneously estimated/modified lumped circuit parameters.

The change of battery open circuit voltage v_{oc} during operation is normal and relatively slow. Thus its estimation should be incorporated into the diagnostic scheme (Fig. 5) that now has to fulfill two tasks:

- $\hat{v}_{oc}$ estimation: $\hat{v}_{oc}$ is needed for $\hat{v}_{DC}$ estimation in (4) and (6). Fortunately, during normal operation $\hat{v}_{oc}$, and consequently the v_{DC} estimation error *e*, change slowly; thus the slower and stable inner control algorithm should adapt the estimated value $\hat{v}_{oc}$ and so minimize the error. A possible solution could be using the sliding mode observer [23,25].
- Battery open-circuit fault detection: Sudden error between measured and estimated DC-link voltage *e*, after $\hat{v}_{oc}$ has been adequately tracked, could be caused only by some other fault source – open circuit – as will be explained next.

At steady-state (5) and (6) can be simplified, leading to the equation for DC link voltage error from Fig. 5

$$\varepsilon_m=\underbrace{v_{DC}-\hat{v}_{DC}}_{\varepsilon}\pm\zeta_\varepsilon=\underbrace{v_{DC}-\hat{v}_{oc}+i_{DC}\left(R_i+R_C\right)}_{\varepsilon}\pm\zeta_\varepsilon= \\ v_{DC}-\hat{v}_{oc}+\frac{3}{2v_{DC}}\left(v_di_d-v_qi_q\right)\left(R_i+R_C\right)\pm\zeta_\varepsilon \quad (7)$$

The term consists of:

- ε – the difference between measured (v_{DC}) and estimated ($\hat{v}_{DC}$) DC-link voltage. Note that i_{DC} in $\hat{v}_{DC}$ is calculated from control variables instead of being measured.
- ζ_e – the error due to erroneous modeling (parameter mismatch, discretization, measurement error, etc.)

The maximum possible error of ζ_e (denoted as ζ_{e_max}) can be analytically determined and serves as a diagnostic threshold. Hence, as depicted in Fig. 5, if the error ε_m exceeds $\zeta_e = \zeta_{e\_max}$, the open circuit has undoubtedly occurred.

Such diagnostic method proves to be reliable and fast, allowing for fast post-fault operation.

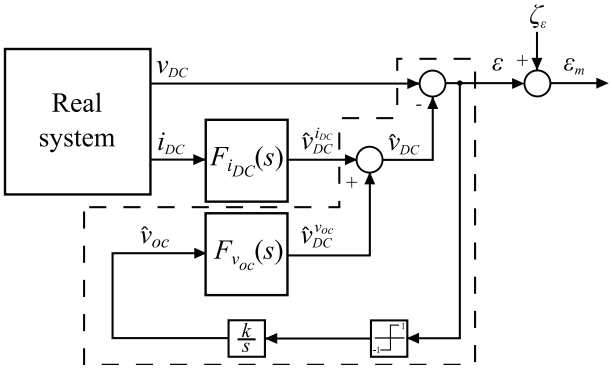

Figure 5: Block diagram of the estimation model.

4 Post fault operation

Once the fault is detected, post fault operation can be performed in two ways. The first one is to shut down the inverter. While the simplest to implement, this option is only viable when the drive is not in a field weakening mode or the inverter's DC link does not supply the electronics. During field weakening, current control has to stay active. Also, if the inverter's DC link should supply the electronics, rotational energy can be used to provide the necessary power, at least for some time.

The DClink voltage can change significantly during the fault transient, as the magnetic energy stored in machine windings dissipates to the DC-link regardless of

the post fault operation mode. Therefore, for the inverter to survive such a fault, it has to be designed accordingly. Only then can the inverter take appropriate action to control the DC-link voltage.

4.1 Inverter design considerations for open circuit battery supply fault

Immediately following the fault, i_d should remain unchanged. It is already zero in a constant torque mode, while in field weakening mode, it prevents back emf from rising above a safe level. The only active required power flow is for supplying the control electronics and the motor losses. Hence, the active power current component i_q after the fault transient will be almost zero.

After the fault, the energy circulates only between the machine and the inverter. After inserting (1) into (3), three distinct power flow components can be identified: winding losses (P_{loss}), reactive power (P_r), and mechanical power (P_{mech}) (8).

$$p_e = \frac{3}{2}\left(\underbrace{R_s i_d^{\,2} + R_s i_q^{\,2}}_{P_{loss}} + \underbrace{L_d i_d \frac{di_d}{dt} + L_q i_q \frac{di_q}{dt}}_{P_r} + \underbrace{\omega \psi_m i_q + \omega i_d i_q (L_d - L_q)}_{P_{mech}} \right) \tag{8}$$

In order to assess the under-/overvoltage, the energy transferred from fault occurrence until the end of fault transient (t_1) should be calculated .

$$\Delta W = \int_0^{t_1} p_e dt = \frac{3}{2}\int_0^{t_1} \left(R_s \left(i_d^{\,2} + i_q^{\,2} \right) + \omega i_q \left(\psi_m + i_d (L_d - L_q) \right) \right) dt - \frac{3 L_q i_{q0}^2}{4} \tag{9}$$

The amount of transferred magnetic (reactive) energy does not depend on the transient duration but only on the current values at the beginning of the transient i_{d0}, i_{q0} ($t=0$). Additionally, since i_d remains almost unaltered, its derivative can be neglected.

The total duration of the fault transient (t_1) consists of fault detection time t_{det} and current transient time $\mathrm{D}t$ (assuming local linearity, see (13))

$$t_1 = t_{det} + \Delta t \tag{10}$$

The final equation for the total energy transferred during the transient is

$$\Delta W = \frac{3}{2}\left((R_s i_{q0}^2 + \omega \psi_m i_{q0})(t_{det} + \frac{\Delta t}{2}) - L_q \frac{i_{q0}^2}{2} \right) \tag{11}$$

With a shorter total time t_1, the energy transferred between the machine and inverter will be lower; thus, the under-/overvoltage on DC-link will be reduced.

The main parameters determining the duration of the current transient (Δt) are machine inductances L_d, L_q, and the voltage difference between maximum applicable inverter voltage and back emf.

$$\sqrt{v_d^2 + v_q^2} = \frac{v_{DC}}{\sqrt{3}} \tag{12}$$

Insertion of (1) into (12), neglecting the terms with resistance R_s (being significantly smaller than other contributions) and di_d/dt (since i_d remains constant), and also assuming linear transition of i_q ($di_q/dt = -i_{q0}/\Delta t$) results in .

$$(L_q \frac{-i_{q0}}{\Delta t} + \omega L_d i_{d0} + \omega \psi_m)^2 = \frac{v_{DC}^2}{3} - (-\omega L_q i_{q0})^2 \tag{13}$$

The solutions of the quadratic equation for Δt with different i_d, i_q pairs in $i_d < 0$ half-plane (which corresponds to normal operation/field weakening), show that the transient time $\mathrm{D}t$ mainly depends on i_q (Fig 6).

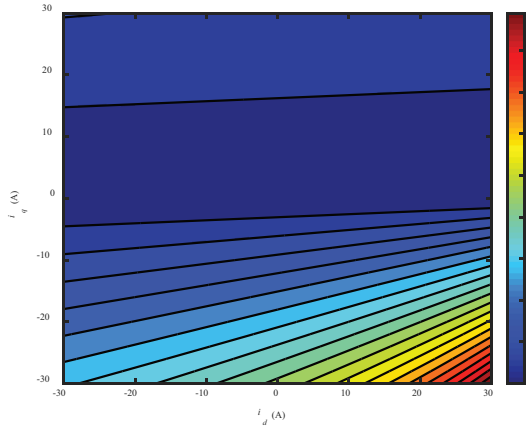

Figure 6: Transient duration.

The total energy transferred will alter the energy level in the DC-link capacitor (14), resulting in either an increased or decreased DC voltage (v_{DC_1}) compared to the voltage at the instant of the fault v_{DC_0}. Using (11) and (14), the relation between final DC-link voltage v_{DC_1} and DC-link capacitance is obtained (15).

$$\Delta W = \frac{C_{DC}(v_{DC\_1}^2 - v_{DC\_0}^2)}{2} \tag{14}$$

$$v_{DC\_1} = \sqrt{v_{DC\_0}^2 - \frac{3}{C_{DC}^2}\alpha} \tag{15}$$

where

$$\alpha = \left(R_s i_{q0}^2 + \omega \psi_m i_{q0}\right)\left(t_{det} + \frac{\Delta t}{2}\right) - \frac{L_q i_{q0}^2}{2}$$

Equation (15) serves as a design criterion for assessing the drive's tolerance during the supply fault to overvoltage, when in generator mode, and undervoltage, in motoring mode.

4.2 Post-fault DC-link voltage control

After the supply fault detection, the DC link voltage has to stay under control, especially in field weakening mode, to prevent further faults. Since the field weakening controller still sets the direct current id in this case, the voltage can be controlled by quadrature current i_q. The sign of i_q has to account for the direction of rotation (dotted area in Fig. 2).

4.2.1 Tuning DC-link voltage controller

The selection of voltage controller parameters is especially critical for achieving fast transients. In order to set the parameters analytically, the control loop (Fig. 7) has to be analyzed.

Electric power drawn from the DC-link depends on the speed and torque of the machine, with losses in machine and inverter neglected (16).

$$p_e = T_e \frac{\omega}{p_p} = \frac{3}{2}\omega i_q \psi_m \tag{16}$$

Thus, the DC-link voltage is

$$v_{DC} = i_{DC} R_{esr} + \frac{1}{sC_{DC}} i_{DC} \tag{17}$$

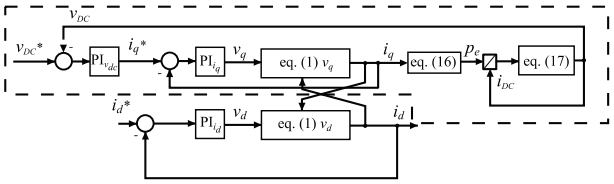

Figure 7: Block scheme of a post-fault voltage control loop.

As can be seen, the control loop is nonlinear and depends on multiple input parameters. However, several simplifications can be introduced to obtain an analytically solvable system.

Nonlinear relationship in DC-link current i_{DC} calculation from power p_e can be linearized as the loop will operate only around the DC-link voltage reference value. Hence DC link voltage (v_{DC}) can be considered pseudo-constant resulting in the division (far right-hand side on Fig. 7) being replaced by multiplication with constant v_{DC}^{-1}.

Furthermore, as the mechanical speed ω dynamics is several orders of magnitude slower than electrical transients, the mechanical speed can also be considered constant during these transients. Consequently, the direct axes current i_d, which is used only for field weakening (the latter is a function of ω), can also be considered constant. Hence, the i_d control loop in Fig. 7 is oblivious.

Thus the transfer function of the system, including i_q current PI controller with gains K_{p_q}, K_{i_q} (dashed in Fig. 6), is

$$F_s = \frac{3}{2}\frac{\omega \psi_m}{v_{DC}^* C_{DC}} \cdot \frac{K_{p\_q} C_{DC} R_{esr} s^2 + (K_{p\_q} + K_{i\_q} C_{DC} R_{esr}) s + K_{i\_q}}{L_q s^3 + (K_{p\_q} + R_s) s^2 + K_{i\_q} s} \tag{18}$$

The equation can be rewritten in a form where individual time constants can be easily identified

$$F_s = \frac{3}{2}\omega \psi_m \frac{K_{i\_q}\tau_1\tau_2}{v_{DC}^* C_{DC} L_q} \frac{\left(\frac{K_{p\_q}}{K_{i\_q}} s + 1\right)(C_{DC} R_{esr} s + 1)}{s(\tau_1 s + 1)(\tau_2 s + 1)} \tag{19}$$

where

$$\tau_{1,2} = \frac{2L_q}{K_{p\_q} + R_s \pm \sqrt{\left(K_{p\_q} + R_s\right)^2 - 4L_q K_{i\_q}}} \tag{20}$$

By setting the current controller parameters $K_{p\_q}/K_{i\_q} = \tau_2$, the order of the transfer function is further reduced [26,27]. Additional simplification is possible by neglecting R_{esr}. The result of this reduction is a second-order system (21).

$$F_s = \frac{3}{2}\omega \psi_m \frac{\tau_1 K_{p\_q}}{v_{DC}^* C_{DC} L_q} \frac{1}{s(\tau_1 s + 1)} \tag{21}$$

This system can be further reduced to an integrator with a delay (22).

$$F_s(s) = k' \frac{e^{-\tau_d s}}{s} \tag{22}$$

with gain defined as

$$k' = \frac{3}{2}\omega\psi_m \frac{\tau_1 K_{p\_q}}{v_{DC}{}^* C_{DC} L_q} \quad (23)$$

The delay τ_d is calculated as proposed in [27]

$$\tau_d = \frac{\tau_1}{2} + \frac{\tau_s}{2} \quad (24)$$

using a time constant of the initial transfer function $_1$, and sampling time τ_s.

Now a voltage PI controller can be parametrized. "Simple control" or "Skogestad (SIMC)" guidelines offer the recipe for setting the (voltage) controller parameters for the transfer function in form equal to (25), where $_c$ is the desired closed loop time constant.

$$k_p = \frac{1}{k'} \frac{1}{(\tau_c + \theta)}, \tau_i = 4(\tau_c + \theta) \quad (25)$$

The v_{DC} control should function regardless of the operational point. As the system gain k' actually depends on rotor speed and DC voltage reference setpoint (23), the proportional k_p gain in (25) has to adapt accordingly.

5 Simulation results

First, the simulations were performed to test if the simplifications of the DC-link voltage control loop in section 4 were justified. The parameters correspond to those of the experimental system (Tables 1 and 2).

The transient response of a simplified system based on (18) and fully nonlinear system described in (8), were compared. The controller parameters for both systems were set using (25). As shown in Fig. 8 and 9, the only significant difference between the two systems occurs during the initial transient of the DC-link voltage. As the voltage controller response is much slower, the transient error owed to the simplification has no effect. The agreement between the responses of both models during the main transient shows that the simplifications were justified and that the voltage controller was correctly parameterized.

Additionally, the enlarged transient of i_q in Fig. 9 corroborates the duration of the transient obtained from (13).

6 Experimental results

6.1 Experimental setup

Detection algorithm and post-fault operation were tested on a laboratory back-to-back setup consisting of

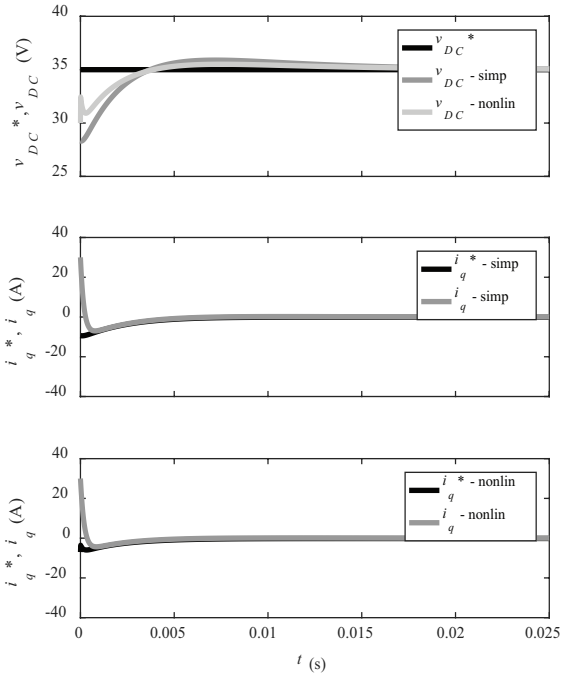

Figure 8: Transient response of simplified ("simp") and fully nonlinear ("nonlin") model in motoring mode.

two identical PMSM drives with independent battery power supplies, thus enabling four-quadrant operation (see Figs. 10-11). Control and detection algorithm (running at 6 kHz) was implemented on a motor controller build around ARM Cortex M4 MCU with support for floating-point arithmetic. The drive under test is

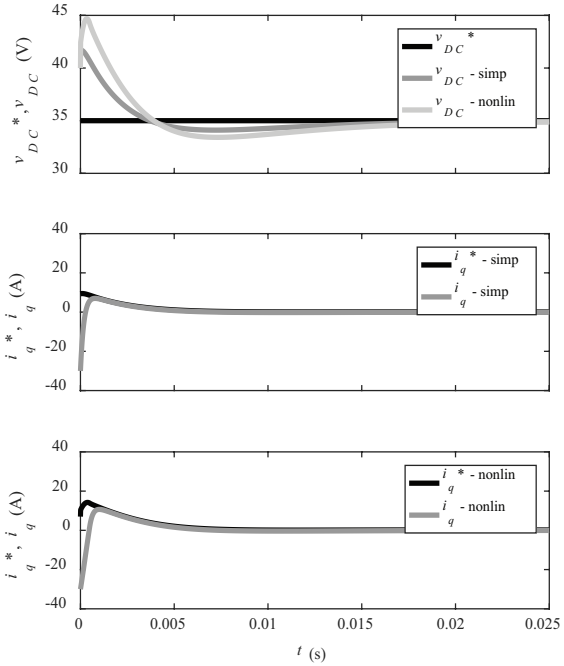

Figure 9: Transient response of simplified ("simp") and fully non-linear ("nonlin") model in generator mode.

torque-controlled, which is the usual operation mode in traction applications. A second coupled drive emulates the mechanical load by running at a controlled speed. Power electronics is integrated into both motors' housings. Fault emulation was performed by switching off the contactor of the torque controlled drive.

Inverter and power supply parameters are shown in Table 1, while the machine parameters are given in Table 2.

Table 1: DC Supply parameters

Symbol	Value	Unit
v_{oc}	34.5	(V)
R_i	86	(mΩ)
R_c	94	(mΩ)
L_c	3.82·10-6	(H)
r_c	0.6	(mm)
d_c	0.1	(m)
l_c	1.8	(m)
C_{DC}	1.4	(mF)
R_{esr}	94.1	(mΩ)
k_i	0.5	/

Table 2: PMSM parameters

Symbol	Value	Unit
R_s	28.5	(mΩ)
L_d	164	(mH)
L_q	186	(mH)
Ψ_m	0.022	(Wb)
p_p	4	/

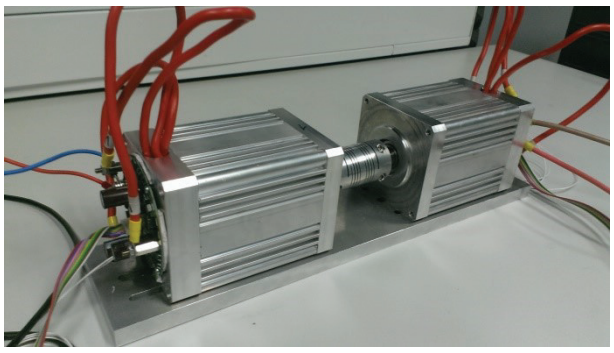

Figure 10: Experimental setup with back-to-back configuration.

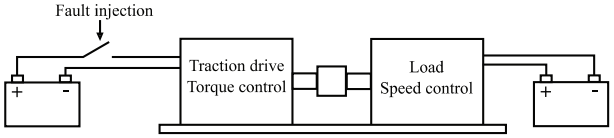

Figure 11: Schematic of the experimental setup.

6.2 Fault detection

Firstly, the performance of the DC-link voltage observer for fault detection, described in section 3, is shown under normal operation [23]. As we can see (fig. 12), the observer tracks the actual voltage during the drive's operating point changes without any significant deviations.

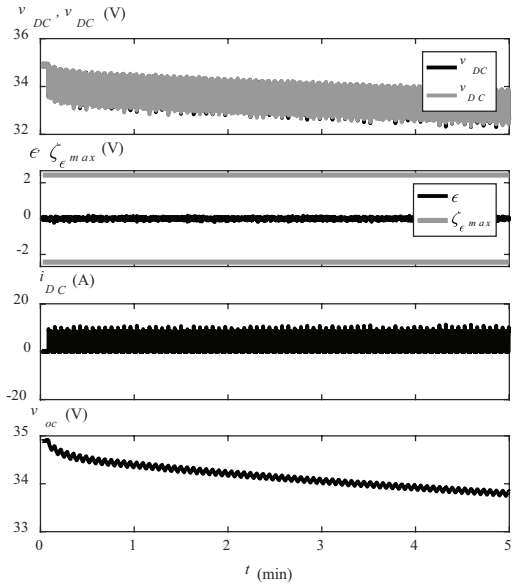

Figure 12: DC supply model response in case of periodic changes of drive's operating point.

The response of the fault detection algorithm during the fault in generator mode is shown in fig. 13. At the instant of the fault, the error between the actual DC-

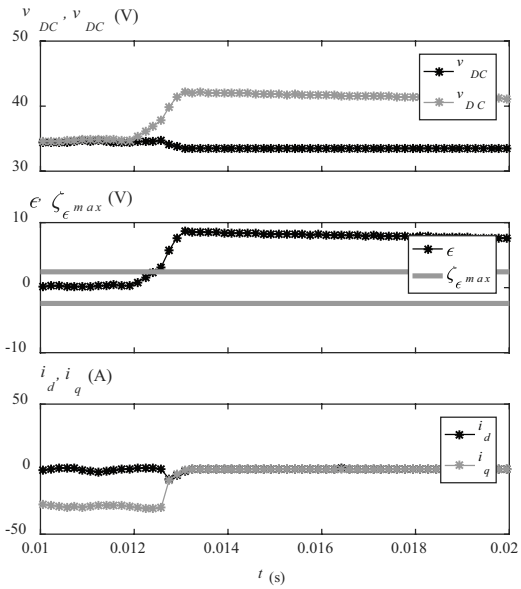

Figure 13: Transient response during a fault in generator mode without voltage controller (1500 rpm, i_q^* = - 30 A).

link voltage and observer output almost immediately exceeds the threshold resulting in instantaneous fault detection. Note that this test is only for demonstration purposes, as no pos-fault action is undertaken.

6.3 Post fault operation

Results in this section show the system response with both the fault detection and post-fault control method activated. A fast voltage control loop response can be observed, as the DC-link voltage stabilizes quickly to the reference value (Fig. 14-15) in both the motor and generator mode. In motor mode (Fig. 14), a short-lasting and minor undervoltage occurs. Hence, the drives with electronics supplied from the DC-link can continue to operate even after the fault. Even more important is the behavior in generator mode (Fig. 15). Here the voltage controller prevents more extended overvoltage, which would occur without a post-fault voltage controller (Fig. 13). Additionally, the overvoltage is very close to the theoretically calculated value from (15), where during generator operation, 46,8 V was measured. In comparison, 46,5 V was calculated from the analytical equation based on system parameters. The combined detection and activation time of four sampling intervals (three for fault detection and one for starting the post-fault mode) was considered for the analytical approach. This confirms the practicality of (15), when designing the drive, thus providing the basis for the maximum voltage ratings of electronic components.

Safe DC-link voltage level with a disconnected power supply can be provided only by the fading kinetic energy of the system's rotating parts. Its duration depends on the actual speed at the instant of the fault and the system's inertia. However, this time should be more than enough for the electronics to enter the safe-stop mode, including the storage of relevant parameters. Hence, almost all of the (kinetic) energy is supporting a low-consuming operation of the control electronics.

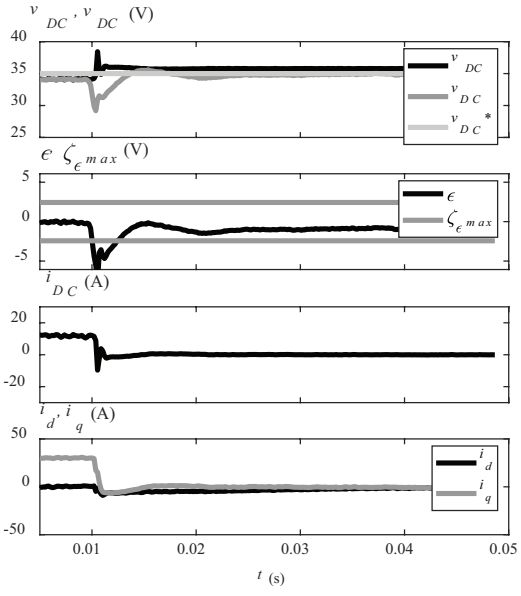

Figure 14: Transient response during a fault in motor mode (1500 rpm, i_q^* = 30 A).

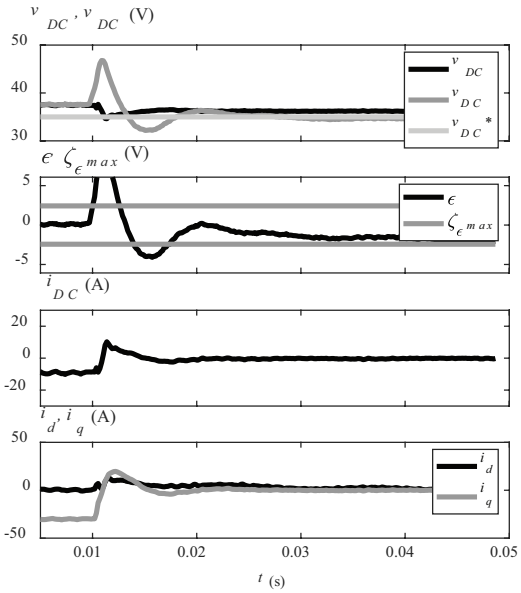

Figure 15: Transient response during fault in generator mode (1500 rpm, i_q^* = - 30 A).

7 Conclusion

This paper proposed an approach to post-fault operation following the malfunctioning of the battery power supply of a PMSM drive. The main goal is to control the level of DC-link voltage and provide for a temporary supply of the controller's electronics before entering the safe-stop mode. The functionality of a post-fault operation, following successful fault detection, has been confirmed by the simulation and experimental results. These also confirm the validity of the analytical terms to determine limit values of DC-link voltage during the transition to the post-fault operation. Further work will focus on applying the concept to more complex configurations of the supply system and methods for dynamic braking.

8 References

1. D. Cabezuelo, E. Ibarra, E. Planas, I. Kortabarria, and J. I. Garate, 'Rare-Earth Free EV and HEV Motor Drives: State of the Art', in *PCIM Europe 2018; International Exhibition and Conference for Power*

Electronics, Intelligent Motion, Renewable Energy and Energy Management, Jun. 2018, pp. 1–8.
2. D. Wanner, *Controlling over-actuated road vehicles during failure conditions*. Stockholm: Engineering Sciences, KTH Royal Institute of Technology, 2015. Accessed: Sep. 29, 2018. [Online]. Available: http://urn.kb.se/resolve?urn=urn:nbn:se:kth:diva-166819
3. J. Zheng, Z. Wang, D. Wang, Y. Li, and M. Li, 'Review of fault diagnosis of PMSM drive system in electric vehicles', in *2017 36th Chinese Control Conference (CCC)*, Jul. 2017, pp. 7426–7432. https://doi.org/10.23919/ChiCC.2017.8028529.
4. Y. Da, X. Shi, and M. Krishnamurthy, 'Health monitoring, fault diagnosis and failure prognosis techniques for Brushless Permanent Magnet Machines', in *2011 IEEE Vehicle Power and Propulsion Conference*, Sep. 2011, pp. 1–7. https://doi.org/10.1109/VPPC.2011.6043248.
5. A. M. El-Refaie, 'Fault-tolerant permanent magnet machines: a review', *IET Electr. Power Appl.*, vol. 5, no. 1, pp. 59–74, Jan. 2011, https://doi.org/10.1049/iet-epa.2009.0117.
6. T. A. Najafabadi, F. R. Salmasi, and P. Jabehdar-Maralani, 'Detection and Isolation of Speed-, DC-Link Voltage-, and Current-Sensor Faults Based on an Adaptive Observer in Induction-Motor Drives', *IEEE Trans. Ind. Electron.*, vol. 58, no. 5, pp. 1662–1672, May 2011, https://doi.org/10.1109/TIE.2010.2055775.
7. J. O. Estima, N. M. A. Freire, and A. J. M. Cardoso, 'Recent advances in fault diagnosis by Park's vector approach', in *2013 IEEE Workshop on Electrical Machines Design, Control and Diagnosis (WEMDCD)*, Mar. 2013, pp. 279–288. https://doi.org10.1109/WEMDCD.2013.6525187.
8. W. Zhang, D. Xu, P. N. Enjeti, H. Li, J. T. Hawke, and H. S. Krishnamoorthy, 'Survey on Fault-Tolerant Techniques for Power Electronic Converters', *IEEE Trans. Power Electron.*, vol. 29, no. 12, pp. 6319–6331, Dec. 2014, https://doi.org/10.1109/TPEL.2014.2304561.
9. L. Mathe, C. Kopacz, L. Bede, and P. O. Rasmussen, 'Sensor-fault tolerant control of PMSM in flux-weakening operation using LKF observer', in *Railway and Ship Propulsion 2012 Electrical Systems for Aircraft*, Oct. 2012, pp. 1–6. https://doi.org/10.1109/ESARS.2012.6387427.
10. S. K. E. Khil, I. Jlassi, J. O. Estima, N. Mrabet-Bellaaj, and A. J. M. Cardoso, 'Detection and isolation of open-switch and current sensor faults in PMSM drives, through stator current analysis', in *2017 IEEE 11th International Symposium on Diagnostics for Electrical Machines, Power Electronics and Drives (SDEMPED)*, Aug. 2017, pp. 373–379. https://doi.org/10.1109/DEMPED.2017.8062382.
11. J. Fang, W. Li, H. Li, and X. Xu, 'Online Inverter Fault Diagnosis of Buck-Converter BLDC Motor Combinations', *IEEE Trans. Power Electron.*, vol. 30, no. 5, pp. 2674–2688, May 2015, https://doi.org/10.1109/TPEL.2014.2330420.
12. H. Al-Sheikh, O. Bennouna, G. Hoblos, and N. Moubayed, 'Modeling, design and fault analysis of bidirectional DC-DC converter for hybrid electric vehicles', in *2014 IEEE 23rd International Symposium on Industrial Electronics (ISIE)*, Jun. 2014, pp. 1689–1695. https://doi.org/10.1109/ISIE.2014.6864869.
13. Y. Cai, L. Lu, P. Shen, X. Feng, H. Wang, and M. Ouyang, 'Online Weld Breakage Diagnosis for the Battery of Electric Vehicle: A Data-Driven Approach', in *2016 IEEE Vehicle Power and Propulsion Conference (VPPC)*, Oct. 2016, pp. 1–5. https://doi.org/10.1109/VPPC.2016.7791739.
14. C. Wu, C. Zhu, Y. Ge, and Y. Zhao, 'A review on fault mechanism and diagnosis approach for Li-ion batteries', *J. Nanomater.*, vol. 2015, pp. 1–9, 2015.
15. United Nations Economic Commission for Europe (United Nations Economic and Social Council), 'Regulation No 94 — Uniform provisions concerning the approval of vehicles with regard to the protection of the occupants in the event of a frontal collision'. Sep. 20, 2012.
16. Z. Ke, J. Zhang, and M. W. Degner, 'DC Bus Capacitor Discharge of Permanent-Magnet Synchronous Machine Drive Systems for Hybrid Electric Vehicles', *IEEE Trans. Ind. Appl.*, vol. 53, no. 2, pp. 1399–1405, Mar. 2017, https://doi.org/10.1109/TIA.2016.2636279.
17. V. R. Jevremović and B. Jeftenić, 'An Efficient Braking Algorithm for Interior Permanent Magnet Synchronous Motors', Nov. 2005.
18. S. M. Yang and J. Y. Chen, 'Controlled Dynamic Braking for Switched Reluctance Motor Drives With a Rectifier Front End', *IEEE Trans. Ind. Electron.*, vol. 60, no. 11, pp. 4913–4919, Nov. 2013, https://doi.org/10.1109/TIE.2012.2233696.
19. Y. Wang and R. D. Lorenz, 'Creative usage of stator flux linkage to fast brake electric vehicles', in *2016 IEEE Transportation Electrification Conference and Expo (ITEC)*, Jun. 2016, pp. 1–6. https://doi.org/10.1109/ITEC.2016.7520278.
20. G. D. Marques and M. F. Iacchetti, 'Sensorless Frequency and Voltage Control in the Stand-Alone DFIG-DC System', *IEEE Trans. Ind. Electron.*, vol. 64, no. 3, pp. 1949–1957, Mar. 2017, https://doi.org/10.1109/TIE.2016.2624262.
21. T. Guo, J. Liu, S. Vazquez, L. Wu, H. Gao, and L. G. Franquelo, 'Predictive direct power control for grid-connected power converters with an Extended State Observer based dc-link voltage regulator', in *2016 IEEE 25th International Sympo-*

sium on Industrial Electronics (ISIE), Jun. 2016, pp. 1218–1223. https://doi.org/10.1109/ISIE.2016.7745068.

22. B. K. Bose and P. M. Szczesny, 'A microcomputer-based control and simulation of an advanced IPM synchronous machine drive system for electric vehicle propulsion', *IEEE Trans. Ind. Electron.*, vol. 35, no. 4, pp. 547–559, Nov. 1988, https://doi.org/10.1109/41.9178.
23. M. Breznik, V. Ambrožič, and M. Nemec, 'Detection of open circuit fault in battery power supply feeding permanent magnet synchronous motor', *IET Power Electron.*, vol. 11, no. 14, pp. 2377–2384, 2018, https://doi.org/10.1049/iet-pel.2018.5214.
24. H. A. Aebischer and B. Aebischer, 'Improved formulae for the inductance of straight wires', *Adv. Electromagn.*, vol. 3, no. 1, pp. 31–43, 2014.
25. S. K. Kommuri, M. Defoort, H. R. Karimi, and K. C. Veluvolu, 'A Robust Observer-Based Sensor Fault-Tolerant Control for PMSM in Electric Vehicles', *IEEE Trans. Ind. Electron.*, vol. 63, no. 12, pp. 7671–7681, Dec. 2016, https://doi.org/10.1109/TIE.2016.2590993.
26. C.-H. Park, D.-Y. Kim, H.-B. Yeom, Y.-D. Son, and J.-M. Kim, 'A Current Reconstruction Strategy Following the Operation Area in a 1-Shunt Inverter System', *Energies*, vol. 12, no. 8, p. 1423, Jan. 2019, https://doi.org/10.3390/en12081423.
27. S. Skogestad, 'Simple analytic rules for model reduction and PID controller tuning', *J. Process Control*, vol. 13, no. 4, pp. 291–309, Jun. 2003, https://doi.org/10.1016/S0959-1524(02)00062-8.

Arrived: 05. 10. 2021
Accepted: 28. 01. 2022

Original scientific paper
https://doi.org/10.33180/InfMIDEM2022.104

Informacije MIDEM
Journal of Microelectronics,
Electronic Components and Materials
Vol. 52, No. 1(2022), 29 – 39

Throughput Estimation of K-zone Gbps Radio Links Operating in the E-band

Attila Hilt[1,2]

[1]Nokia Cloud and Network Services, Budapest, Hungary
[2]Department of Broadband Infocommunications and Electromagnetic Theory, Faculty of Electrical Engineering and Informatics, BME, Budapest University of Technology and Economics, Budapest, Hungary

Abstract: Nowadays covid virus changes our work, learning and life-style. Broadband telecommunication channels are required for remote work, e-learning and video conferencing. Optical-fiber access offers the required wide bandwidths and low latencies. However, due to technical and business reasons optical-fiber cannot yet reach all homes, all offices or industrial plants. Mobile network sites often meet similar problems in urban environment. Since the introduction of mobile data (e.g., High-Speed Packet Access in 3G networks) and with the actual 4G expansion and 5G deployments, more and more cell-sites are connected to the fiber backhaul. But not all radio nodes can benefit the enormous bandwidth provided by optical-fiber access. The missing section between the fiber end-point and the site is often only few hundred meters, one or two kilometers. More and more millimeter-wave radios are deployed to reach the fiber access point. As radio links suffer from rain, atmospheric attenuation and interference, careful design is required. This paper focuses on digital radio links operating in the *E*-band (71-86 GHz) in Central Europe, where rainfall rates reach 42 mm/h (e.g., Slovenia and Hungary). In the paper a step-by-step planning method is shown to estimate the yearly radio throughput. It is shown that E-band radio links can reach Gigabit/s (Gbps) speed and availability figures comparable to optical-fiber connections.

Keywords: fiber/wireless system; millimeter-wave; *E*-band; Gbps radio access; adaptive modulation; throughput; rainfall

Ocena zmogljivosti gigabitne radijske zveze v območju K v pasu E

Izvleček: Danes virus covid spreminja naše delo, učenje in življenjski slog. Za delo na daljavo, e-učenje in videokonference so potrebni širokopasovni telekomunikacijski kanali. Dostop z optičnimi vlakni ponuja zahtevane široke pasovne širine in nizke zakasnitve. Vendar zaradi tehničnih in poslovnih razlogov optična vlakna še ne morejo doseči vseh domov, pisarn ali industrijskih obratov. Mobilna omrežna mesta se v mestnem okolju pogosto srečujejo s podobnimi težavami. Od uvedbe mobilnih podatkov (npr. hitri paketni dostop v omrežjih 3G) ter z dejanskim širjenjem omrežja 4G in uvajanjem omrežja 5G je vse več lokacij priključenih na optično hrbtno povezavo. Vendar pa vsa radijska vozlišča ne morejo izkoristiti ogromne pasovne širine, ki jo zagotavlja dostop z optičnimi vlakni. Manjkajoči odsek med končno točko optičnega omrežja in lokacijo je pogosto le nekaj sto metrov, en ali dva kilometra. Razvitih je ved več radijskih sprejemnikov z milimetrskimi valovi, da bi dosegli dostopno točko z optičnimi vlakni. Ker so radijske povezave izpostavljene dežju, atmosferskemu slabljenju in motnjam, je potrebno skrbno načrtovanje. Članek se osredotoča na digitalne radijske povezave, ki delujejo v pasu *E* (71-86 GHz) v Srednji Evropi, kjer količina padavin doseže 42 mm/h (npr. v Sloveniji in na Madžarskem). V članku je prikazana metoda načrtovanja po korakih za oceno letne radijske prepustnosti. Pokazano je, da lahko radijske povezave v pasu E dosežejo hitrosti gigabit/s (Gb/s) in razpoložljivost, primerljivo s povezavami z optičnimi vlakni.

Ključne besede: optični/brezžični sistem; milimetrski valovi; gigabitni radijski dostop; *E* pas; prilagodljiva modulacija; prepustnost; stopnja padavin

** Corresponding Author's e-mail: attila.hilt@nokia.com, hilt.attila@vik.bme.hu*

How to cite:
A. Hilt, "Throughput Estimation of K-zone Gbps Radio Links Operating in the E-band", Inf. Midem-J. Microelectron. Electron. Compon. Mater., Vol. 52, No. 1(2022), pp. 29–39

1 Introduction

There is an intensive ongoing research of combined fiber-optical/wireless networks [1]-[6]. Remarkably, the investigations of using microwave and millimeter-wave (μW/mmW) frequencies in combined fiber/wireless networks started more than two decades ago [7]-[11]. In both fixed and mobile access systems, the optical fibers are deployed to reach the end-users as close as possible. The actual covid virus changed our workstyle. Remote work, e-learning and videoconferencing require broadband access. Fiber access systems, such as FTTH (Fiber-to-the-Home, Fig. 1.a) and FTTO (Fiber-to-the-Office, Fig. 1.b) became even more important during pandemic times [12]. The optical fiber can provide the required bandwidth for the users. The wireless part e.g., WiFi can provide some mobility in FTTH or FTTO access systems, when needed.

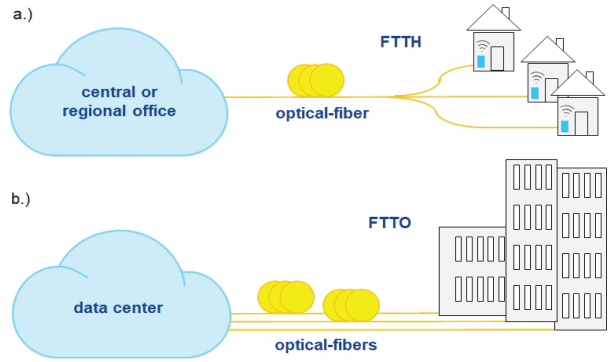

Figure 1: a.) Fiber-to-the-Home and b.) Fiber-to-the-Office systems.

In 2G (2nd generation) and early 3G (3rd generation) mobile systems fiber-optical technology was mainly used in the core and transport parts of the network [13]-[14]. With the introduction of HSPA (High Speed Packet Access) and LTE (Long Term Evolution) broadband for mobile data became a reality. FTTS (Fiber-to-the-Site) turned out to be more and more important. As shown in Fig. 2, new and newer Radio Access Technologies (RATs) like 4G, 5G employ FTTS wherever it is possible.

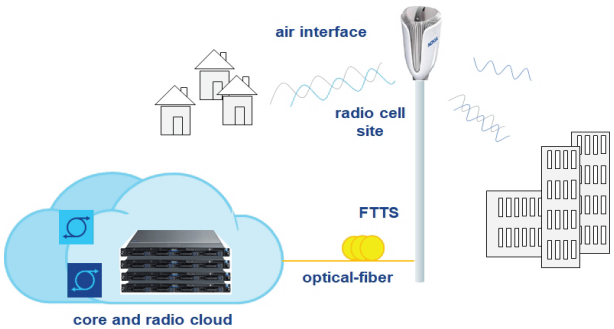

Figure 2: Fiber-to-the-Site.

Beside the enormous bandwidth, optical fibers can provide the low latency that are essential requirements in 5G and future 6G mobile systems [15]-[16]. The wireless μW/mmW access part offers mobility for the end users.

Unfortunately, the initial deployment of optical fibers is a slow and expensive process. Especially in urban environment, the installation of optical cables may require heavy construction works (i.e., cable tunnels) resulting in temporary closure of pavements and street sections. Thus, optical fibers cannot yet reach all the radio cell sites. In several cases a few hundred meters gap remains between the optical-fiber end-point or 'aggregation point' and the cell-site or end user. In such scenarios, *E*-band millimeter-wave fixed radio links can connect the last few-hundred meters where optical fiber is not yet laid down (Fig. 3). It is important to mention, that these Gigabit/s radio connections can be re-used later on at other sites, when optical fiber finally arrives. In practice, the very dense fixed radio and optical network is continuously evolving in big cities (Fig. 3). The radio links are getting shorter and shorter, but higher and higher transmission capacities are expected.

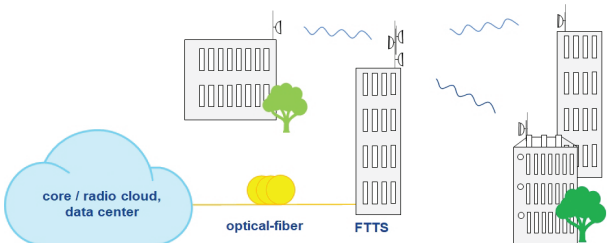

Figure 3: Fiber-radio access node.

This paper reviews the main characteristics of the *E*-band radios and summarizes the planning steps of these links. As shown, clearance and rainfall are the main factors determining link availability. Finally, calculation results are shown for *K* rain-zone that covers Central Europe, including Slovenia and Hungary. In the given design example, average link throughput is estimated. It is shown that state-of-the-art *E*-band radios can bring 'fiber-availability' with proper radio link design.

2 Line-of-Sight E-band radio links

μW/mmW radio links offer a good solution to connect the fiber-end-point with the nearby site or office. An important design rule is that the radio links require clean Line-of-Sight (LoS). Obstacles, especially metal objects may cause unwanted reflections. When the direct radio wave and the reflected wave arrive to the

receiving antenna with opposite phase, the two signals cancel each other. Even though the exact cancellation happens at one (or multiple) discrete frequency, the attenuation due to non-satisfactory clearance can be significant for wide bandwidth (BW) radio signals too. In practice the LoS condition is estimated with the clearance of the first Fresnel-zone. The radius of the *n*-th Fresnel-ellipsoid is calculated as [17], [18]:

$$F_n\left[\mathrm{m}\right]=\sqrt{n\cdot\frac{d_1\cdot d_2}{d_1+d_2}\cdot\lambda}=\sqrt{c\cdot n\cdot\frac{d_1\cdot d_2}{f\cdot d}} \quad (1)$$

Where $d=d_1+d_2$ is the total hop length of the link, f is the frequency and $c\approx 299.7\cdot 10^8$ m/s is the speed of light in free space. As shown in Fig. 4, d_1 and d_2 are the distances measured from the axial observation point to antenna 1 and antenna 2, respectively. To avoid doubts, in the coming equations units are indicated in brackets. Eq. (1) simplifies for the first Fresnel-zone with n=1. When d is given in km and f is given in GHz, then:

$$F_1\left[\mathrm{m}\right]=17.312\sqrt{\frac{d_1\cdot d_2}{f\cdot d}} \quad (2)$$

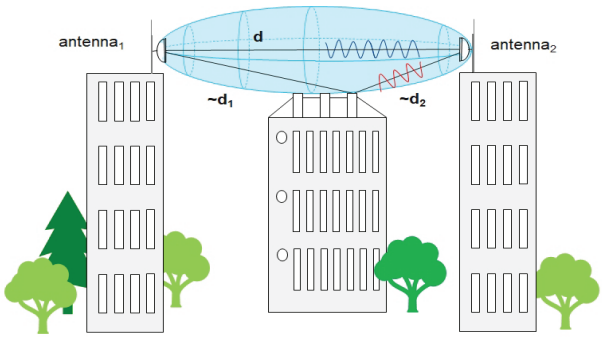

Figure 4: Unwanted reflection from an obstacle in the first Fresnel-zone.

Please note, that equation (2) has different forms when frequency and distance are given in other units [17], [18]. Let us consider an *E*-band radio, operating at f=71.125 GHz with a hop length of d = 1.2 km. The maximum radius of the first Fresnel-ellipsoid is at the middle of the link where $d_1=d_2=d/2$:

$$F_1\left[\mathrm{m}\right]\cong 17.312\sqrt{\frac{d}{2}\cdot\frac{d}{2}\cdot\frac{1}{f\cdot d}}=8.656\sqrt{\frac{d\left[\mathrm{km}\right]}{f\left[\mathrm{GHz}\right]}}\cong 1.1\left[\mathrm{m}\right], \quad (3)$$

In practice, a narrow ø 2.2 m diameter ellipsoid shall be clean between the two transceivers of the radio link. As an initial check, the LoS condition is usually investigated first in a radio link planning tool. An example path profile is shown in Fig. 5, as it is seen in IQ-Link tool [19]. For the proper design accurate coordinates are necessary. A useful help if a high-resolution digital terrain model is added to the link planning tool. Clutter info and three-dimensional (3D) building data can make the preliminary LoS check more reliable.

Figure 5: Path profile of the mmW radio link, as seen in the IQ-link planning tool [19].

An attractive LoS estimation is possible by visualizing the planned link in Google-Earth three dimensional plot. Figure 6 shows the d=1.2 km long link designed in an inner district of Budapest. Please note, that computer estimations are never accurate enough in urban environments. Buildings, chimneys, trees, cables or cranes may attenuate or block completely the *E*-band link. Site visits are necessary to confirm LoS before constructing the *E*-band link. In the rest of this paper a clear LoS condition is assumed.

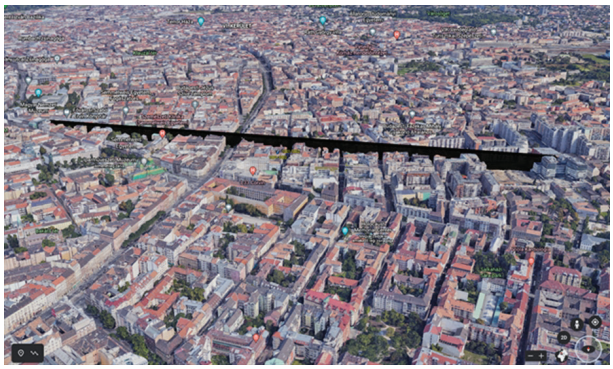

Figure 6: Line-of-Sight estimation using Google Earth in the microwave link design.

3 Radios with adaptive modulation

For calculation simplicity, in the paper a single *E*-band radio connection is investigated. To calculate aggregat-

ed throughput of dual frequency or dual polarization radio links (e.g., 23 GHz and *E*-band radios combined onto one dual-band antenna) is not discussed. But the presented design method can be extended to include the lower frequency band or the other polarization too.

The main characteristics of the *E*-band millimeter-wave digital radios are demonstrated in the following by selecting the Nokia 'Wavence' radio. Wavence radio family uses adaptive modulation [20]. It is emphasized that the presented design method is general, and applicable for any other state-of the-art *E*-band digital radio having adaptive modulation [17]-[22]. In case of fading, adaptive modulation radios automatically switch to simpler modulation mode. Simpler modulation modes are less sensitive to attenuation. Thus, the radio connection is not lost. The transmission is maintained, even though the radio throughput is reduced to a lower bit rate [17]-[22].

For simplicity, in Table 1, the radio parameters are given only for the 250 MHz, 500 MHz, 1 GHz and 2 GHz radio frequency (RF) bandwidth (BW) settings. As seen, the modulation mode can vary from 512-QAM (Quadrature Amplitude Modulation) to QPSK (Quadrature Phase Shift Keying) and BPSK (Binary Phase Shift Keying). The Wavence radio RF bandwidth can be set to 62.5 MHz, 125 MHz, 250 MHz, 500 MHz, 750 MHz, 1 GHz, 1.25 GHz, 1.5 GHz or 2 GHz. The values listed in Table 1 are typical equipment values specified for the Bit Error Rate of $BER=10^{-6}$. System Gain (SG, in decibel) is defined as the difference of the transmit (Tx) power and the receiver (Rx) threshold level:

$$SG_{\text{mod}-n}\left[\text{dB}\right] = P_{\text{Tx}}\left[\text{dBm}\right] - P_{\text{Rxth}}\left[\text{dBm}\right]. \quad (4)$$

Table 1: Tipical *E*-band radio parameters

BW	250 MHz	500 MHz	1 GHz	2 GHz
Modulation	System Gain [dB] at BER=10^{-6}			
BPSK 1/4		94.7	91.4	86
BPSK 1/2	94.9	91.7	88.4	83
BPSK	91.9	88.7	85.4	80
QPSK	88.9	85.7	82.4	77
16-QAM	80.3	77.2	73.8	67.9
32-QAM	77.2	74.1	70.7	64.7
64-QAM	74.3	71.1	67.6	58
128-QAM	71.2	66.9	63.3	54.3
256-QAM	66	62.7	58	
512-QAM	61	57.5		

In Eq. (4) mod-*n* refers to the actual modulation mode that is adaptively varying between BPSK 1/4 and 512-QAM, according to propagation conditions. In practice, we have as many System Gain figures as many modulation modes are available in the selected channel BW. BPSK 1/2 denotes a BPSK modulation where the RF channel is halved. When the same signal power remains with half of the noise in the receiver, the SG is increased with 3 dB. Similarly, BPSK 1/4 reduces the BW to its quarter, so SG is 6 dB better than that of BPSK. (It is important to specify *BER* properly when SG and Fading Margin (FM) figures are given. Please note, that Rx thresholds for $BER=10^{-3}$ are lower than for $BER=10^{-6}$. As SG values at $BER=10^{-3}$ are higher, it is important to check, which figures are used to avoid planning mistake.) In Eq. (4), antenna gain is not added into the definition of SG. Note, that other definition exists too [22].

4 Link design and rain attenuation

Having the System Gain values for the different modulation modes in the selected RF bandwidth, it is possible to calculate the Fading Margin of the link. In this part we discuss the main fading factors. It is shown that rainfall has the most severe effect on the transmission quality. As shown, FM can be consumed by atmospheric and rain attenuation. During sunny days high FM is not required. Automatic Transmit Power Control (ATPC) can reduce output power to avoid unwanted interference in other links and to save energy. Threshold degradation due to radio-interference from other links is not discussed here. It is an assumption that radio channel is properly selected.

4.1 Fading margin calculation

The radio-link operates with a given modulation mode, as long as its Fading Margin is higher than the sum of all kind of different link losses:

$$FM_{\text{mod}-n}^{[\text{dB}]} > A_{\text{rain}}^{[\text{dB}]} + A_{\text{atm}}^{[\text{dB}]} + A_{\text{obst}}^{[\text{dB}]}. \quad (5)$$

In our design a clean LoS condition is considered, so there is no obstacle loss, A_{obst} is zero. FM remains for the main propagation factors of rain attenuation (A_{rain}) and atmospheric attenuation (A_{atm}). Without losing validity of the statements, in the following *B*W = 1 GHz bandwidth is selected in the calculation examples. In Eq. (5) mod-*n* again refers to the actual modulation mode. It can vary between BPSK 1/4, BPSK 1/2, BPSK, QPSK, 16-QAM, 64-QAM, 128-QAM and 256-QAM. For 1 GHz BW the corresponding Ethernet throughput figures are 200, 400, 800 Mbps, 1.6, 3.2, 4, 5.6 and 6.4 Gbps, respectively. If link losses consume the fade margin, the link automatically changes its modulation mode to a less sensitive one. Fading Margin is calculated as [22]:

$$FM^{[\mathrm{dB}]} = P_{\mathrm{Tx}}^{[\mathrm{dBm}]} + G_{\mathrm{Tx}}^{[\mathrm{dBi}]} + G_{\mathrm{Rx}}^{[\mathrm{dBi}]} - FSL^{[\mathrm{dB}]} - P_{\mathrm{Rxth}}^{[\mathrm{dBm}]}, \quad (6)$$

where G_{TX} and G_{RX} are the transmit and receive antenna gain values and *FSL* denotes the Free Space Loss:

$$FSL^{[\mathrm{dB}]} = 92.44 + 20log_{10}\left(f^{[\mathrm{GHz}]}\right) + 20log_{10}\left(d^{[\mathrm{km}]}\right). \quad (7)$$

Combining equations (4) and (6):

$$FM_{\mathrm{mod}-n}^{[\mathrm{dB}]} = SG_{\mathrm{mod}-n}^{[\mathrm{dB}]} + G_{\mathrm{Tx}}^{[\mathrm{dBi}]} + G_{\mathrm{Rx}}^{[\mathrm{dBi}]} - FSL^{[\mathrm{dB}]}. \quad (8)$$

It is visible in Eq. (8), that for a given frequency (*E*-band), and given link distance, only a few parameters remain free: BW, antenna size and modulation mode. Nokia Wavence radios can have ø 12 cm integrated antennas or slip mount antennas. Table 2 below summarizes the possible Tx and Rx antenna combinations and their overall Gain. The 1 foot and 2 feet antennas are calculated with their mid-band gain, as specified in [23]-[24].

Increasing the fade margin by proper link design, the rain attenuation can be compensated and thus the throughput of the digital link can be maximized. The following calculations are performed with different single-polarization antenna sizes according to Table 2.

Table 2: Antenna pairs and their Gain

antenna diameters ø [cm]	Antenna Gain and type			
	G_{Tx} [dBi]	G_{Rx} [dBi]	$G_{Tx} + G_{Rx}$ [dB]	single, linear polarization
12 – 12	38	38	76	integrated
12 – 38	38	43.5	81.5	int. + VHLP1
38 – 38	43.5	43.5	87	VHLP1 [23]
38 – 66	43.5	50.5	94	VHLP1+VHLP2
66 – 66	50.5	50.5	101	VHLP2 [24]

4.2 Calculation of atmospheric attenuation

Atmospheric attenuation is caused by the absorption of gaseous particles in the air [25]. Water vapor causes extra attenuation of 0.2 dB/km around 23 GHz and 12 dB/km around 180 GHz. High attenuation peaks are caused by oxygen absorption in the 56–64 GHz (16 dB/km) and in the 120 GHz (2 dB/km) range [25]-[27].

Compared to rain attenuation, atmospheric attenuation is negligible for short links at the 71-86 GHz communication frequencies of *E*-band. In the calculations, specific attenuation of γ_{atm}=0.4 dB/km is used [25]. The total atmospheric attenuation is calculated for the entire link length using the specific attenuation:

$$A_{\mathrm{atm}}\left[\mathrm{dB}\right] = \gamma_{\mathrm{atm}}\left[\mathrm{dB/km}\right] \cdot d\left[\mathrm{km}\right] \quad (9)$$

The entire atmospheric attenuation for a *d*=1.2 km long link is less than 0.5 dB. For practical calculation reasons, the Fade Margin discussed in part 4.1 is decreased with this linear atmospheric attenuation value. A new fade margin figure can be introduced, a FM that remains only for the rain fading for clean LoS paths:

$$FM_{\mathrm{mod}-n}^{[dB]} - A_{\mathrm{atm}}^{[\mathrm{dB}]} > A_{\mathrm{rain}}^{[\mathrm{dB}]}. \quad (10)$$

Equation (10) is similar to Eq. (5), but this form is more useful for numerical calculations. As it is shown in the next part, rain attenuation calculation leads to an equation that is difficult to solve mathematically. However, with a simple program it is easy to calculate the results numerically.

4.3 Calculation of rain Attenuation for K-zone

According to ITU-R (Radiocommunication Sector of the International Telecommunication Union), the attenuation of radio waves due to rainfall can be estimated as:

$$\gamma_{\mathrm{rain}}\left[\mathrm{dB/km}\right] = kR^{\alpha} \quad (11)$$

where *R* is the rainfall-rate, given in mm/h [28]. Constants *k* and α depend on the frequency and polarization (either vertical or horizontal) of the link [28]. γ_{rain} is the specific attenuation of rain in dB/km units. When constants *k* and α are plotted as a function of frequency, it is visible that the horizontal and vertical values are very similar in the 71-86 GHz band (shadowed with blue in Fig. 7). Unlike in the traditional 18-38 GHz communication bands (shadowed with grey in Fig. 7), the polarization of the radio link has seemingly less impact on rain attenuation in the *E*-band. This can be explained by stormy winds that are usually accompanying intensive rainfalls, thus modifying the vertical direction of rain, and by the short wavelengths of λ = 4.2…3.5 mm. Naturally, the model is to be verified with real radio measurements, that are possible with state-of the-art *E*-band radios. For this purpose, long

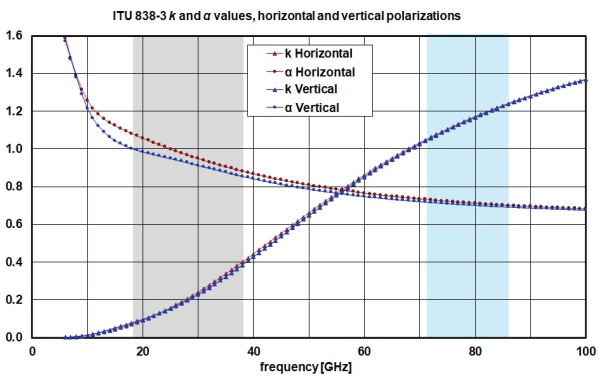

Figure 7: *k* and α parameters according to ITU [28]

term measurements are running in experimental links [26],[27],[29],[30].

The rain attenuation can be estimated following ITU-R P.530 [31]:

$$A_{0.01\%}\left[\mathrm{dB}\right] = \gamma_{\mathrm{rain}} \frac{d}{1 + d / 35 \cdot e^{-0.015 \cdot R_{0.01\%}}} \qquad (12)$$

$A_{0.01\%}$ means rain attenuation, that is exceeded in 0.01% of the time. Please note that Eq. (12) is recommended up to maximum R=100 mm/h rainfall rates. Central European countries falling into K rain-zone satisfy this constraint with the value of $R_{0.01\%}$ = 42 mm/h [22], [32]. Finally, combining Equations (10), (11) and (12) we get:

$$FM_{\mathrm{mod}-n}^{[dB]} - A_{\mathrm{atm}}^{[\mathrm{dB}]} > k \cdot R_{0.01\%}^{\alpha} \frac{d}{1 + d / 35 \cdot e^{-0.015 \cdot R_{0.01\%}}}. \qquad (13)$$

Equation (13) raises some difficulties. First, it gives estimation only for the 0.01% of time, when the rainfall is 42 mm/h or more intensive. This means, that we can split the radio modulation modes into two groups only. One group that can survive the rain in 0.01% of the time and another group that cannot tolerate this rainfall intensity. For rain probabilities in the range of p=0.001% to p=1% in time, ITU-R P.530-13 recommends the estimation for latitudes of 30° or higher [31]:

$$A_p\left[\mathrm{dB}\right] = 0.12 \cdot A_{0.01\%}\left[\mathrm{dB}\right] \cdot p^{-(0.546 + 0.043 \cdot log_{10} p)}. \qquad (14)$$

Using Eq. (14), 0.01 % can be extended into the 0.001 % - 1 % range of time, where link availabilities correspond to 99 % - 99.999 %, respectively.

The other difficulty is to find exact mathematical solution of Eq. (13), (14). Here a simple program is used for numerical solution. In a *for* cycle, the hop length can be increased in very small steps (e.g., 10 m) to find the link distance where rain attenuation consumes the fade margin of the link for the modulation mode set. The results are detailed in part 5.

4.4 Local rainfall rate statistics in K-zone

Figure 9 shows rainfall-rates measured by OMSZ, the Hungarian Meteorological Service over two decades in Budapest [33]. OMSZ operates seven meteorological stations in the capital. Fig. 9 shows rain intensities at "Belterület" station where the highest mm/h rainfall intensity was measured in 2015. Similar measurements are published for city Pécs in southern Hungary [34]. As seen from the local measurements, the ITU-T *K* rain-zone of 42 mm/h is a reasonable estimation when designing radio links in Hungary.

Long-term and high-resolution statistics of local rain events are very important to validate the ITU-R recommendations that are used in the link calculations. Beside OMSZ, BME, the Budapest University of Technology and Economics has also a meteorological station to collect long term meteorological data (rainfall rate, temperature, fog, etc.) with high-resolution [30], [35].

4.5 FDD links and the E-band frequency raster

E-band has been introduced for fixed radio communications by CEPT, the European Conference of Postal and Telecommunications Administrations [36]. Without

BW		71 125															73 125
125	R	R1 / R'1	R2 / R'2	R3 / R'3	R4 / R'4	R5 / R'5	R6 / R'6	R7 / R'7	R8 / R'8	R9 / R'9	R10 / R'10	R11 / R'11	R12 / R'12	R13 / R'13	R14 / R'14	R15 / R'15	R16 / R'16
MHz	low fr.	71 187.5	71 312.5	71 437.5	71 562.5	71 687.5	71 812.5	71 937.5	70 062.5	72 187.5	72 312.5	72 437.5	72 562.5	72 687.5	72 812.5	72 937.5	73 062.5
raster	high fr.	81 187.5	81 312.5	81 437.5	81 562.5	81 687.5	81 812.5	81 937.5	80 062.5	82 187.5	82 312.5	82 437.5	82 562.5	82 687.5	82 812.5	82 937.5	83 062.5
250	P	P1 / P'1		P2 / P'2		P3 / P'3		P4 P'4		P5 / P'5		P6 / P'6		P7 / P'7		P8 / P'8	
MHz	low fr.	71 250		71 500		71 750		72 000		72 250		72 500		72 750		73 000	
raster	high fr.	81 250		81 500		81 750		82 000		82 250		82 500		82 750		83 000	
500	S	S1 / S'1				S2 / S'2				S3 / S'3				S4 / S'4			
MHz	low fr.	71 375				71 875				72 375				72 875			
raster	high fr.	81 375				81 875				82 375				82 875			
1	T	T1 / T1								T2 / T2							
GHz	low fr.	71 625								72 625							
raster	high fr.	81 625								82 625							
2	U	U1 / U1															
GHz	low fr.	72 125															
raster	high fr.	82 125															
		81 125															83 125

BW		73 625															75 625
125	R	R21/R'21	R22/R'22	R23/R'23	R24/R'24	R25/R'25	R26/R'26	R27/R'27	R28/R'28	R29/R'29	R30/R'30	R31/R'31	R32/R'32	R33/R'33	R34/R'34	R35/R'35	R36/R'36
MHz	low fr.	73 687.5	73 812.5	73 937.5	74 062.5	74 187.5	74 312.5	74 437.5	74 562.5	74 687.5	74 812.5	74 937.5	75 062.5	75 187.5	75 312.5	75 437.5	75 562.5
raster	high fr.	83 687.5	83 812.5	83 937.5	84 062.5	84 187.5	84 312.5	84 437.5	84 562.5	84 687.5	84 812.5	84 937.5	85 062.5	85 187.5	85 312.5	85 437.5	85 562.5
250	P	P11 / P'11		P12 / P'12		P13 / P'13		P14 / P'14		P15 / P'15		P16 / P'16		P17 / P'17		P18 / P'18	
MHz	low fr.	73 750		74 000		74 250		74 500		74 750		75 000		75 250		75 500	
raster	high fr.	83 750		84 000		84 250		84 500		84 750		85 000		85 250		85 500	
500	S	S6 / S'6				S7 / S'7				S8 / S'8				S9 / S'9			
MHz	low fr.	73 875				74 375				74 875				75 375			
raster	high fr.	83 875				84 375				84 875				85 375			
1	T	T3 / T3								T4 / T4							
GHz	low fr.	74 125								75 125							
raster	high fr.	84 125								85 125							
2	U	U2 / U2															
GHz	low fr.	74 625															
raster	high fr.	84 625															
		83 625	note: 750 MHz raster is not shown														85 625

Figure 8: A section of the E-band frequency allocation table with different RF bandwidths (BW).

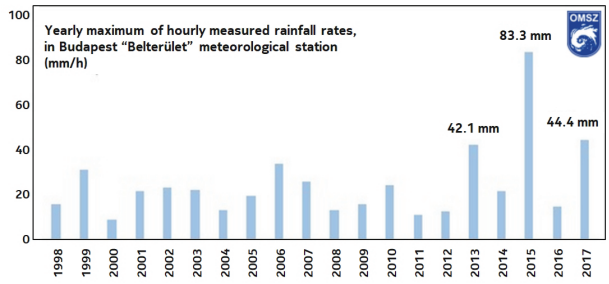

Figure 9: Yearly peak rainfall rates (mm/h) inside the territory of Budapest [33]

completeness, the frequency raster is shown in Fig. 8 (750 MHz channels are not indicated). The Frequency Division Duplex (FDD) spacing between the high (H) and the low (L) frequencies is:

$$\Delta f = f_H - f_L = 10\,\text{GHz}. \tag{15}$$

Δ*f* is the 'go-return' frequency separation between the transmit and receive directions. The center frequencies are shown in Fig. 8 for the 125, 250, 500 MHz, 1 and 2 GHz bandwidth options. As seen in Fig. 8, the frequency of the low band-edge is 71 125 MHz. The Fresnel-ellipsoid has the largest diameter at this frequency. The frequency of the high band-edge is 85 625 MHz. The parabolic antennas have higher gain here, but *FSL* is also higher (Eq. 7). There are four 1 GHz wide radio bands in the raster, marked as T1/T'1, T2/T'2, T3/T'3 and T4/T'4.

5 Calculation results

Calculations have been carried out using the described method. The results are summarized in two set of plots. Antenna pairs are varying in the plots starting with ø 12- 12 cm (lowest gain) to ø 66-66 cm (highest gain). The first plot is given for a fixed hop length of a 1.2 km link. In the second set of plots, the hop length is a free variable and link availability curves are plotted for the different modulation modes from BPSK ¼ to 256-QAM.

5.1 Throughput for 1.2 km long E-band link

The estimated throughput of the 1.2 km link is calculated as a function of time. Figure 10 shows the portion of the year when fade margin is sufficient to run the link with highest modulation mode of 256-QAM. The time is marked as % of the year on the *x*-axis. In case of intensive rain, the link adaptively changes to a lower modulation mode. Parameter of the curves is the antenna pair. If both ends use ø 12 cm integrated antenna, the link cannot reach 5 Gbps and sensitive to rain. In *K* rain-zone, $R_{0.01\%} = 42$ mm/h or stronger rainfall rate is considered in 0.01 % of the year, this is shown as 99.99 % on the horizontal axis. It is seen in Fig. 10, that ø 38 - 66 cm or ø 66 - 66 cm antenna pairs are suitable to reach 6 Gbps throughput in 99.99 % of the time.

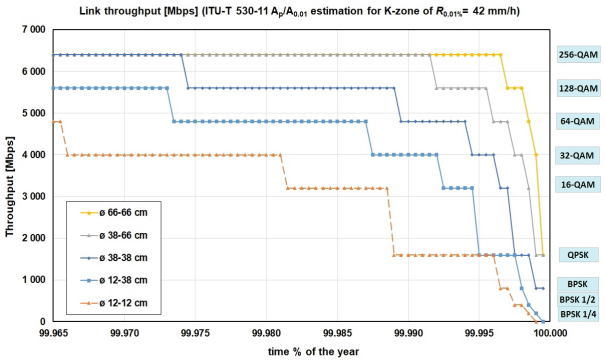

Figure 10: Estimated link throughput as a function time (in % of the year)

It is seen, that with ø 12 cm integrated antenna pairs, the link cannot reach 6 Gbps throughput. The highest modulation mode with this antenna pair is 64-QAM in sunny days. With ø 12 - 38 cm antenna pair the modulation mode can reach 128-QAM. A peak 5 Gbps link throughput can be achieved in 99.97 % of the time. But even small rain intensities reduce the capacity of the link. Table 3 summarizes main time % figures in Available (A) and Unavailable (U) minutes. Recommended design targets are around the green shadowed rows.

Table 3: Availability and unavailability parameters and their values in minutes in a year.

time of the year, A [%]	time of the year, U [%]	A [minutes]	U [minutes]
99.999 %	0.001 %	525 594.7	5.3
99.995 %	0.005 %	525 573.7	26.3
99.99 %	0.01 %	525 547.4	52.6
99.98 %	0.02 %	525 494.9	105.1
99.965 %	0.035 %	525 416.0	184.0

5.2 Link availabilities in the K rain-zone

In this part the calculation results are shown for estimated *E*-band link availabilities as a function of link length. Curves of Figure 11, 12 and 13 help the design considerations when new links are planned. Naturally, calculations are usually confirmed in a link planning tool. Professional planning tools help in proper channel selection, to minimize interference from neighboring links [19], [37]. Tools also support high/low coordination to avoid near-field interference. As a general design rule, high/low conflict is to be avoided. If by mistake, different sub-band radios are planned on the

same site, the planning tool provides "high/low conflict" warning.

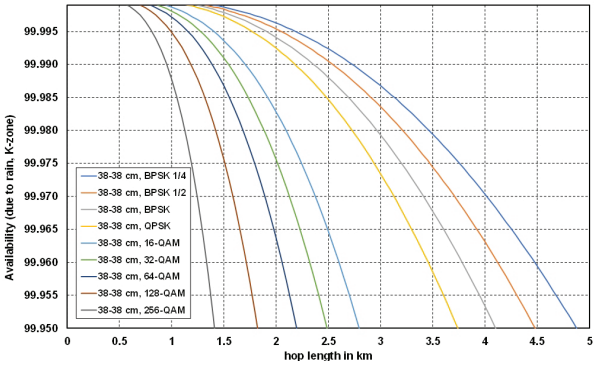

Figure 11: Link Availability as a function of hop length with ø 38 cm – ø 38 cm dish pair. The parameter is the modulation mode from BPSK ¼ to 256-QAM

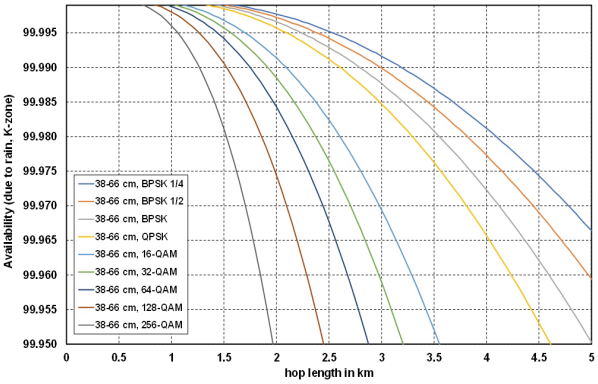

Figure 12: Link Availability as a function of hop length with ø 38 cm – ø 66 cm dish pair. The parameter is the modulation mode from BPSK ¼ to 256-QAM

6 Discussion

After reviewing the main μW/mmW link design steps, set of plots have been calculated numerically. It was shown that modulation mode dependent Fade Margin calculation is straightforward if a radio family is selected with known radio and antenna parameters. On the other hand, to calculate the effect of rain on link availability is difficult. Instead of tedious mathematical solution, a program was used to draw the plots given in part 5. Using the presented method, radio-link under-dimensioning can be avoided.

'Under dimensioned' links have small antennas for the given hop length. Even in sunny days, these links cannot reach the highest radio throughput, as adaptive modulation will not allow to reside on the corresponding modulation mode. In rainy days, under-dimensioned links reduce their symbol rate and the link throughput is quickly degrading [21]-[22]. It is worth mentioning, that for several radios, the throughput is a software licensed item [38]. There is no need to purchase a capacity what a radio link can never benefit in most of the time.

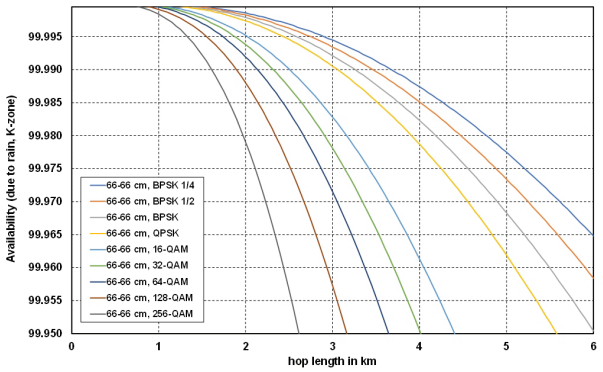

Figure 13: Link Availability as a function of hop length with ø66 cm - ø66 cm dish pair. The parameter is the modulation mode from BPSK ¼ to 256-QAM

On the contrary, 'over dimensioned' links may have too big antenna for the relative short radio hop. Unnecessarily big antennas have unpreferred visual impact on a site. Beside the undesired view, there is a dangerous mechanical problem. In wind-stormy days, strong wind may result vibration or rotation of the dishes if antenna construction is not enforced. The bigger the dish diameter, the stronger pole and antenna construction are required. At 80 GHz the antenna beamwidth is very narrow. The radiated power is focused into a sharp 'pencil' beam [17], [18]. One or even half degree of dish rotation may reduce the antenna gain easily by 3 dB [23], [24]. As presented in the calculation examples, for short hops reaching a nearby fiber access point, mainly ø 12 cm, 38 cm or 66 cm dishes are preferred.

7 Conclusions

E-band radios are excellent extensions of fiber-optical access networks. It was shown in the paper, that thanks to the wide radio bandwidth available by the frequency allocation plan [36], Gbps throughput can be achieved by state-of-the-art mmW radios. Main factor deteriorating the link availability is rain fading. The investigation focused on Central European countries like Slovenia and Hungary, where the *K* rain-zone of ITU-R with 42 mm/h rainfall rate is a good estimation in 0.01 % of the time. It was shown that with proper link design 99.99 % link availabilities or better can be achieved. Practical charts have been plotted to support the design phase of such links. As reviewed in the paper, the optical fiber is get-

ting closer and closer to the end-users in combined fiber/wireless systems (FTTH, FTTO, FTTS, 5G) [1]-[5], [7]-[8], [10]-[16], [39]-[41]. Therefore, the expected lifetime of the discussed *E*-band radio-links is 3-5 years. The investment however is not lost when optical fiber reaches a radio node. The same radio link can be quickly re-used to provide bandwidth for another hop, which is still waiting for the fiber connection.

8 Acknowledgments

The author thanks Dr. Gábor Járó and László Cserháti, (Nokia) for the useful discussions. Tamás Ludányi's (Vodafone) great experience and contribution is greatly acknowledged. The valuable support of Henrik Kiss and Brian Eichenser (CommScope) is appreciated. The author used ComSearch IQ-Link planning tool in several rollout and mobile network modernization projects.

9 Conflict of interest

The author declares no conflict of interest. This research received no external funding.

10 References

1. M. A. Ilgaz, B. Batagelj, "Določanje pomena in kakovosti radijskega dostopovnega omrežja s centraliziranim optoelektronskim oscilatorjem / Determining the importance and quality of a radio access network with a centralized optoelectronic oscillator," (in Slovenian) *Elektrotehniski Vestnik*, vol. 88, no. 4, pp. 183-189, 2021.
2. M. A. Ilgaz, "Opto-Electronic Oscillator in Radio Access Network / Optoelektronski oscilator v radijskem dostopovnem omrežju," *doctoral dissertation,* University of Ljubljana, Slovenia, 2020. [Online]. Available: https://repozitorij.uni-lj. si/IzpisGradiva.php?id=132776. [Accessed: 09-Dec-2021].
3. T. Cseh, "Improvements in Radio over Multimode Fiber Systems by Mode Filtering Techniques," *doctoral dissertation,* Budapest University of Technology and Economics, Hungary, 2018. http://hdl.handle.net/10890/5652
4. A. Hilt, E. Udvary, G. Járó, T. Berceli, "Harmonic Components and Dispersion of Mobile Network Signals due to Fiber-Optical Transmission," in *21st Optical Network Design and Modelling Conference Proceedings*, Budapest, Hungary, 2017, pp. 1-7, https://doi.org/10.23919/ONDM.2017.7958543.
5. M. A. Ilgaz, B. Batagelj, "Proposal for Distribution of a Low-Phase-Noise Oscillator Signal in Forthcoming Fifth-Generation Mobile Network by Radio-Over-Fibre Technology," in *58th International Symposium Electronics in Marine Conference Proceedings*, 2016, pp. 13-16, https://doi. org/10.1109/ELMAR. 2016.7731744.
6. J. Ladvánszky, "Circuit Theoretical Aspects of Optical Communication Links," in *17th International Conference on Transparent Optical Networks Conference Proceedings*, pp. 1-4, 2015, https://doi. org/10.1109/ICTON.2015.7193443.
7. B. Batagelj, L. Pavlovič, L. Naglič, S. Tomažič, "Convergence of fixed and mobile networks by radio over fibre technology," *Informacije MIDEM,* vol. 41, no. 2, pp. 144–149, 2011, http://www. midem-drustvo.si/Journal%20papers/MIDEM_41(2011)2p144.pdf.
8. T. Marozsák et al., "A new optical distribution approach for millimeter wave radio," in *IEEE MTT Topical Meeting on Microwave Photonics Conference Proceedings,* 1998, pp. 63-66, https://doi.org/10.1109/MWP.1998.745501.
9. G. Járó, "High speed optical receivers (in Hungarian: Nagysebességű optikai vevők)," *doctoral dissertation*, BME, Technical University of Budapest, Budapest, Hungary, 1999.
10. A. Hilt, "Transmission et traitement optiques des signaux dans les systèmes de télécommunications hertziens," *doctoral dissertation,* INPG, Institut National Polytechnique de Grenoble, Grenoble, France, 1999.
11. A. Hilt, T. Marozsák, G. Maury, T. Berceli, B. Cabon, A. Vilcot, "Radio-node upconversion in millimeter-wave fiber-radio distribution systems," in *12th International Conference on Microwaves & Radar Conference Proceedings*, vol. 1, pp. 176-180, 1998, https://doi.org/10.1109/MIKON.1998.737942
12. B. Batagelj, "Deployment of Fiber-to-the-Home in the Slovenian Telecommunications Market," *Fiber and Integrated Optics*, 2013, vol. 32, no. 1, pp. 1-11, https://doi.org/10.1080/01468030.2012.760686.
13. A. Hilt, L. Pozsonyi, "Application of Fiber-Optical Techniques in the Access Transmission and Backbone Transport of Mobile Networks," *Fiber and Integrated Optics*, vol. 31, pp. 277-298, 2012, https://doi.org/10.1080/01468030.2012.723797.
14. A. K. Garg, V. Janyani, B. Batagelj, N. H. Z. Abidin, M. H. A. Bakar, "Hybrid FSO/fiber optic link based reliable & energy efficient WDM optical network architecture," *Optical Fiber Technology*, vol. 61, pp. 1-10, 102422, 2021, ISSN 1068-5200, https://doi. org/10.1016/j.yofte.2020.102422.
15. L. Giorgi et al., "Subcarrier Multiplexing RF Plans for Analog Radio Over Fiber in Heterogeneous

Networks," *Journal of Lightwave Technology*, vol. 34, no. 16, pp. 3859-3866, 2016, https://doi.org/10.1109/JLT.2016.2581883.
16. J. Varga et al., "Reducing operational costs of ultra-reliable low latency services in 5G," *Infocommunications Journal*, vol. 10, no. 4, pp. 37-45, 2018, https://doi.org/10.36244/ICJ.2018.4.6.
17. P. Angueira, J. A. Romo, *Microwave Line of Sight Link Engineering*, John Wiley & Sons, USA, 2012.
18. T. Manning, *Microwave Radio Handy Reference Guide*, 1st ed., TMC Global, ISBN:9780648191568, Brisbane, Australia, 2019.
19. ComSearch, a Commscope Company, "IQ-Link, Microwave Link Design System," *User Guide,* version 10.4.0.7, 2021.
20. Nokia, "Nokia Wavence Ultra-Broadband Transceiver Millimeterwave 80," *Nokia data sheet*, 2021, [Online]. Available: https://www.nokia.com/networks/products/e-band-portfolio/ [Accessed: 12-Dec-2021]
21. A. Al-Saman, M. Mohamed, M. Cheffena, M. H. Azmi, T. A. Rahman, "Performance of Full-Duplex Wireless Back-Haul Link under Rain Effects Using E-Band 73 GHz and 83 GHz in Tropical Area," *MDPI Applied Sciences*, vol. 10, no. 17, 6138, pp. 1-9, https://doi.org/10.3390/app10176138.
22. A. Hilt, "Microwave Hop-Length and Availability Targets for the 5G Mobile Backhaul," in *42nd IEEE Telecommunications and Signal Processing Conference Proceedings*, 2019, pp. 187-190, https://doi.org/10.1109/TSP.2019.8768870.
23. Commscope, "VHLP1-80/A, 0.3 m / 1 ft ValuLine® High Performance Low Profile Antenna, single-polarized, 71.000 – 86.000 GHz," *antenna data sheet,* CommScope Inc., 2020.
24. Commscope, "VHLP2-80/B, 0.6m / 2 ft ValuLine® High Performance Antenna, single polarized, 71.000–86.000 GHz," *antenna data sheet,* CommScope Inc., 2021.
25. Rec. ITU-R P.676-12, "Attenuation by atmospheric gases and related effects," in *P Series, Radiowave Propagation*, *International Telecommunication Union,* Geneva, Switzerland, 2019.
26. V. Kvičera, M. Grabner, "Rain attenuation at 58 GHz: Prediction versus long-term trial results," *EURASIP Journal of Wireless Communications and Networking*, vol. 2007, pp. 1–7, https://doi.org/10.1155/2007/46083.
27. A. Hilt, T. Pap, "Application of 58 GHz band for GSM access networks in Hungary," in *11th Microwave Colloquium Conference Proceedings,* 2003, pp. 81–84, Budapest, Hungary, https://hdl.handle.net/10890/16318.
28. Rec. ITU-R P.838-3, "Specific attenuation model for rain for use in prediction methods," in *P Series, Radiowave Propagation*, *International Telecommunication Union,* Geneva, Switzerland, 2005.
29. Nokia, "The evolution of microwave transport - enabling 5G and beyond," *Nokia White Paper,* Espoo, Finland, 2019.
30. L. Csurgai-Horváth, I. Frigyes, J. Bitó, "Propagation and Availability on E-band Terrestrial Radio," in *6th European Conference on Antennas and Propagation Conference Proceedings*, pp. 73-75, 2012, https://doi.org/10.1109/EuCAP.2012.6206539.
31. Rec. ITU-R P.530-13, -18, "Propagation data and prediction methods required for the design of terrestrial line-of-sight systems," in *P Series, Radiowave propagation, International Telecommunication Union,* Geneva, Switzerland, 2009, 2021.
32. Rec. ITU-R P.837-1, -7, "Characteristics of precipitation for propagation modelling," in *P Series, Radiowave propagation, International Telecommunication Union,* Geneva, Switzerland, 1994, 2017.
33. M. Lakatos, L. Hoffmann, "Rendkívüli csapadékhullás Budapest belvárosában (in Hungarian) / Extraordinary Rainfall in Downtown Budapest," *OMSZ, Országos Meteorológiai Szolgálat,* 2017, [Online]. Available: https://www.met.hu/ismeret-tar/erdekessegek_tanulmanyok/index.php?id=1885. [Accessed: 09-Dec-2021].
34. M. Lakatos, L. Hoffmann, "Increasing trend in short term precipitation and higher return levels due to climate change," in *Országos Települési Csapadékvíz-gazdálkodási Konferencia* (in Hungarian), Cum Scientia pro Aquis Hungariae, 2017, pp. 8-16, ISBN 978-615-5845-21-5.
35. B. Adjei-Frimpong, L. Csurgai-Horváth, "Using Radio Wave Satellite Propagation Measurements for Rain Intensity Estimation," *Infocommunications Journal*, vol. 10, no. 3, pp. 2-8, 2018, https://doi.org/10.36244/ICJ.2018.3.1.
36. CEPT ECC Rec. (05)07, "Radio Frequency Channel Arrangements for Fixed Service Systems Operating in the Bands 71-76 GHz and 81-86 GHz," 2013. [Online]. Available: https://docdb.cept.org/download/9c4f8690-d0e1/REC0507.PDF. [Accessed: 09-Dec-2021].
37. A. Hilt, T. Pap, "Fixed MW Access Network Design Using Interference Matrices," in *11th Microwave Colloquium Conference Proceedings,* 2003, pp. 169–172, Budapest, Hungary, http://hdl.handle.net/ 10890/16608.
38. A. Hilt, G. Járó, "Licensing options for virtual network functions in telecommunications cloud environment," in *11th IEEE/IET International Symposium on Communication Systems, Networks & Digital Signal Processing Conference Proceedings*, 2018, pp. 1-6, https://doi.org/10.1109/CSNDSP.2018.8471802.

39. N. Badraoui, "Investigations on optical communication links for high data rate in 5G systems," *doctoral dissertation*, BME, Budapest University of Technology and Economics, Budapest, Hungary, 2020. http://hdl.handle.net/10890/15127.
40. J. Ratkoceri, "Capacity Increase of an Optical Access Network Using an Injection-locked Fabry-Perot Laser," *doctoral dissertation,* University of Ljubljana, Slovenia, 2019.
41. H. N. Parajuli, "Investigation of Potential 5G Modulation Formats in mm-Wave Radio Over Fiber Systems and Passive Optical Network," *doctoral dissertation*, BME, Budapest University of Technology and Economics, Budapest, Hungary, 2018. http://hdl.handle.net/10890/5661.

Arrived: 14. 12. 2021
Accepted: 28. 01. 2022

Original scientific paper
https://doi.org/10.33180/InfMIDEM2022.105

Informacije MIDEM
Journal of Microelectronics, Electronic Components and Materials
Vol. 52, No. 1(2022), 41 – 49

Charge Pump Using Gain-Boosting and Positive Feedback Techniques in 180-nm Digital CMOS Process

Fatemeh Esmailisaraji, Alireza Ghorbani, Seyed Mahmoud Anisheh

Department of Electrical Engineering, Sari Branch, Islamic Azad University, Sari, Iran

Abstract: The charge pump (CP) circuit is an essential element in a delay-locked loop (DLL). This paper proposes a new CP using gain-boosting technique. Two possible solutions for gain-boosting circuit implementation are presented. One solution is based on common-source amplifier. In another solution, positive feedback method is employed at the output stage to increase the output resistance of the amplifier. Therefore, DC-gain of the amplifier is improved. In addition, nonlinear current mirror is employed in which the gain is dependent to the input current. To evaluate the performance of the proposed CPs, simulations are done in a 0.18 µm CMOS process with the supply voltage of 1.8 V. The simulation results indicate that the proposed CPs can obtain good current matching characteristics in the low power applications. The mismatch between up and down CP currents is less than 1%.

Keywords: Charge pump; Common-source amplifier; Gain-boosting; Positive feedback; Nonlinear current mirror

Črpalka naboja z uporabo tehnik povečanja ojačanja in pozitivne povratne zveze v 180-nm digitalnem procesu CMOS

Izvleček: Vezje črpalke naboja (CP) je bistven element v zanki z zakasnitvijo (DLL). Ta članek predlaga novo CP s tehniko povečanja ojačenja. Predstavljeni sta dve možni rešitvi za izvedbo vezja za povečanje ojačenja. Ena rešitev temelji na ojačevalniku skupnega vira. Pri drugi rešitvi je na izhodni stopnji uporabljena metoda pozitivne povratne zveze za povečanje izhodne upornosti ojačevalnika. Zato se izboljša enosmerno ojačanje ojačevalnika. Poleg tega je uporabljeno nelinearno tokovno zrcalo, pri katerem je ojačenje odvisno od vhodnega toka. Da bi ocenili delovanje predlaganih ojačevalnikov, so simulacije izvedene v 0,18 µm procesu CMOS z napajalno napetostjo 1,8 V. Rezultati simulacij kažejo, da lahko predlagani ojačevalniki dosežejo dobre karakteristike tokovnega ujemanja v nizkoenergijskih aplikacijah. Neskladje med tokovi CP navzgor in navzdol je manjše od 1 %.

Ključne besede: črpalka naboja; ojačevalnik s skupnim virom; povečanje ojačenja; pozitivne povratna zanka; nelinearno tokovno ogledalo

** Corresponding Author's e-mail: alirezaghorbani2005@gmail.com*

1 Introduction

Phase-locked loops (PLL) and delay-locked loops (DLL) have been widely employed for clock synchronization applications. Nowadays, the DLL can be used for synchronization, clock generation, and digital transceivers in serial links [1-3]. Several problems should be considered for designing the high-performance DLL. To increase the input frequency range of the DLL, the precision of the phase detector (PD), the matching between the up and down charge pump (CP) currents, and the

How to cite:
F. Esmailisaraji et al., "Charge Pump Using Gain-Boosting and Positive Feedback Techniques in 180-nm Digital CMOS Process", Inf. Midem-J. Microelectron. Electron. Compon. Mater., Vol. 52, No. 1(2022), pp. 41–49

delay cells bandwidth requirement in a voltage-controlled delay line (VCDL) should be regarded [4-5]. By increasing the input frequency, the phase resolution is limited by the phase offset of the PD. The current mismatch between the up and down signal may lead to static phase error between the input and output clocks [6-10]. Increasing the number of the delay cells or the input clock frequency will result in harmonic-locked problem provided that the total intrinsic delay is greater than the period of the input clock.

Several methods for designing CP have been suggested in the literatures [11-19]. A conventional CMOS CP circuit consists of UP and DN switches made by PMOS and NMOS transistors, respectively. This method suffers from current mismatch between Up and Down paths. It is due to the different output impedances of PMOS and NMOS transistors [11]. Some ideas have been suggested to overcome the shortcoming of the basic CP. In [12], it is shown that by employing of dummy devices and dummy loads, current mismatch can be reduced significantly. In another method, cascade topology is utilized to reduce current mismatch and reference spurs [13]. It is indicated that operational amplifiers (op-amps) as a unity gain amplifier can be successful in alleviating the current mismatch [14]. Another design method proposed in [15] reduces the output current glitch by canceling the spurious jump phenomenon.

In [16], the CP circuit performance in terms of current matching is improved by the operational trans-conductance amplifier (OTA). The mismatch between I_{ch} (charge current) and I_{dis} (discharge current) of the CP circuit is reduced significantly. But, current variation is not considered in this method. It is shown that I_{ch} and I_{dis} are dependent on output voltage variation. Therefore, CP-PLLs stability and transient response may be affected [17]. In another method [18], the gain-boosting technique is proposed to increase the output impedance of the CP circuit. In this method, the output current will remain more constant and the result indicates good current matching characteristic. In addition, using the bulk-driven method, the output voltage swing is improved while the power dissipation (Pdiss) is reduced. In [19], the gain-boosting is used to increase the output impedance of the CP as well as a low-voltage cascode current mirror is used to enhance its current matching. The low-voltage cascode current mirror is used to copy I_{ch} and I_{dis} from a single current source to ensure that both current values are equal.

Some techniques have been developed to reduce the power consumption and increase the power efficiency of the CP circuits. In [20], To improve the charge transfer characteristic a feedback loop is utilized. In [21], a CP is introduced based on a four-phase clock and boost capacitors on the switch transistors which eliminates the influence of threshold voltage of the transistor. In [22], an optimized method is suggested that relies on the determination of the optimal stage number to minimize the power consumption. In [23], the charge sharing method is employed for a four-phase charge pump to enhance the power efficiency. The technique in [24], which combines the charge sharing technique with multi-step capacitor charging can alleviate the overall power consumption compared to the conventional four-phase CP and also the charge sharing based CP.

In this paper, a new CP is proposed using the gain-boosting technique. Two circuit implementations of the gain-boosting are presented. One implementation is based on a common-source amplifier, and the other is based on a positive feedback amplifier. In addition, nonlinear current mirror with gain dependent on the input current is utilized for the proposed CP. The results indicate the superiority of the proposed technique in terms of current matching compared to the existing methods. In Section 2, the proposed CP is described. The performance evaluations of the CP and comparison results are provided in Section 3. Finally, Section 4 concludes the paper.

2 Proposed CPs

In this Section, two CPs using the gain-boosting techniques are presented. The designing details are provided as follows.

2.1 Common-source amplifier based CP

Figure 1 shows the circuit configuration of the proposed CP using the gain-boosting technique. In this circuit, M_1 and M_2 are the current sources. Up and Down controlled switches are implemented by M_4 and M_3, respectively. (M_5, $M_{7)}$ and (M_6, M_8) form the gain-boosting loop where M_7 and M_8 works as a common-source amplifier. M_9 to M_{14} are current mirror transistors. M_{15} acts as reference current generator. The output impedance can be described as follows:

$$R_{out} = (g_{m5}r_{o5}g_{m3}r_{o3}r_{o1})(g_{m7}r_{o7}) \parallel (g_{m6}r_{o6}g_{m4}r_{o4}r_{o2})(g_{m8}r_{o8}) \quad (1)$$

In the above equations, g_m and r_o denote the trans-conductance of the transistor and the drain-source resistor of the related transistor, respectively.

Nonlinear current mirrors based on flipped voltage follower (FVF) [25-27] have been used for the output active loads made by transistor sets (M_9, M_{10}, $M_{11)}$ and (M_{12}, M_{13}, M_{14}). The nonlinearity of the current mirrors results in the

desired output current boosting. The current mirrors are used to ensure that I_{UP} and I_{DOWN} currents are equal.

If V_{b1} is chosen to bias M_{10} in the triode region, the following equations are obtained:

$$I_9 = \frac{1}{2}\beta_9 V_{od9}^2 \tag{2}$$

$$I_{10} = \beta_{10} V_{od10} V_{DS10} \tag{3}$$

where $\beta=\mu_n C_{ox} W/L$ and V_{od} represents the overdrive voltage of the transistor. It should be mentioned that μ_n, C_{ox}, W and L are electron mobility, gate-channel capacitance density, transistor channel width, and transistor channel length, respectively. Assuming $\beta_9=\beta_{10}$ and using equations (2) and (3), we have:

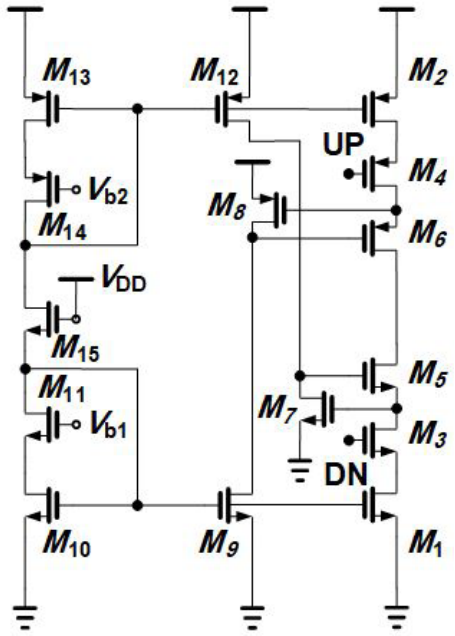

Figure 1: The first proposed CP.

$$I_9 = \frac{I_{10}^2}{2\beta_9 V_{DS10}^2} \tag{4}$$

Since $V_{DS10}=V_{b1}-V_{tn}-V_{od11}$ (V_{tn} is the threshold voltage), I_9 is given as below:

$$I_9 = \frac{I_{10}^2}{2\beta_9 (V_{b1} - V_{tn} - \sqrt{\frac{2I_{10}}{\beta_{11}}})^2} \tag{5}$$

As can be seen from (5), a nonlinear relation exists between I_9 and I_{10}. It is worth to mention that biasing M_{10} in the saturation region leads to the obtaining conventional linear current mirror.

2.2 Positive feedback based CP

The OTAs are used in many applications such as high-resolution ADCs and DACs, and sample-and-hold amplifiers (SHAs) [25-30]. Figure 2 shows another possible solution for the CP in which the gain-boosting circuit implementation is performed by the OTA. The proposed OTA to provide higher DC-gain compared to the common-source amplifier is shown in Figure 3.

In the proposed OTA, the transistors (M_{1a}, M_{1b}, M_{2a}, M_{2b}, M_{3a}, M_{3b}) constitute a flipped voltage follower (FVF) [25-27] to bias the input differential pairs. Input signals are applied to the split transistor sets (M_{4a}, M_{4b}) and (M_{4c}, M_{4d}) which have the same aspect ratio. Consider a situation in which V_{in+} and V_{in-} increases and decreases, respectively. Thus, the source-gate voltages of the (M_{4a}, M_{4b}) and (M_{4c}, M_{4d}) decrease and increase, respectively.

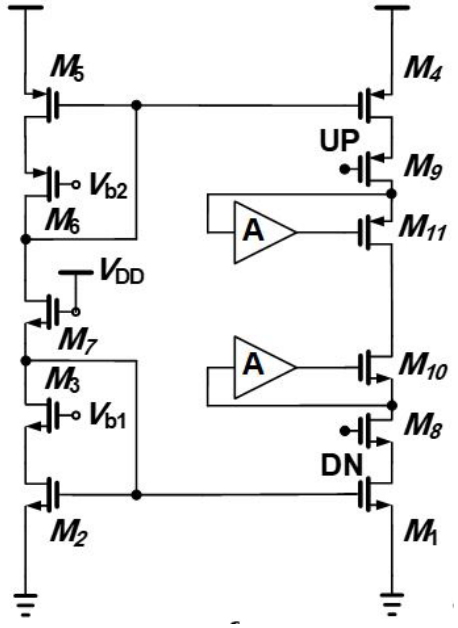

Figure 2: The second proposed CP.

Therefore, the current through them decrease and increase, respectively. M_5 and M_6 are used as common-gate transistors. M_7 to M_{10} are active load transistors of the common-gate transistors. M_{11} to M_{14} act as improved recycling structure (IRS) [30]. The IRS technique presents different paths for DC and AC currents, which results in enhancing the trans-conductance. By applying the output signal V_{out+} to the bulk terminal of M_5 and V_{out-} to the bulk terminal of M_6, a positive feedback loop is created. In order to control the gain of the feedback loop and also avoiding instability, the resistors (R_1, $R_{2)}$ and (R_3, R_4) are used. The resistor sets work as the voltage divider. The division factor is defined as below:

$$k = \frac{R_2}{R_1 + R_2} \tag{6}$$

The DC-gain of the OTA is explained as:

$$A_d = G_{meff\,1} R_{out} \tag{7}$$

The G_{meff1} is calculated in [25] as below:

$$G_{meff\,1} = g_{m\,4a}(1+\alpha_1) + g_{m\,9} \tag{8}$$

where $\alpha_1 = g_{m13a}/g_{m13b}$ means that M_{13a} aspect ratio is α_1 times greater than that of M13b.

In order to derive the output resistance of the OTA, the equivalent resistance from the drain of M_5 should be determined (see Figure 4).

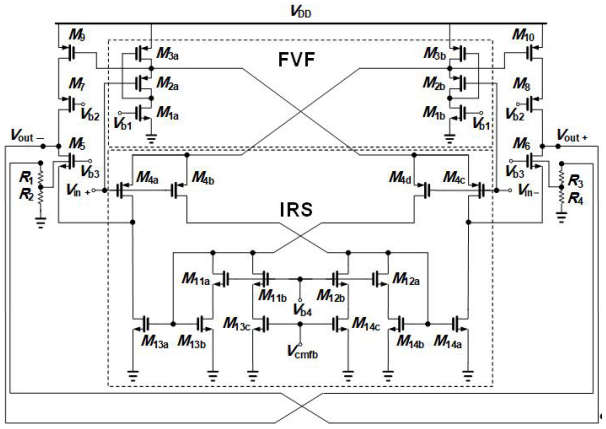

Figure 3: The proposed OTA.

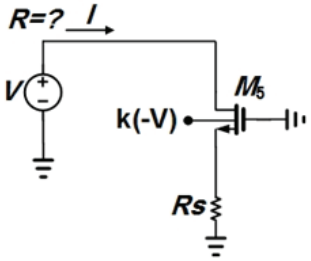

Figure 4: Model to calculate the equivalent resistance from the drain. of M_5.

$$R = \frac{V}{I} = \frac{r_{o5} + g_{m5} r_{o5} R_s + R_s}{1 - g_{mb5} k r_{o5}} \tag{9}$$

Therefore, the R_{out} is defined as follows:

$$\begin{aligned} R_{out} &= [g_{m7} r_{o7} r_{o9} \,\|\, \mathrm{R}] \\ &= [g_{m7} r_{o7} r_{o9} \,\|\, \frac{r_{o5} + g_{m5} r_{o5} R_s + R_s}{1 - g_{mb5} k r_{o5}}] \end{aligned} \tag{10}$$

In the above equations, R_{out} is the output resistance of the OTA and $R_s = r_{o4a} \| r_{o13a}$. Moreover, g_{mb5} denotes the trans-conductance of the bulk-driven transistor M_5 that represents the body effect. Using the positive feedback, the output resistance can be increased. If the denominator of equation (9) is chosen so that $1\text{-}g_{mb5}k\text{-}r_{o5}>0$, close to zero, then the differential voltage gain is enhanced significantly, and the circuit is stable.

It is worth to mention that the dominant pole is determined by the output resistance and capacitive load as follows:

$$\omega_{p1} = \frac{1}{R_{out} C_L} \tag{11}$$

Equation (11) reveals that the positive feedback technique moves the dominant pole to the lower frequency.

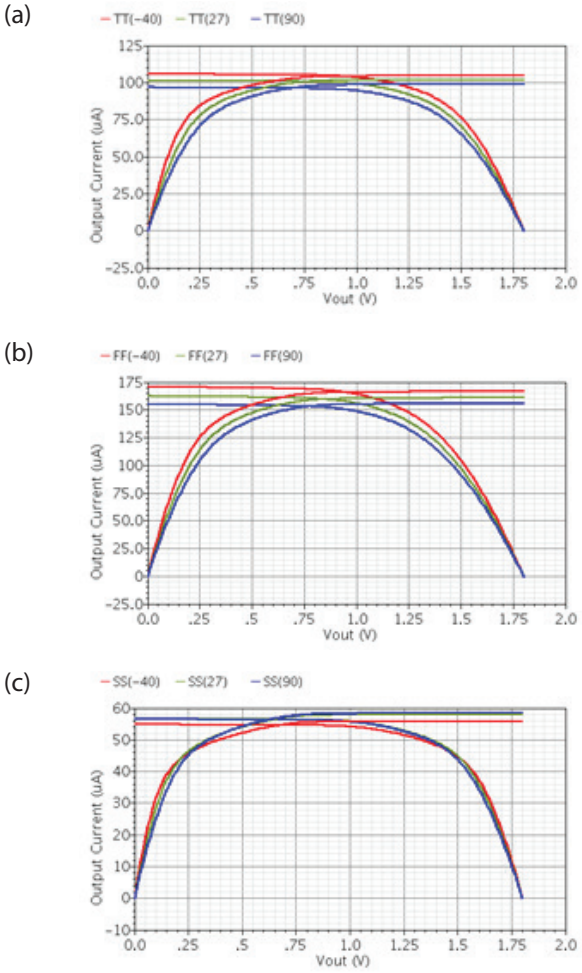

Figure 5: Charge and discharge current output versus the output voltage of the first proposed CP in the process and temperature corners: (a) TT(-40°C), TT(27°C), TT(90°C), (b) FF(-40°C), FF(27°C), FF(90°C), (c) SS(-40°C), SS(27°C), SS(90°C).

3 Simulation Results

In order to verify the performance of the proposed CPs, some simulations are performed. Both of the CPs are designed in a 0.18 µm CMOS process with 1.8V supply voltage using Cadence software. Figure 5 shows the charge and discharge current output versus the output voltage of the first proposed CP circuit in process and temperature corners. The CP current is about 100 µA, and the mismatch between I_{UP} and I_{DOWN} is less than 1% over the output voltage dynamic range from 0.2V to 1.79V, which covers 88% of the 1.8V supply voltage. Layout of the first proposed CP is shown in Figure 6 in which the layout area is 12µm×18µm.

The Bode diagrams of the proposed OTA using the positive feedback technique are shown in Figure 7. As can be seen from the Figure 7, the proposed OTA exhibits 79 dB DC-gain. UGBW and phase margin of the proposed OTA are 160 MHz and 75^0, respectively. The phase margin shows that the OTA is stable. In order to the slew rate (SR) calculation, a square wave, 1 Vpp at 5 MHz was applied to the OTA, and the result is shown in Figure 8. The OTA specifications along with a comparison to the existing methods are summarized in Table 1. As seen from the results, the proposed OTA has the highest DC-gain, at least 9 dB more than the other methods. In addition, the proposed OTA has high values for both figure of merits (FOMs).

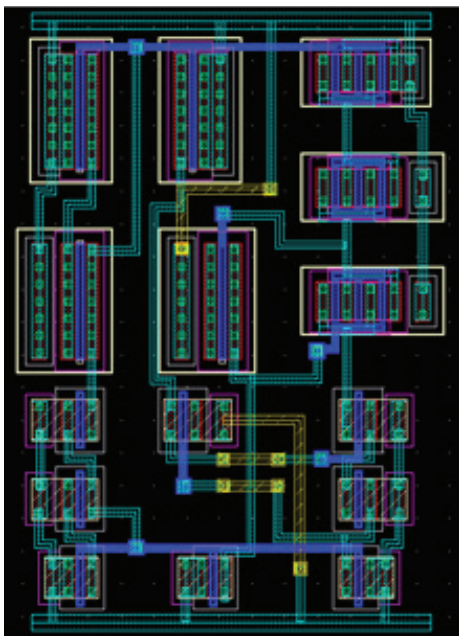

Figure 6: Layout of the first proposed CP.

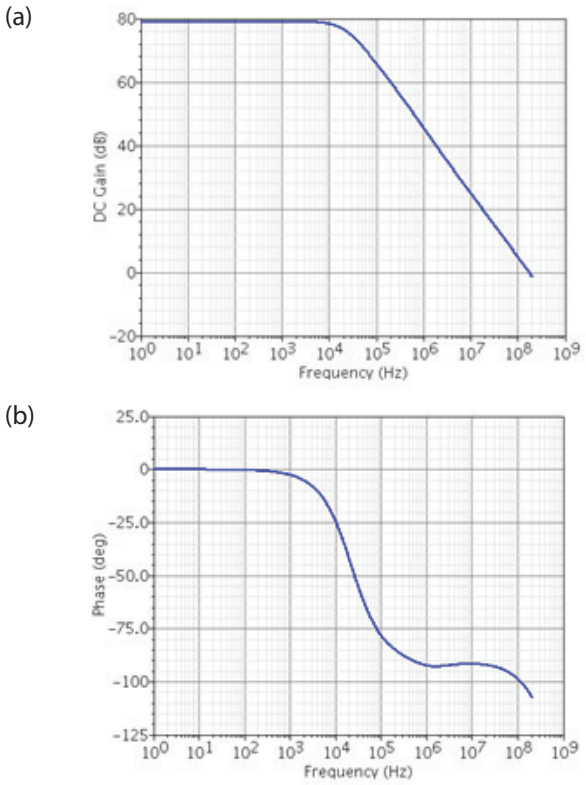

Figure 7: Frequency responses of the proposed OTA: (a) magnitude and (b) phase.

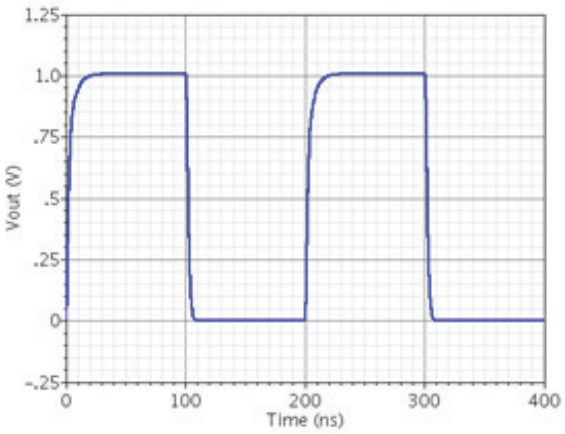

Figure 8: OTA large signal step response.

Table 1: Performance Comparison of the Proposed OTA and the Existing Methods.

Parameter	[28]	[29]	[30]	This work
Bias current	260µA	260µA	260µA	260µA
CL(pF)	7	7	7	7
UGBW(MHZ)	24.6	50	83	160
Gain(dB)	56	65	70	79
Phase margin (deg)	87	80	70	75

SR (V/µs)	12	23	38	47
$FOM_S = \frac{MHz.pF}{mA}$	662	1346	2235	4308
$FOM_L = \frac{V.pF}{ì\ s.mA}$	323	619	1023	1265

Monte Carlo (MC) simulations for the proposed OTA are done by considering both process and mismatch variations. Figure 9 indicates the MC histograms of the proposed OTA using 100-run simulations. From the Figure 9, the mean and standard deviation values for the DC-gain are 76.5 and 4.6, respectively. For the phase margin, the mean and standard deviation values are 75.1 and 1.8, respectively. The layout of the OTA is depicted in Figure 10. The area of the layout is 35µm×86µm.

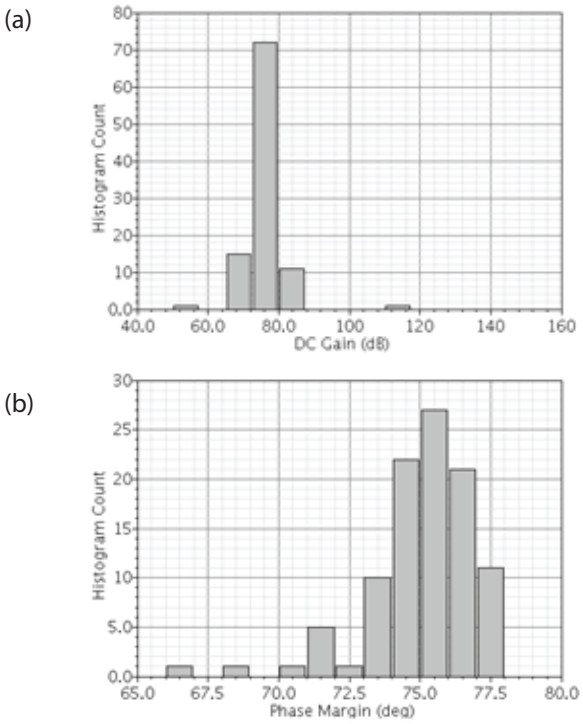

Figure 9: Histogram of MC simulation for the proposed OTA. (a) DC Gain, (b) Phase Margin.

Figure 11 shows the charge and discharge current output versus the output voltage of the second solution for the CP in the process and temperature corners. The current boosting factor of the nonlinear current mirror

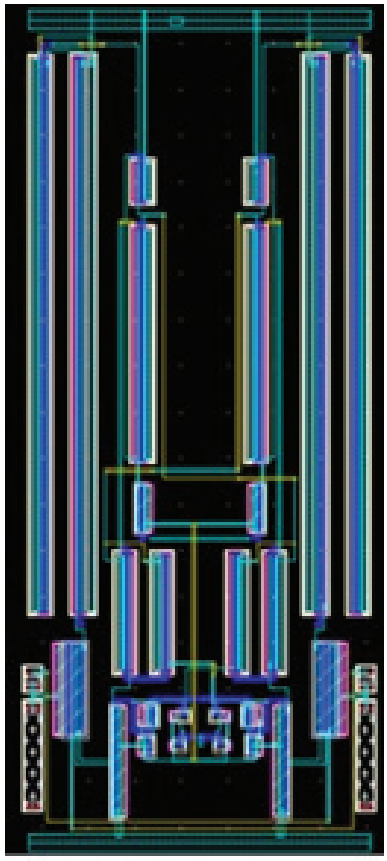

Figure 10: The layout of the OTA.

is equal to 1.5. The CP current is about 100 µA, and the mismatch between I_{UP} and I_{DOWN} is less than 0.3% over the output voltage dynamic range from 0.2V to 1.79V, which covers 88% of the 1.8V supply voltage. It has the less current mismatch compared to the first solution.

Table 2 presents the post-layout comparison parameters among the proposed CPs and other existing CP circuits. The second CP has the lowest current mismatch while it has the higher power dissipation due to using the gain-boosting OTA (1.2 mW in the CP2 compared to the 0.6 mW in the CP1). In addition, the CPs have the wide range for the output voltage. In conclusion, the proposed CPs achieve the best trade-off.

Table 2. Comparison parameters of the proposed CPs and other existing CP circuits.

	CP1	CP2	[6]	[7]	[8]	[9]	[10]
Technology	0.18µm	0.18µm	0.18µm	0.13µm	0.18µm	0.18µm	0.18µm
Supply Voltage (V)	1.8	1.8	1.2	1.2	1.8	1.8	1.8
Current Mismatch	1%	0.3%	0.5%	3.2%	0.5%	1%	0.5%
Output Voltage Range	88%	88%	83%	67%	83%	70%	83%

(a)

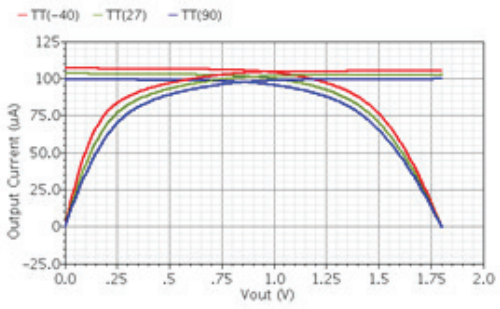

(b)

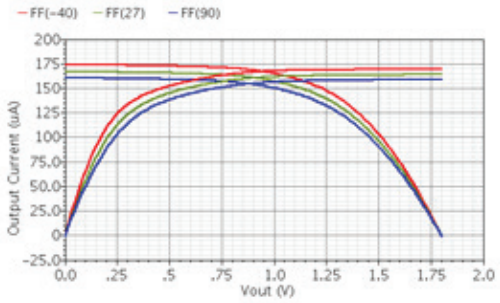

(c)

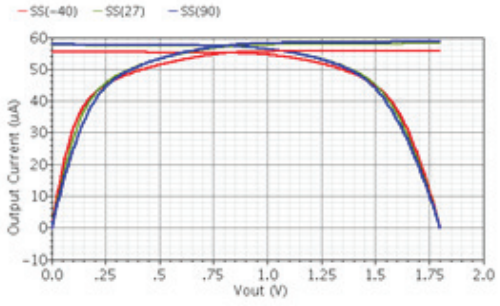

Figure 11. Charge and discharge current output versus the output voltage of the second proposed CP in the process and temperature corners: (a) TT(-40^{0}C), TT(27^{0}C), TT(90^{0}C), (b) FF(-40^{0}C), FF(27^{0}C), FF(90^{0}C), (c) SS(-40^{0}C), SS(27^{0}C), SS(90^{0}C).

4 Conclusions

In this paper, new charge pumps in a 0.18 µm CMOS process with a 1.8 V supply voltage have been presented. The charge pumps were based on the gain-boosting techniques. Common-source amplifier and positive feedback-based OTA were suggested to implement gain-boosting techniques. Nonlinear current mirrors have been employed to generate desired current boosting. The power dissipation of the CP1 and CP2 were 0.6 mW and 1.2 mW, respectively. In order to evaluate the effectiveness of the CPs, several simulation scenarios have been done in the process and temperature corners. The results indicated the superiority of the proposed CPs in terms of current matching characteristics. The mismatch between I_{UP} and I_{DOWN} of the CP1 and CP2 were less than 1% and 0.3%, respectively.

5 Conflicts of Interest

The authors declare no conflict of interest.

6 References

1. T. I. Badal , P. Maroofee , M. A. S. Bhuiyan , L. F. Rahman , M. B. I. Reaz , M. A. Mukit, "Low power delay locked-loop using 0.13µm CMOS technology,", *International Conference on Advances in Electrical, Electronic and Systems Engineering (ICAEES)*, 2016, pp. 176-179. https://doi.org/10.1109/ICAEES.2016.7888033
2. Chi-Nan Chuang, Shen-Iuan Liu, "A 0.5–5-GHz Wide-Range Multiphase DLL With a Calibrated Charge Pump,", IEEE Transactions on Circuits and Systems II: Express Briefs, Vol. 54, Issue: 11, pp. 939 – 943, 2007. https://doi.org/10.1109/TCSII.2007.904155
3. Muhammad Abrar Akram, Myeong-Ho Lee, Dong-Hyeok Cho, In-Chul Hwang,"A 0.012mm^2, 0.96-mW All-Digital Multiplying Delay-Locked Loop Based Frequency Synthesizer for GPS-L4 band,", IEEE International Conference on Consumer Electronics (ICCE), 2020, pp. 1-2. https://doi.org/10.1109/ICCE46568.2020.9043028
4. Sami Ur Rehman, Mohammad Mahdi Khafaji, Ali Ferschischi; Corrado Carta, Frank Ellinger, "A 0.2-1.3 ns Range Delay-Control Scheme for a 25 Gb/s Data-Receiver Using a Replica Delay-Line-Based Delay-Locked-Loop in 45-nm CMOS,", IEEE Transactions on Circuits and Systems II: Express Briefs, Vol. 67, Issue: 5, pp. 806 – 810, 2020. https://doi.org/10.1109/TCSII.2020.2980813
5. Myeongjo Jeong, Minchul Shin, Jinwoo Kim; Manho Seung, Seokkiu Lee, Jingook Kim, "Measurement and Analysis of System-Level ESD-Induced Jitter in a Delay-Locked Loop,", IEEE Transactions on Electromagnetic Compatibility, Vol. 62, Issue: 5, pp. 1840 – 1851, 2020. https://doi.org/10.1109/TEMC.2019.2936826
6. Yuan Sun, Liter Siek, Pengyu Song, "Design of a High Performance Charge Pump Circuit for Low Voltage Phase-locked Loops,", IEEE ISle. Singapore, 2007, pp. 271-274. https://doi.org/10.1109/ISICIR.2007.4441850
7. Hwang M S, Kim J, Jeong D K, "Reduction of pump current mismatch in charge-pump PLL,", Electronics Letters. vol. 45, 2009, pp. 135-136. https://doi.org/10.1049/el:20092727
8. Shuangshuang Zheng, Zhiqun Li, "A novel COMS Charge Pump with high performance for phase-

locked loops synthesizer,", IEEE ICCT. Jinan, 2011, pp. 1062-1065.
https://doi.org/10.1109/ICCT.2011.6158043
9. Ngo Trong Hieu, Tae-Woo Lee, Hyo-Hoon Park, "A perfectly Current Matched Charge Pump of CP-PLL for Chip-to-Chip Optical Link,", CLEO. Seoul, 2007, pp. 1-2.
https://doi.org/10.1109/CLEOPR.2007.4391088
10. Jia Yaoyao, Fang Jian, Qiao Ming, Zhou Ze-kun, Yang Wentao, Zhang Bo, "A charge pump with reduced current variation and mismatch in low-voltage low-power PLLs,", IEEE International Conference of Electron Devices and Solid-state Circuits, 2013, pp. 1-2.
https://doi.org/10.1109/EDSSC.2013.6628140
11. Kashyap K. Patel, Nilesh D. Patel and Kruti P. Thakore, "Charge Pump, Loop Filter and VCO for Phase Lock Loop Using 0.18 um CMOS Technology", IOSR Journal of VLSI and Signal Processing (IOSR-JVSP) Vol. 2, Issue 4, pp. 21-25, 2013.
https://doi.org/10.9790/4200-0242125
12. J. Keller "SB-1250: A high performance power efficient chip multiprocessor (CMP) targeting networking applications" Microprocessor Forum 2000.
13. C.M. Hung, K.O. Kenneth, "A Fully Integrated 1.5 V 5.5 GHz CMOS Phase Locked Loop", IEEE Journal Of Solid State Circuits, Vol. 37, pp. 521-525, April 2002.
https://doi.org/10.1109/4.991390
14. J. Alvarez, H. Sanchez, G. Gerosa, R. Countryman, "A wide-bandwidth low voltage PLL for PowerPC™ microprocessors", IEEE J. Solid-State Circuits, vol. 30, pp. 383-391, Apr. 1995.
https://doi.org/10.1109/VLSIC.1994.586200
15. R. A. Baki and M. N. El-Gamal, "A new CMOS charge pump for low voltage (1V) high speed PLL Applications" Circuits and Systems, 2003. ISCAS '03. Proceedings of the 2003 International Symposium, Vol. 1, pp. 657-660, 2003.
https://doi.org/10.1109/ISCAS.2003.1205649
16. Jae-Shin Lee, Min-Sun Keel, Shin-Il Lim, et al. "Charge pump with perfect current matching characteristics in phase-locked loops," Electronics Letters. vol. 36, pp. 1907-1908,2000.
https://doi.org/10.1049/el:20001358
17. Soleiman E, Kamarei M, "New low current mismatch and wide output dynamic range charge pump," IEEE ICEE. Tehran, Iran, 2011, pp. 1-5.
18. Noushin Ghaderi, Ali Dehghani, "A novel high swing, low power charge pump circuit with excellent current matching", 24th Iranian Conference on Electrical Engineering (ICEE), 2016, pp. 1797-1800.
https://doi.org/10.1109/IranianCEE.2016.7585812
19. Rania H. Mekky, Mohamed Dessouky, "Design of a Low-Mismatch Gain-Boosting Charge Pump for Phase-Locked Loops", International Conference on Microelectronics, 2007, pp. 1-4.
https://doi.org/10.1109/ICM.2007.4497720
20. J. Shin, I.-Y. Chung, Y. J. Park et H. S. Min, "A new charge pump without degradation in threshold voltage due to body effect [memory applications]," IEEE Journal of Solid-State Circuits, vol. 35, no. 18, pp. 1227-1230, August 2000.
https://doi.org/10.1109/4.859515
21. K. H. Choi, J. M. Park, J. K. Kim, T. S. Jung et K. D. Suh, "Floating-well charge-pump circuits for sub-2.0-V single power supply flash memories," chez Symposium VLSI circuits Dig. Tech. Papers, 1997.
https://doi.org/10.1109/VLSIC.1997.623807
22. G. Palumbo, D. Pappalardo et M. Gaibotti, "Charge-Pump Circuits: Power-Consumption Optimization," IEEE Transactions on Circuits and Systems I: Fundamental Theory and applications, vol. 49, no. 111, pp.1535-1542, November 2002.
https://doi.org/10.1109/TCSI.2002.804544
23. C. Lauterbach, W. Weber et D. Romer, "Charge sharing concept and new clocking scheme for power efficiency and electromagnetic emission improvement of boosted charge pumps," IEEE Journal of Solid-State Circuits, vol. 35, pp. 719-723, May 2000.
https://doi.org/10.1109/4.841499
24. S. Ngueya W., J. Mellier, S. Ricard, J. M. Portal et H. Aziza, "Ultra Low Power Charge Pump with Multi-Step Charging and Charge Sharing," chez IEEE 8th International Memory Workshop (IMW), Paris, 2016.
https://doi.org/10.1109/IMW.2016.7495294
25. Behrouj, A.R., Ghorbani, A.R., Ghaznavi-Ghoushchi, M.B. *et al.* A Low-Power CMOS Transceiver in 130 nm for Wireless Sensor Network Applications. *Wireless Pers* Commun, vol 106, pp.1015–1039 (2019).
https://doi.org/10.1007/s11277-019-06201-8
26. S. M. Anisheh, H. Abbasizadeh, H. Shamsi, C. Dadkhah, K. Y. Lee, "A 84 dB DC-Gain Two-Stage Class-AB OTA," IET Circuits Devices & Systems , 2019, pp. 1-10.
https://doi.org/10.1049/iet-cds.2018.5038
27. J. A. Galan, A. J. López-Martín, R. G. Carvajal, J. Ramírez-Angulo, and C. Rubia-Marcos, "Super class-AB OTAs with adaptive biasing and dynamic output current scaling," IEEE Transactions on Circuits and Systems I: Regular Papers, vol. 54, no. 3, pp. 449-457, 2007.
https://doi.org/10.1109/TCSI.2006.887639
28. A.R. Ghorbani, M.B. Ghaznavi-Ghoushchi, "A novel transceiver structure including power and audio

amplifiers for Internet of Things applications" ,Computers & Electrical Engineering, Volume 62,2017,pp 29-43. https://doi.org/10.1016/j.compeleceng.2017.07.025.
29. R. S. Assaad, and J. Silva-Martinez, "The Recycling Folded Cascode: A General Enhancement of the Folded Cascode Amplifier," IEEE J. Solid-State Circuits, vol. 44, no. 9, pp. 2535-2542, 2009. https://doi.org/10.1109/JSSC.2009.2024819
30. Y.L. Li, K.F. Han, X. Tan, N. Yan and H. Min, "Transconductance enhancement method for operational transconductance amplifiers," Electron. Lett., vol. 46, no. 19, pp. 1321–1323, 2010. https://doi.org/10.1049/el.2010.1575

Arrived: 27. 11. 2021
Accepted: 15. 02. 2022

Original scientific paper
https://doi.org/10.33180/InfMIDEM2022.106

Informacije MIDEM
Journal of Microelectronics,
Electronic Components and Materials
Vol. 52, No. 1(2022), 51 – 66

Improved Current Mode Biquadratic Shadow Universal Filter

Divya Singh, Sajal K. Paul

Department of Electronics Engineering, Indian Institute of Technology (Indian School of Mines), Dhanbad, Jharkhand, India

Abstract: In this paper, an improved single-input-multiple-output (SIMO) current-mode biquadratic shadow universal filter (SUF) is realized using two new variants of second-generation current conveyors (CCIIs), namely current conveyor cascaded transconductance amplifier (CCCTA) and extra-X current controlled conveyor transconductance amplifier (EX-CCCTA). The low pass and the band pass outputs of a non-shadow universal filter (NSUF), consisting of CCCTA, are utilized through two amplifiers' feedback paths using one EX-CCCTA to realize the proposed SUF. It is resistorless and utilizes only two grounded capacitors. All the five standard responses of SUF, such as low pass (LP), high pass (HP), band pass (BP), band-reject (BR), and all pass (AP), are obtained simultaneously. The main advantage of SUF over NSUF is the ease of orthogonal tuning of the pole frequency (ω_o) and quality factor (Q_o) with the bias currents of CCCTA and EX-CCCTA. It is suitable for full cascadability because of proper input and output impedances. Moreover, it simplifies integrated circuit implementation because all capacitors are grounded and no resistors are required. It does not possess any component matching constraints and consumes 4.1mW of power. The theoretical results have been validated in TSMC 180nm technology using Cadence Virtuoso.

Keywords: CCCTA; EX-CCCTA; CCII; CM universal filter; CM shadow universal filter

Izboljšan tokovni bikvadrantni univerzalni filter v senci

Izvleček: V tem članku je izboljšan enovhodno-večizhodni (SIMO) tokovni bikvadratni univerzalni filter v senci (SUF) z uporabo dveh novih različic tokovnih pretvornikov druge generacije (CCII), in sicer kaskadnega transkonduktančnega ojačevalnika (CCCTA) in transkonduktančnega ojačevalnika z nadzorom toka (EX-CCCTA). Izhodi nizkoprepustnega in pasovnega prehoda univerzalnega filtra brez sence (NSUF), ki ga sestavlja CCCTA, se uporabljajo prek dveh povratnih poti am-prevodnikov z uporabo enega EX-CCCTA za izvedbo predlaganega SUF. Filter je brez uporov in uporablja le dva ozemljena kondenzatorja. Vseh pet standardnih odzivov SUF, kot so nizka prepustnost (LP), visoka prepustnost (HP), pasovna prepustnost (BP), zavrnitev pasu (BR) in celotna prepustnost (AP), se dobi hkrati. Glavna prednost SUF pred NSUF je enostavnost ortogonalnega nastavljanja polne frekvence (ω_o) in faktorja kakovosti (Q_o) z diagonalnimi tokovi CCCTA in EX-CCCTA. Zaradi ustreznih vhodnih in izhodnih impedanc je primeren za popolno kaskadnost. Poleg tega poenostavlja izvedbo integriranih vezij, saj so vsi kondenzatorji ozemljeni in upori niso potrebni. Nima nobenih omejitev glede usklajevanja komponent in porabi le 4,1 mW energije. Teoretični rezultati so bili potrjeni v 180 nm tehnologiji TSMC z uporabo programa Cadence Virtuoso.

Ključne besede: CCCTA; EX-CCCTA; CCII; CM univerzalni filter; CM universal filter v senci

** Corresponding Author's e-mail: sajalkpaul@rediffmail.com*

1 Introduction

Current-mode (CM) universal filters, especially the single-input multiple-output (SIMO) type, have received significant attention [1-3] because of their wide applications. They are useful for many applications, namely communication systems, instrumentation, control systems,

How to cite:
D. Singh et al., "Improved Current Mode Biquadratic Shadow Universal Filter", Inf. Midem-J. Microelectron. Electron. Compon. Mater., Vol. 52, No. 1(2022), pp. 51–66

signal generation, and signal processing. Moreover, the possibility of simultaneous realization of multiple filter functions with the same topology finds use in PLL FM demodulator, touch-tone phone, and crossover network used in a three-way high-fidelity loud-speaker [4]. A reasonably good filter should have the following important features: simultaneous realization of various filter responses, use of few active and passive components, full cascadability i.e., low input impedance and high output impedance, all grounded components, low space requirement, no component matching constraints, low sensitivity, low power consumption, ease of orthogonal adjustment of pole frequency (ω_o) and quality factor (Q_o) including electronic tuning of various parameters. It may be appreciated that among the many parameters, the orthogonal tuning of ω_o and Q_o and electronic tuning plays a crucial role, primarily when the filter is implemented as an integrated circuit (IC). The literature survey reveals that many biquadratic current mode filters lack orthogonal electronic tuning capability.

Shadow filters introduce simple orthogonal electronic tuning of ω_o and Q_o of a core filter via amplifier gain. Lakys and Fabre [5, 6] introduced the shadow filter (also termed as frequency-agile filter) in 2010, where the low pass output of a second order core filter (non-shadow filter) is fed back to the input through an amplifier. This resulted in capability to control ω_o and Q_o (but not bandwidth (BW)) via gain; moreover, ω_o and Q_o cannot be tuned independently. Biolkova and Biolek [7] extended the idea, as shown in Fig. 1, and achieved an enhanced flexibility in the control of ω_o, Q_o and BW of the filter by gain of one or more feedback amplifier(s) connected externally [7].

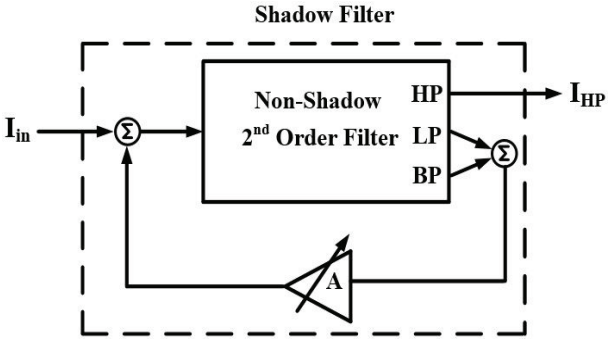

Figure 1: Scheme of Shadow filter [6].

A large diversity of SIMO filters are reported [1-4, 8-43]. Filter topologies [1-4, 8-28] are non-shadow (NS) type, while filter topologies [29-43] are shadow (S) type. Further, [29-35] are current-mode (CM) types and [36-43] are voltage-mode (VM) types.

In [1], non-shadow universal filters (NSUF) using four CFTAs and two grounded capacitors are reported. However, the simultaneous UF responses and ease of orthogonal tuning of ω_o and Q_o are not possible [1]. The topology [2] uses two CCCIIs, one MO-CCCA, and two grounded capacitors. In [3], four MO-OTAs are used. It has the following shortcomings: it does not possess full cascadability, requires matching constraints for UF realization, and independent control of ω_o and Q_o is not possible for the LP filter. In [4], an NSUF using three differential voltage current conveyors (DVCCs) and six passive elements without full cascadability is presented. In [8], the LP, HP, and BP filter are realized using one current follower transconductance amplifier (CFTA). However, one output is obtained through a capacitor; hence its practical implementation needs additional circuitry. A single current conveyor transconductance amplifier (CCTA) based NSUF is implemented in [9]. Again, a universal filter is reported with three DVCCs and six MOS resistors [10] without simultaneous responses and electronic tunability. Two operational transconductance amplifiers (OTAs) based NSUF circuit is presented in [11]. Moreover, NSUF in [12], using four Z-copy current follower transconductance amplifiers (ZC-CFTAs), provides simultaneous responses. On the other hand, NSUF using two Z-copy current inverter transconductance amplifiers (ZC-CITAs) is implemented in [13]. In [14], three MOCCCIIs are used, but the circuit does not provide full cascadability and ease of orthogonality. Further, one voltage differencing gain amplifier (VDGA) along with two resistors and capacitors are used for implementing multifunctional filters [15]. In [16], a universal filter without independent tunability is reported by employing two extra X current conveyor transconductance amplifier and six passive elements. Three/four second-generation current-controlled conveyors (DOCCCIIs/CCCIIs) [17, 19, 21] and three ZC-CFTAs [20] with minimal passive elements are used to realize NSUFs with simultaneous responses. In [18], a universal filter is reported consisting of one dual-X current conveyor transconductance amplifier (DXCCTA) with three passive elements. Furthermore, an NSUF is reported in [22] using two OTAs and one third-generation current conveyor (CCIII) with three passive elements. A universal filter [23] with two DVCCs and five passive components is reported. In [24], a multifunction filter is realized using voltage differencing dual X current conveyor with two grounded capacitors and two grounded resistors. Moreover, two multiple-output-operational floating conveyors (MOOFCs) with four passive elements provide an NSUF [25] with no simultaneous responses. A BJT-based universal filter is realized in [26] with two grounded capacitors. Moreover, an NSUF using a single VDTA and three passive components is reported in [27]. A universal filter is realized in [28] without full cascadability and ease of independent tunability. The available shadow filters (SFs) are reported [29-43]. The CDTA/VDTA based shadow

filters [29] realize only LP and BP through the capacitor with no full casacadability. Further, the shadow filter topology [30] reports only BP response utilizing a capacitor, but without full cascadability and orthogonal tuning of ω_o and Q_o. Moreover, shadow filter topology [31] realizes multifunction filters (LP, BP, and HP) using three CDTAs. However, the obtained BP and HP current signal conducted through a series capacitor to ground and hence extra circuitry is required to use these responses practically. It does not have the ease of cascadability and orthogonal tunability. Four OFCCs with five resistors and two capacitors implement a shadow BP filter [32] with no electronic tuning. Similarly, a BP filter with two CDTAs, one current amplifier (CA), and two capacitors is implemented [33]. Another shadow BP filter using four ECCII and four passive elements is reported [34] without full cascadability and electronic tuning. In [35], two CM shadow filters are reported. The first is a multifunction filter (LP, HP, and BP) using two CC-CDCTAs and two grounded capacitors. However, the obtained HP current signal conducted through a series capacitor to ground, and hence extra circuitry is required as of to use it practically. The second one is a shadow UF (SUF) using three CC-CDCTA, one CCCII, and two capacitors, of which one is floating. This is probably the first reported CM SUF. In [36, 43], VM shadow filters are comprised with differential difference current conveyor with higher number of passive elements without full cascadability. Op-amps are employed [37] to realize multifunction VM shadow filter with limitations on gain-bandwidth product and slew rate. Current feedback operational amplifiers (CFOAs) with higher number of passive elements are utilized to realize a multifunctional VM filter without simultaneous responses in [38] and single response filter in [39, 40]. In [41], three operational transresistance amplifiers (OTRAs) with eleven resistors and four capacitors are employed and provide only low-pass and band-pass responses. A VM shadow filter is realized in [42] using three voltage differencing differential-difference amplifiers (VDDDAs). To our best knowledge the work [42] reports the first VM shadow universal filter.

This paper describes a realization of an improved resistorless biquadratic current mode SUF. It uses two modified active building blocks, namely current conveyor cascaded transconductance amplifier (CCCTA) and extra-X current controlled conveyor transconductance amplifier (EX-CCCTA). The proposed shadow filter possesses the following advantageous features: simultaneous realization of various filter responses without alteration of the circuit, no component matching constraints, use of only two ABBs and two grounded capacitors, it is resistorless, fully cascadable, has low sensitivity and low power consumption, provides the possibility of orthogonally adjustment of the pole frequency (ω_o) and the quality factor (Q_o) including electronic tuning of various parameters, and is suitable for integrated circuit implementation. To distinguish the similar mathematical and non-mathematical symbols with reference to both the blocks, superscripts (1) and (2) have been used all through the paper for the CC-CTA and EX-CCCTA, respectively. Such as, $M_1^{(1)}$, $g_{m1}^{(1)}$ and $I_Y^{(1)}$ represent for CCCTA while $M_{20}^{(2)}$, $g_{m1}^{(2)}$ and $I_Y^{(2)}$ represent for EX-CCCTA.

This paper consists of six sections. Section 1 gives the introduction, followed by Section 2, which describes active building blocks. Section 3 discusses the proposed universal shadow filter and its analysis. Section 4 gives the non-ideality analysis while the proposed circuit is compared to existing filters in section 5. Verification through simulation and experimentation is given in section 6 and section 7, respectively, followed by the conclusion in section 8.

2 Active building blocks

In this section, two active building blocks, CCCTA and EX-CCCTA, are being discussed. These building blocks are used for UF realization.

2.1 Current conveyor cascaded transconductance amplifier (CCCTA)

The second-generation current conveyor (CCII) is a well-known current mode building block. The CCII structure has two input terminals, X and Y, at low and high impedance respectively, and one high impedance output terminal, Z. In [44], a BJT based CCII is modified into a current conveyor transconductance amplifier (CCTA) by the addition of transconductance amplifier (TA) at the Z terminal of CCII in series. This paper proposes a new variant of CCII, composed of CCTA followed by an additional TA in cascade resulting in a current conveyor cascaded transconductance amplifier (CCCTA). The symbol of the proposed CCCTA is shown in Fig. 2, and its CMOS-based internal structure is shown in Fig. 3. The first stage, CCII, is composed of $M_1^{(1)}$ - $M_9^{(1)}$, and after that, two TA stages, formed by $M_{10}^{(1)}$ - $M_{17}^{(1)}$, are cascaded.

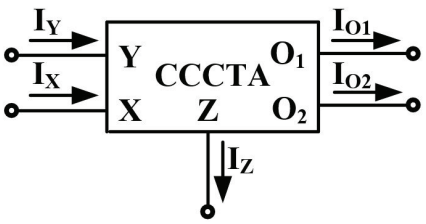

Figure 2: Symbol of CCCTA.

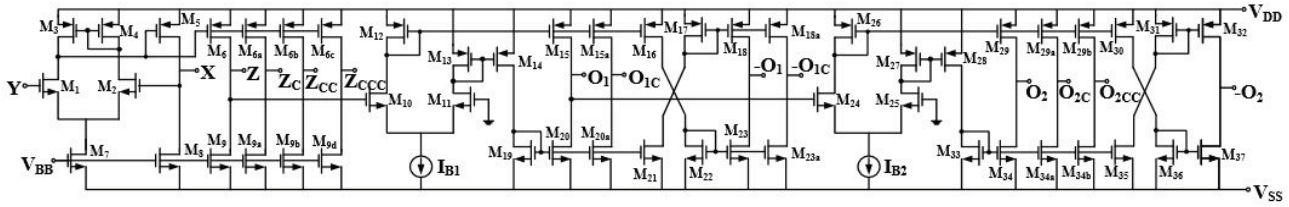

Figure 3: The CMOS-based Internal structure of CCCTA

The port relationships for CCCTA are given as follows:

$$\begin{bmatrix} I_Y^{(1)} \\ V_X^{(1)} \\ I_Z^{(1)} \\ I_{O1}^{(1)} \\ I_{O2}^{(1)} \end{bmatrix} = \begin{bmatrix} 0 & 0 & 0 & 0 & 0 \\ 1 & 0 & 0 & 0 & 0 \\ 0 & 1 & 0 & 0 & 0 \\ 0 & 0 & g_{m1}^{(1)} & 0 & 0 \\ 0 & 0 & 0 & g_{m2}^{(1)} & 0 \end{bmatrix} \begin{bmatrix} V_Y^{(1)} \\ I_X^{(1)} \\ V_Z^{(1)} \\ V_{O1}^{(1)} \\ V_{O2}^{(1)} \end{bmatrix} \quad (1)$$

Where $g_{m1}^{(1)}$ d $g_{m2}^{(1)}$ are the transconductances of the first and second TA, respectively. They can be expressed as:

$$g_{m1}^{(1)} = \sqrt{\mu_n C_{ox} \left(\frac{W}{L}\right)_{M_{10}^{(1)},\ M_{11}^{(1)}} I_{B1}} \quad (2a)$$

$$g_{m2}^{(1)} = \sqrt{\mu_n C_{ox} \left(\frac{W}{L}\right)_{M_{14}^{(1)},\ M_{15}^{(1)}} I_{B2}} \quad (2b)$$

Where μ, C_{ox}, W/L, I_{B1}, and I_{B2} have their usual meaning. The proposed CCCTA is designed in TSMC 180 nm technology. The aspect ratios of transistors are given in Table 1.

Table 1: The aspect ratio of MOS Transistors of CCCTA.

MOS Transistors	W(μm)/ L(μm)	MOS Transistors	W(μm)/ L(μm)
$M_{1,7}^{(1)}$	7.2/0.36	$M_{5,6}^{(1)}$	6.12/0.36
$M_{2}^{(1)}$	19.6/0.36	$M_{8,9}^{(1)}$	31.6/0.36
$M_{3,4}^{(1)}$	3.6/0.36	$M_{10-37}^{(1)}$	10.8/0.36

The essential features of the CCCTA in Fig. 2 can be verified through simulation. The dc current and voltage characteristics, $I_Z^{(1)}$ versus $I_X^{(1)}$ and $V_X^{(1)}$ versus $V_Y^{(1)}$, are shown in Fig. 4. The dc current characteristic is almost linear for the range of -376 μA to 500 μA while the dc voltage characteristic is linear for the range of -1.14 V to 1.14 V. Fig. 5 shows the frequency response of current gains, $I_Z^{(1)} / I_X^{(1)}$, $I_{O1}^{(1)} / I_X^{(1)}$, and $I_{O2}^{(1)} / I_X^{(1)}$ with a -3 dB bandwidths being 1.4 GHz, 45.7 MHz, and 45.7 MHz, respectively. It is observed from Fig. 5 (b) that the gains $I_{O1}^{(1)} / I_X^{(1)}$ and $I_{O2}^{(1)} / I_X^{(1)}$ overlap. Table 2 summarizes the performance parameters of CCCTA.

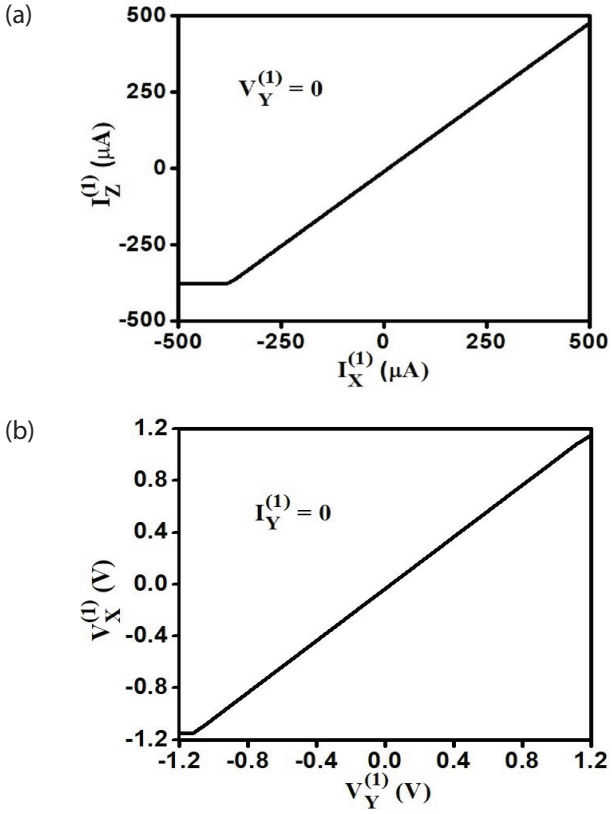

Figure 4: The plot of dc characteristics (a) I_Z versus I_X (b) V_X versus V_Y.

2.2 Extra-X second generation current controlled conveyor transconductance amplifier (EX-CCCTA)

Extra X- second generation current controlled conveyor (EX-CCCII) is one of the variants of CCCII, which adds one more X terminal and, therefore, extra intrinsic resistance at X terminal. This paper introduces a new variant of CCCII, an extra-X second-generation current controlled conveyor transconductance amplifier (EX-CCCTA), in which two TAs are connected at two Z terminals. The symbol of EX-CCCTA is shown in Fig. 6, and its CMOS internal structure, as shown in Fig. 7, is modified from ref. [45].

(a)

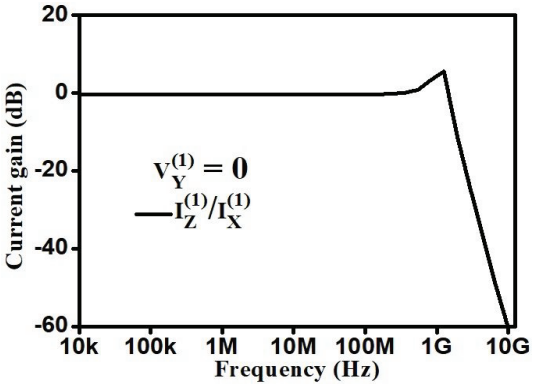

(b)

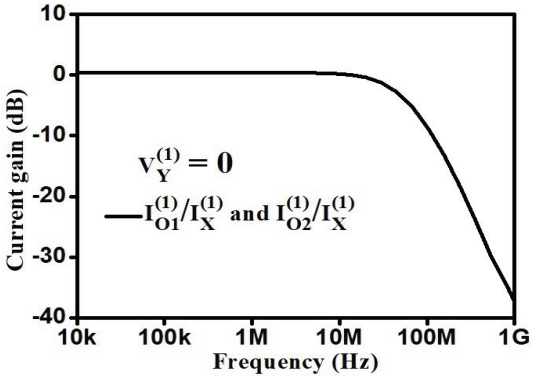

Figure 5: Current gain frequency response at (a) Z, (b) O_1 and O_2

Table 2: Performance parameters of CCCTA.

Parameters	Values
Supply Voltage	± 1.5 V
Power Consumption for V_{BB} = -1 V, $I_{B1} = I_{B2}$ = 56 µA	3.6 mW
Parasitics at Y port ($R_Y^{(1)}$, $C_Y^{(1)}$)	360 kΩ, 2.73 fF
Parasitics at X port ($R_X^{(1)}$)	679 Ω
Parasitics at Z port ($R_Z^{(1)}$, $C_Z^{(1)}$)	4.38 MΩ, 4.12 fF
Parasitics at O_1 port ($R_{O1}^{(1)}$, $C_{O1}^{(1)}$)	2.54 MΩ, 3.42 fF
Parasitics at O_2 port ($R_{O2}^{(1)}$, $C_{O2}^{(1)}$)	2.3 MΩ, 3.24 fF
Linear variation of $I_Z^{(1)}$ over $I_X^{(1)}$	-376 µA to 500 µA
Linear variation of $V_X^{(1)}$ over $V_Y^{(1)}$	-1.14 V to 1.14 V
Bandwidth of $I_Z^{(1)} / I_X^{(1)}$	1.4 GHz
Bandwidth of $I_{O1}^{(1)} / I_X^{(1)}$	45.7 MHz
Bandwidth of $I_{O2}^{(1)} / I_X^{(1)}$	45.7 MHz

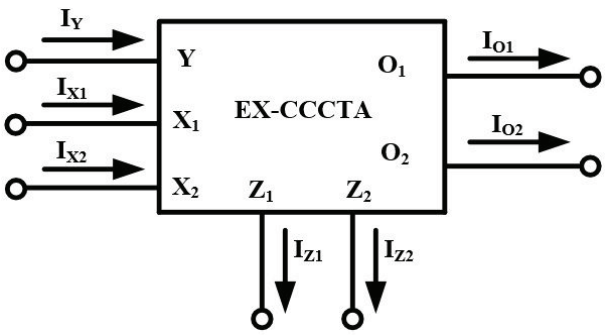

Figure 6: Symbol of EX-CCCTA.

The port relationships for EX-CCCTA are as follows:

$$\begin{bmatrix} I_Y^{(2)} \\ V_{X1}^{(2)} \\ V_{X2}^{(2)} \\ I_{Z1}^{(2)} \\ I_{Z2}^{(2)} \\ I_{O1}^{(2)} \\ I_{O2}^{(2)} \end{bmatrix} = \begin{bmatrix} 0 & 0 & 0 & 0 & 0 & 0 & 0 \\ 1 & R_{X1}^{(2)} & 0 & 0 & 0 & 0 & 0 \\ 1 & 0 & R_{X2}^{(2)} & 0 & 0 & 0 & 0 \\ 0 & 1 & 0 & 0 & 0 & 0 & 0 \\ 0 & 0 & 1 & 0 & 0 & 0 & 0 \\ 0 & 0 & 0 & g_{m1}^{(2)} & 0 & 0 & 0 \\ 0 & 0 & 0 & 0 & g_{m2}^{(2)} & 0 & 0 \end{bmatrix} \begin{bmatrix} V_Y^{(2)} \\ I_{X1}^{(2)} \\ I_{X2}^{(2)} \\ V_{Z1}^{(2)} \\ V_{Z2}^{(2)} \\ V_{O1}^{(2)} \\ V_{O2}^{(2)} \end{bmatrix} \quad (3)$$

$R_{X1}^{(2)}$ and $R_{X2}^{(2)}$ are the intrinsic resistances at the X_1 and X_2 terminals, respectively. Parasitics at Y port are given by ($R_Y^{(2)}$, $C_Y^{(2)}$). Similarly, $g_{m1}^{(2)}$ and $g_{m2}^{(2)}$ are the transconductances of the first and second TA. Values of $R_{X1}^{(2)}$ and $R_{X2}^{(2)}$ can be computed as:

$$R_{X1}^{(2)} = R_{X2}^{(2)} \cong \frac{1}{\sqrt{2I_{C1}C_{OX}}\left(\sqrt{\frac{\mu_p W_p}{L_p}} + \sqrt{\frac{\mu_n W_n}{L_n}}\right)} \quad (4)$$

The values of $R_{X1}^{(2)}$ and $R_{X2}^{(2)}$ are equal when $\left(\frac{W}{L}\right)_{M_2^{(2)}} = \left(\frac{W}{L}\right)_{M_3^{(2)}}$ and $\left(\frac{W}{L}\right)_{M_5^{(2)}} = \left(\frac{W}{L}\right)_{M_6^{(2)}}$.

The analysis of the operational transconductance amplifier yields

$$g_{m1}^{(2)} = \sqrt{\mu_n C_{ox}\left(\frac{W}{L}\right)_{M_{20}^{(2)},\ M_{21}^{(2)}} I_{C2}} \quad (5a)$$

$$g_{m2}^{(2)} = \sqrt{\mu_n C_{ox}\left(\frac{W}{L}\right)_{M_{24}^{(2)},\ M_{25}^{(2)}} I_{C3}} \quad (5b)$$

Where μ is the mobility, C_{OX} is the oxide capacitance, W/L is the aspect ratio and I_{C2}, I_{C3} are the bias currents. The proposed EX-CCCTA is designed in TSMC 180 nm CMOS technology, the aspect ratios of transistors are given in Table 3.

Table 3: The aspect ratio of EX-CCCTA of Fig. 7.

MOS Transistors	W(μm)/ L(μm)	MOS Transistors	W(μm)/ L(μm)
$M^{(2)}_{1,\,2,\,3}$	11.5/0.36	$M^{(2)}_{13-19}$	4.5/0.36
$M^{(2)}_{4-12}$	7.2/0.36	$M^{(2)}_{20-43}$	10.8/0.36

The basic architecture of EX-CCCTA is similar to CCCTA. Hence, the simulated responses of EX-CCCTA are the same as the responses of the CCCTA block.

3 Proposed shadow filter realization

The shadow filter implementation using two feedback amplifiers, as given in Fig. 1 [6], is adopted in this paper to improve the non-shadow filter performance. The band pass and low pass responses of the non-shadow filter are fed back to the input through amplifiers A_1 and A_2, respectively. The shadow universal filter (SUF) realization, in line with Fig. 1, is shown in Fig. 8. One of the constituents of it is NSUF, shown inside the small dotted lines. Hence, at first, we briefly discuss NSUF realization, followed by the realization of SUF.

The proposed SIMO current mode (CM) second-order NSUF using a single CCCTA and two grounded capacitors is shown in Fig. 8 inside the small dotted lines. Where $Z_C^{(1)}$, $Z_{CC}^{(1)}$, and $Z_{CCC}^{(1)}$ are the $Z^{(1)}$ copies. The $O_{1C}^{(1)}$, and $O_{1CC}^{(1)}$, are $O_1^{(1)}$ copies, and similarly, $O_2^{(1)}$ copies are represented. The current at terminals $-O_1^{(2)}$ and $-O_2^{(2)}$ is 180 degree phase shifted over $O_1^{(2)}$ and $O_2^{(2)}$ terminals, respectively. The proposed filter provides all the standard UF responses such as low pass, band pass, high pass, band-reject, and all pass simultaneously. It has low input impedance and high output impedances, suitable for full cascading in the current mode. The routine analysis of NSUF results in the pole frequency and quality factor as:

$$Pole\ freq. = \sqrt{\frac{g_{m1}^{(1)} g_{m2}^{(1)}}{C_1 C_2}}\ ,Q.\ factor = \sqrt{\frac{C_1 g_{m2}^{(1)}}{C_2 g_{m1}^{(1)}}}$$
$$Bandwidth = \frac{g_{m1}^{(1)}}{C_1} \quad (6)$$

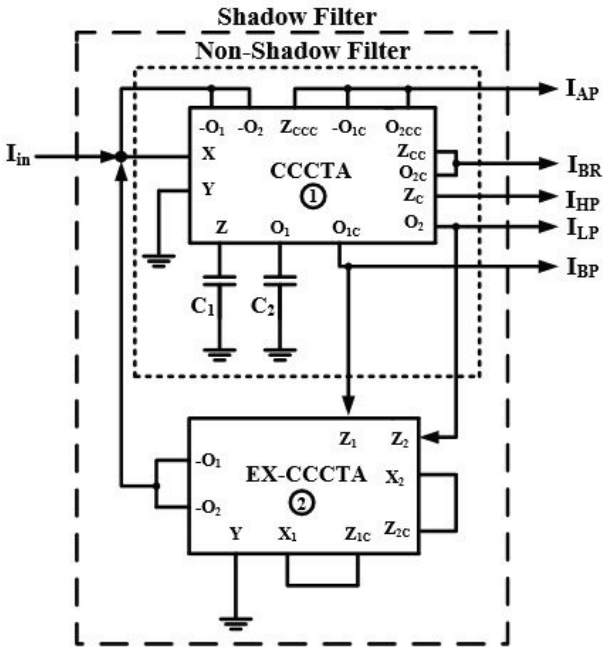

Figure 8: Proposed Shadow universal filter.

Equation (5) indicates that the pole frequency, quality factor, and bandwidth are electronically tunable by bias currents because of $g_{m1}^{(1)}$ and $g_{m2}^{(1)}$. Moreover, pole frequency can easily be tuned independently of quality factor by varying $g_{m1}^{(1)} = g_{m2}^{(1)} = g_m$ with bias currents. However, the quality factor cannot be tuned independently of pole frequency easily.

It is also observed from Fig. 8 that the proposed SUF is realized with CCCTA based NSUF and EX-CCCTA. The two current amplifiers A_1 and A_2, are implemented using one EX-CCCTA. The amplifier gains are expressed as $A_1 = g_{m1}^{(2)} R_{X1}^{(2)}$ and $A_2 = g_{m2}^{(2)} R_{X2}^{(2)}$, where $g_{m1}^{(2)}$ and $g_{m2}^{(2)}$ are

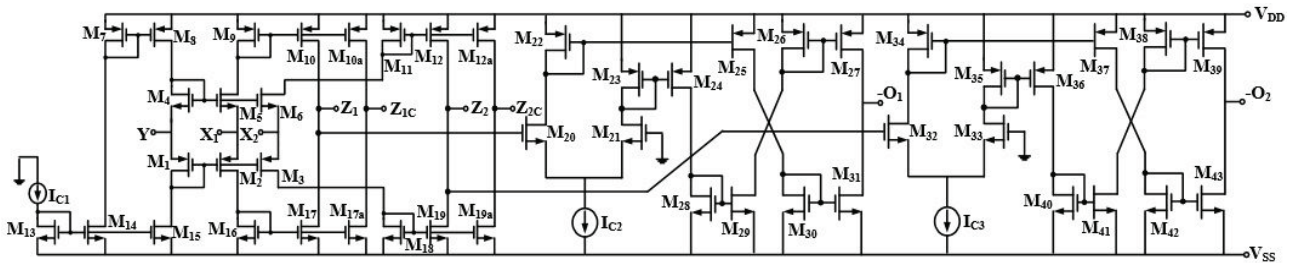

Figure 7: The CMOS-based internal structure of EX-CCCTA.

the first and second transconductances of the second analog building block (ABB), EX-CCCTA.

Thereafter, the routine analysis of the circuit of Fig. 8 results in the transfer functions as follows:

$$\frac{I_{LP}}{I_{in}}=\frac{g_{m1}^{(1)}g_{m2}^{(1)}}{D(s)} \tag{7}$$

$$\frac{I_{BP}}{I_{in}}=\frac{sC_2g_{m1}^{(1)}}{D(s)} \tag{8}$$

$$\frac{I_{HP}}{I_{in}}=\frac{s^2C_1C_2}{D(s)} \tag{9}$$

$$\frac{I_{BR}}{I_{in}}=\frac{s^2C_1C_2+g_{m1}^{(1)}g_{m2}^{(1)}}{D(s)} \tag{10}$$

$$\frac{I_{AP}}{I_{in}}=\frac{s^2C_1C_2-sC_2g_{m1}^{(1)}+g_{m1}^{(1)}g_{m2}^{(1)}}{D(s)} \tag{11}$$

where,

$$D(s)=s^2C_1C_2+sC_2g_{m1}^{(1)}(1+A_1)+g_{m1}^{(1)}g_{m2}^{(1)}(1+A_2) \tag{12}$$

The equations (7) – (11) show that all the standard responses of SUF such as low pass (LP), high pass (HP), band pass (BP), band-reject (BR), and all pass (AP) have been realized simultaneously.

The above transfer functions results in the following gains:

$$A_{LP}=A_{BR}=\frac{1}{1+A_2},A_{BP}=\frac{1}{1+A_1},A_{HP}=A_{AP}=1 \tag{13}$$

The denominator of the above transfer functions results in the pole frequency (ω_o), quality factor (Q_o) and the bandwidth (BW) of the SUF given by:

$$\omega_o=\sqrt{\frac{g_{m1}^{(1)}g_{m2}^{(1)}(1+A_2)}{C_1C_2}} \tag{14a}$$

$$Q_o=\frac{1}{(1+A_1)}\sqrt{\frac{C_1g_{m2}^{(1)}(1+A_2)}{C_2g_{m1}^{(1)}}} \tag{14b}$$

$$BW=\frac{g_{m1}^{(1)}(1+A_1)}{C_1} \tag{14c}$$

If $g_{m1}^{(1)}=g_{m2}^{(1)}=g_m$ and $C_1=C_2=C$, then the above equation can be rewritten as:

$$\omega_o=\frac{g_m}{C}\sqrt{(1+A_2)}\ ,Q_o=\frac{\sqrt{(1+A_2)}}{(1+A_1)} \tag{15a}$$

$$BW=\frac{g_m(1+A_1)}{C} \tag{15b}$$

The sensitivity analysis of ω_o, Q_o, and BW using (14) results in:

$$S_{g_{m1}^{(1)}}^{\omega_o}=S_{g_{m2}^{(1)}}^{\omega_o}=\frac{1}{2},\quad S_{C_1}^{\omega_o}=S_{C_2}^{\omega_o}=-\frac{1}{2},\quad S_{g_{m2}^{(2)}}^{\omega_o}=S_{R_{X2}^{(2)}}^{\omega_o}=\frac{1}{2}\left(\frac{A_2}{1+A_2}\right) \tag{16}$$

$$S_{g_{m1}^{(2)}}^{Q_o}=S_{R_{X1}^{(2)}}^{Q_o}=-\frac{A_1}{1+A_1},\ S_{C_1}^{Q_o}=S_{g_{m2}^{(1)}}^{Q_o}=\frac{1}{2},\quad S_{C_2}^{Q_o}=S_{g_{m1}^{(1)}}^{Q_o}=-\frac{1}{2},S_{g_{m2}^{(2)}}^{Q_o}=S_{R_{X2}^{(2)}}^{Q_o}=\frac{1}{2}\left(\frac{A_2}{1+A_2}\right) \tag{17}$$

$$S_{g_{m1}^{(2)}}^{BW}=S_{R_{X1}^{(2)}}^{BW}=-\frac{A_1}{1+A_1}\ ,\ S_{g_{m1}^{(1)}}^{BW}=1,S_{C_1}^{BW}=-1 \tag{18}$$

It is observed from equation (15) that Q_o can be adjusted independently of ω_o by electronically controlling the value of A_1 with $g_{m1}^{(2)}$. Similarly, ω_o can be adjusted independently of Q_o by electronically controlling g_m. Also, BW can be electronically controlled independently of ω_o by controlling A_1 with $g_{m1}^{(2)}$. Furthermore, BW can be tuned independently from Q_o via g_m. It is also evident from equation (13) that AP, BP, and BR gains can be electronically controlled with A_1 and A_2. The sensitivities of all the parameters are within unity in magnitude irrespective of the value of A_1 and A_2. Thus, the most important achievement of SUF over NSUF is the ease of orthogonal adjustment of pole frequency and quality factor.

4 Non-ideality analysis

Practically there will be effects of non-ideal transfer gains and parasitics of active building blocks. The effects of these two types of non-idealities are discussed in section 4.1 and 4.2.:

4.1 Non-ideal transfer gain of CCCTA

Considering the non-idealities of voltage, current and transconductance gains of CCCTA, the port relationship modifies as:

$$\begin{bmatrix} I_Y^{(1)} \\ V_X^{(1)} \\ I_Z^{(1)} \\ I_{O1}^{(1)} \\ I_{O2}^{(1)} \end{bmatrix} = \begin{bmatrix} 0 & 0 & 0 & 0 & 0 \\ \beta_1^{(1)} & 0 & 0 & 0 & 0 \\ 0 & \alpha_1^{(1)} & 0 & 0 & 0 \\ 0 & 0 & \gamma_1^{(1)} g_{m1}^{(1)} & 0 & 0 \\ 0 & 0 & 0 & \gamma_2^{(1)} g_{m2}^{(1)} & 0 \end{bmatrix} \begin{bmatrix} V_Y^{(1)} \\ I_X^{(1)} \\ V_Z^{(1)} \\ V_{O1}^{(1)} \\ V_{O2}^{(1)} \end{bmatrix} \quad (19)$$

While, the non-ideal port relationships of an EX-CCCTA are:

$$\begin{bmatrix} I_Y^{(2)} \\ V_{X1}^{(2)} \\ V_{X2}^{(2)} \\ I_{Z1}^{(2)} \\ I_{Z2}^{(2)} \\ I_{O1}^{(2)} \\ I_{O2}^{(2)} \end{bmatrix} = \begin{bmatrix} 0 & 0 & 0 & 0 & 0 & 0 & 0 \\ \beta_1^{(2)} & R_{X1}^{(2)} & 0 & 0 & 0 & 0 & 0 \\ \beta_2^{(2)} & 0 & R_{X2}^{(2)} & 0 & 0 & 0 & 0 \\ 0 & \alpha_1^{(2)} & 0 & 0 & 0 & 0 & 0 \\ 0 & 0 & \alpha_2^{(2)} & 0 & 0 & 0 & 0 \\ 0 & 0 & 0 & \gamma_1^{(2)} g_{m1}^{(2)} & 0 & 0 & 0 \\ 0 & 0 & 0 & 0 & \gamma_2^{(2)} g_{m2}^{(2)} & 0 & 0 \end{bmatrix} \begin{bmatrix} V_Y^{(2)} \\ I_{X1}^{(2)} \\ I_{X2}^{(2)} \\ V_{Z1}^{(2)} \\ V_{Z2}^{(2)} \\ V_{O1}^{(2)} \\ V_{O2}^{(2)} \end{bmatrix} \quad (20)$$

Where $\beta^{(i)}$ (i= 1, 2) is the voltage transfer gain between Y and $X^{(i)}$ terminals, $\alpha^{(i)}$ is the current transfer gain between $X^{(i)}$ and $Z^{(i)}$ terminals, $\gamma_1^{(i)}$ and $\gamma_2^{(i)}$ are the gains from $Z^{(i)}$ to $O_1^{(i)}$ and $O_1^{(i)}$ to $O_2^{(i)}$ terminals, respectively. The above gain factors are ideally found to be unity while practically they may slightly deviate from unity. After considering the non-ideality the transfer functions of Fig. 8 are obtained as:

$$\frac{I_{LP}}{I_{in}} = \frac{\gamma_1^{(1)}\gamma_2^{(1)}\alpha_1^{(1)}\alpha_1^{(2)}\alpha_2^{(2)} g_{m1}^{(1)} g_{m2}^{(1)}}{D(s)} \quad (21)$$

$$\frac{I_{BP}}{I_{in}} = \frac{sC_2\gamma_1^{(1)}\alpha_1^{(1)}\alpha_1^{(2)}\alpha_2^{(2)} g_{m1}^{(1)}}{D(s)} \quad (22)$$

$$\frac{I_{HP}}{I_{in}} = \frac{s^2 C_1 \alpha_1^{(1)}\alpha_1^{(2)}\alpha_2^{(2)}}{D(s)} \quad (23)$$

$$\frac{I_{BR}}{I_{in}} = \frac{\alpha_1^{(1)}\alpha_1^{(2)}\alpha_2^{(2)}\left(s^2 C_1 C_2 + \gamma_1^{(1)}\gamma_2^{(1)} g_{m1}^{(1)} g_{m2}^{(1)}\right)}{D(s)} \quad (24)$$

$$\frac{I_{AP}}{I_{in}} = \frac{\alpha_1^{(1)}\alpha_1^{(2)}\alpha_2^{(2)}\left(s^2 C_1 C_2 - sC_2\gamma_1^{(1)} g_{m1}^{(1)} + \gamma_1^{(1)}\gamma_2^{(1)} g_{m1}^{(1)} g_{m2}^{(1)}\right)}{D(s)} \quad (25)$$

Where,

$$D(s) = s^2 C_1 C_2 \alpha_1^{(2)}\alpha_2^{(2)} + sC_2 g_{m1}^{(1)}\gamma_1^{(1)}\alpha_1^{(1)}\alpha_2^{(2)}(\alpha_1^{(2)} + A_1\gamma_1^{(2)}) + \gamma_1^{(1)}\gamma_2^{(1)}\alpha_1^{(1)}\alpha_1^{(2)} g_{m1}^{(1)} g_{m2}^{(1)}(\alpha_2^{(2)} + A_2\gamma_2^{(2)}) \quad (26)$$

Therefore, the pole frequency (ω_o) and the quality factor (Q_o) are:

$$\omega_o = \sqrt{\frac{\gamma_1^{(1)}\gamma_2^{(1)}\alpha_1^{(1)} g_{m1}^{(1)} g_{m2}^{(1)}\left(\alpha_2^{(2)} + A_2\gamma_2^{(2)}\right)}{\alpha_2^{(2)} C_1 C_2}} \quad (27a)$$

$$Q_o = \frac{\alpha_1^{(2)}}{\left(\alpha_1^{(2)} + A_1\gamma_1^{(2)}\right)}\sqrt{\frac{C_1 g_{m2}^{(1)}\gamma_2^{(1)}\left(\alpha_2^{(2)} + A_2\gamma_2^{(2)}\right)}{C_2 g_{m1}^{(1)}\gamma_1^{(1)}\alpha_1^{(1)}\alpha_2^{(2)}}} \quad (27b)$$

$$BW = \frac{g_{m1}^{(1)}\gamma_1^{(1)}\alpha_1^{(1)}\left(\alpha_1^{(2)} + A_1\gamma_1^{(2)}\right)}{\alpha_1^{(2)} C_1} \quad (27c)$$

From the Eq. (27), the effects due to non-idealities of CCCTA and EX-CCCTA can be easily observed. For the ideal cases, the current gains and transconductance gains are unity and Eq. (27) reverts to Eq. (14).

4.2 Effects of parasitics

Fig. 9 shows the non-ideal equivalent circuit of CCCTA and EX-CCCTA with parasitics. Series resistance at X terminal is of very low value while $\left(C_Y^{(1)} \parallel R_Y^{(1)}\right)$, $\left(C_Z^{(1)} \parallel R_Z^{(1)}\right)$, $\left(C_{O1}^{(1)} \parallel R_{O1}^{(1)}\right)$, and $\left(C_{O2}^{(1)} \parallel R_{O2}^{(1)}\right)$ are at Y, Z, O_1, and O_2 terminals, respectively. The values of $R_Y^{(1)}$, $R_Z^{(1)}$, $R_{O1}^{(1)}$, and $R_{O2}^{(1)}$ are high whereas $C_Y^{(1)}$, $C_Z^{(1)}$, $C_{O1}^{(1)}$, and $C_{O2}^{(1)}$ are low. The non-ideal circuit of the proposed shadow filter is shown in Fig. 10 where impedances are:

$$Z_1 = R_Z^{(1)} \left\| C_1^{'} \right., Z_2 = R_{O1}^{(1)} \left\| C_2^{'} \right.,$$
$$Z_3 = R_{O1}^{(1)} \left\| R_{Z1}^{(2)} \right\| C_{O1}^{(1)} \left\| C_{Z1}^{(2)} \right., \; Z_4 = R_{O2}^{(1)} \left\| R_{Z2}^{(2)} \right\| C_{O2}^{(1)} \left\| C_{Z2}^{(2)} \right. \quad (28)$$
$$Z_5 = R_{Z1}^{(2)} \left\| C_{Z1}^{(2)} \right., \; Z_6 = R_{Z2}^{(2)} \left\| C_{Z2}^{(2)} \right.$$

Where,

$$C_1^{'} = C_1 + C_Z^{(1)} \text{ and } C_2^{'} = C_2 + C_{O1}^{(1)}$$

The routine analysis of Fig. 10 results in the following TFs:

$$\frac{I_{LP}}{I_{in}} = \frac{g_{m1}^{(1)} g_{m2}^{(1)}}{D(s)} \quad (29)$$

$$\frac{I_{BP}}{I_{in}} = \frac{\left(sC_2^{'} + \frac{1}{R_{O1}^{(1)}}\right) g_{m1}^{(1)}}{D(s)} \quad (30)$$

$$\frac{I_{HP}}{I_{in}} = \frac{\left(sC_1^{'} + \frac{1}{R_Z^{(1)}}\right)\left(sC_2^{'} + \frac{1}{R_{O1}^{(1)}}\right)}{D(s)} \quad (31)$$

$$\frac{I_{BR}}{I_{in}}=\frac{\left(sC_1^{'}+\frac{1}{R_Z^{(1)}}\right)\left(sC_2^{'}+\frac{1}{R_{O1}^{(1)}}\right)+g_{m1}^{(1)}g_{m2}^{(1)}}{D(s)} \tag{32}$$

$$\frac{I_{AP}}{I_{in}}=\frac{\left(sC_1^{'}+\frac{1}{R_Z^{(1)}}\right)\left(sC_2^{'}+\frac{1}{R_{O1}^{(1)}}\right)+\left(sC_2^{'}+\frac{1}{R_{O1}^{(1)}}\right)g_{m1}^{(1)}+g_{m1}^{(1)}g_{m2}^{(1)}}{D(s)} \tag{33}$$

Where,

$$\begin{aligned}D(s)=&\left(sC_1^{'}+\frac{1}{R_Z^{(1)}}\right)\left(sC_2^{'}+\frac{1}{R_{O1}^{(1)}}\right)\\&+\left(sC_2^{'}+\frac{1}{R_{O1}^{(1)}}\right)g_{m1}^{(1)}(1+A_1)\\&+g_{m1}^{(1)}g_{m2}^{(1)}(1+A_2)+E_1+E_2\end{aligned} \tag{34}$$

Where,

$$E_1=\frac{\left(sC_1^{'}+\frac{1}{R_Z^{(1)}}\right)\left(sC_2^{'}+\frac{1}{R_{O1}^{(1)}}\right)R_XA_1}{Z_3},$$

$$E_2=\frac{\left(sC_1^{'}+\frac{1}{R_Z^{(1)}}\right)\left(sC_2^{'}+\frac{1}{R_{O1}^{(1)}}\right)R_XA_2}{Z_4}$$

From the Eq. (29) to (34), the effects of parasitics of CCCTA and EX-CCCTA on filters are observed. It may be noticed that the effects of parasitic capacitances can be neglected by choosing C_1 and C_2 much higher then C_Z and C_{01}. Moreover, as the values of R_Z and R_{01} are high, of the order of few MΩ, their effects are not significant for a few tens of MHz. It may also be found that the values of E_1 and E_2 are negligible in comparison to the other terms in Eq. (34) for a wide frequency range.

5 Comparison with existing CM SIMO Filters

As the proposed work is on CM SIMO UF, a fair comparison is carried out with available similar types of UFs. The comparison of the available CM single-input-multiple-output (SIMO) UF is given in Table 4. The filter topologies

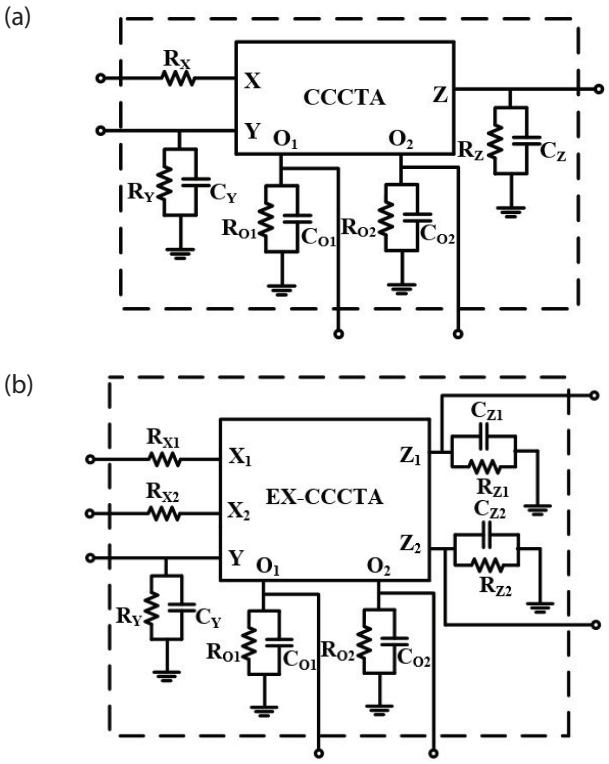

Figure 9: Non-ideal equivalent circuit of (a) CCCTA, (b) EX-CCCTA.

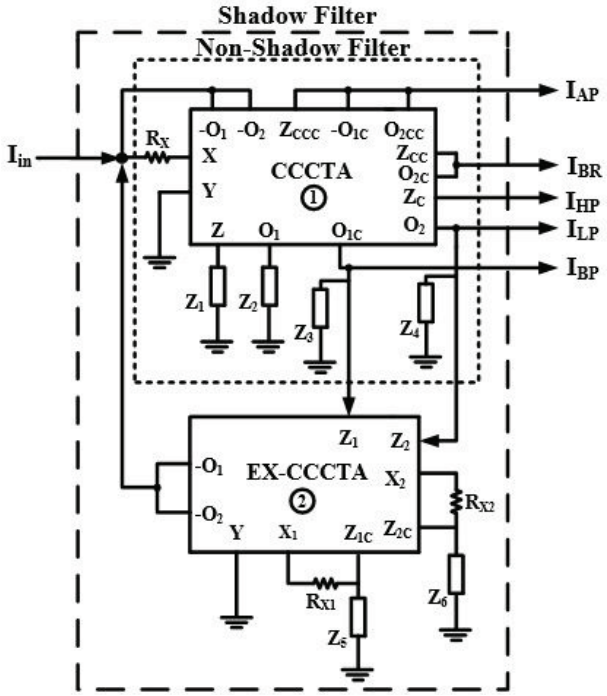

Figure 10: Non-ideal equivalent circuit of Fig. 8 with parasitic impedances.

[1-4, 8-28] are non-shadow (NS) type, while [29-35] are CM shadow (S) type. The filter topologies [8, 15, 24, 29-34, 35 (Fig. 9)] are single/multi-functional filters.

It is observed that topologies [1-4, 9-14, 16-23, 25-28, 35 (Fig. 10)] and proposed work are UFs. Whereas [26] is a direct realization using BJTs and excessive numbers of floating current sources. Its operating frequency is low, 100 kHz, and power consumption is 4.93mW. More than two analog building blocks (ABBs) are used in most UFs [1-4, 10, 12, 14, 17, 19-22, 35 (Fig. 10)], while the proposed shadow UF (SUF) uses two ABBs. Additionally, they suffer from one or more shortcomings as indicated in Table 4. It may be noted that topology [2]'s operating frequency is low, 39 kHz. Moreover, if the technique, as discussed in the paper [2], is applied for orthogonal tuning of ω_o and Q_o, then the AP filter will not work.

Furthermore, the UF topologies [11, 13, 16, 23, 25] use two ABBs. The UF topologies [11, 13, 16, 23] do not provide orthogonal tuning of ω_o and Q_o. Additionally, [11] has a low operating frequency and is not fully cascadable, while [16] does not provide simultaneous responses and independent tuning. The topology [23] uses two capacitors and three resistors, of which two are floating. Moreover, in [23], passive components matching constraints are required for UF realization. Further, unlike the proposed SUF, [23, 25] do not possess electronic tuning of ω_o and Q_o, and the full cascadability.

The UF topologies [9, 18, 27, 28] use one ABB compared to the two ABBs by the proposed SUF. However, the comparison Table 4 reveals that although these circuits use one ABB, the obtained current signals for HP and BP [9, 27] and that for HP [18, 28] conduct through series capacitors to ground, and hence they require significant additional circuitry for practical realization. As a consequence, for simultaneous realization, they need additional circuitry. As discussed in [18], the HP current can be made available from a high impedance terminal with one additional current conveyor and converting the corresponding grounded capacitor to a floating one. Moreover, [9, 18, 27, 28] are not cascadable without a buffer. Also, the power consumption is high in [27].

The power consumption of most of the available UFs is higher than the proposed work except [23, 35]. It is also noted that the operating frequency of 10 MHz and above is reported in [4, 10, 18, 21, 35], and the proposed work.

The above discussion establishes that the proposed SUF has advantage over all other UFs. Moreover, when we compare the proposed shadow filter with its own family (i.e., with available shadow filters), it is found that report of only one CM SUF [35 (Fig. 10)] is available. The proposed SUF is better than [35 (Fig. 10)] in terms of the number of ABBs used and also the fact that all capacitors are grounded compared to one floating capacitor in [35 (Fig. 10)]. Thus, in comparison to [35 (Fig. 10)], the proposed SUF consumes less space and is suitable for integrated circuit implementation.

6 Simulation results of the proposed SUF

The validation of the proposed circuit is performed with Cadence Virtuoso Spectre in TSMC 180 nm CMOS technology parameters. The layout of the SUF from Fig. 8 is shown in Fig. 11, which occupies an area of 110.35 µm x 73.6 µm. The supply voltages for CCCTA and EX-CCCTA are ± 1.5 V. The bias voltage V_{BB} is -1 V and bias currents are $I_{B1} = I_{B2} = 56$ µA for CCCTA whereas bias currents for EX-CCCTA are $I_{C1} = 100$ µA and $I_{C2} = I_{C3} = 56$ µA. The aspect ratio of transistors is given in Table 1 and Table 3 for CCCTA and EX-CCCTA respectively. The calculated frequency of 20.02 MHz, quality factor of 0.95 and bandwidth of 21.07 MHz are obtained for C_1=C_2=1 pf from Eq. (15). The filter gain responses such as LP, HP, BP, and BR for both the pre-layout and post-layout simulations are shown in Fig. 12 (a). Fig. 12 (b) shows the pre-layout and post-layout time response of the BP output for the input current of 50 µA, 20 MHz. Simultaneously, the gain and phase responses of the AP filter are shown in Fig. 13. The pole frequencies of the proposed filter for the pre-layout and post-layout are obtained as 20.2 MHz and 19.9 MHz, respectively. The deviation of post-layout pole frequency from pre-layout frequency is primarily due to parasitic capacitances.

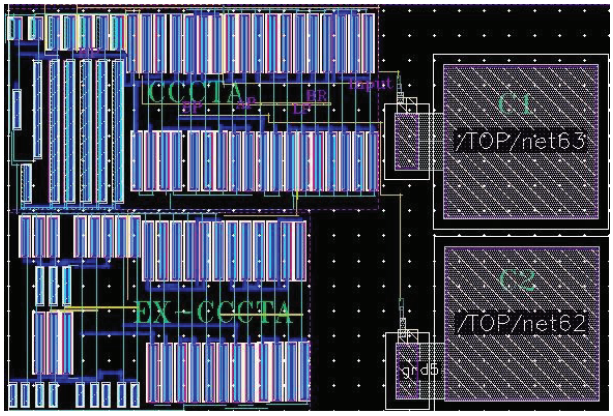

Figure 11: Layout of the proposed shadow universal filter (SUF) of Fig. 8.

The tunability of f_o by bias currents $I_{B1} = I_{B2}$ of CCCTA is shown in Fig. 14 for the SUF. The pre-layout simulated frequencies are obtained as f_o = 20.1 MHz, 37.6 MHz, and 53.5 MHz while the post-layout frequencies are obtained as f_o = 19.8 MHz, 37.01 MHz, and 53 MHz by varying the values of $I_{B1} = I_{B2}$ to 56 µA, 200 µA, and

Table 4: Comparative Study of available CM SIMO filters.

Ref.	No. and type of ABB used	Supply Voltage (V)	Passive elements (R,C)/ All grounded (Yes/N0)	Full cascadability	Filter functions/ Simulatneous responses (Yes/No)	Ease in independent adjustment of filter parameters fO and QO	Electronic tuning	Passive component matching constraint required	P.C. (mW)	Operating frequency (MHz)	S or NS filter
1.	4 CFTA	±3	2C / Yes	Yes	UF/ No	No	Yes	No	NA	0.153	NS
2.	2 CCCII, 1 MO-CCCA	±1.5	2C / Yes	Yes	UF/ Yes	Yes	Yes	No	NA	0.039	NS
3.	4 MO-OTA (Fig. 4)	±2	2C / Yes	No	UF/ Yes	Yes	Yes	Yes for UF realization	NA	0.238	NS
4.	3 DVCC	±2.5	4R, 2C/ Yes	No	UF/ Yes	No	No	Yes for UF realization	NA,	22.5	NS
8.	1 CFTA	±0.75	2C / Yes	No	LP, HP*, BP/ Yes	No	Yes	No	0.6	8	NS
9.	1 CCTA	±2	2R, 2C / Yes	No	UF*/ No	Yes	Yes	No	NA	1	NS
10.	3 DVCC, 6 MOS Resistor	±1.5	2C / Yes	Yes	UF/ No	Yes	No	Yes for UF realization	NA	16	NS
11.	2 OTA	NA	2C / Yes	No	UF/ Yes	No	Yes	No	NA	0.015	NS
12.	4 ZC-CFTA	±3	2C / Yes	Yes	UF/ Yes	Yes	Yes	No	12.2	0.159	NS
13.	2 ZC-CITA	NA	2C / Yes	Yes	UF/ Yes	No	Yes	No	NA	1.026	NS
14.	3 MOCCCII	±1.5	1R, 2C / Yes	No	UF/ Yes	No	Yes	No	NA	0.158	NS
15.	1 VDGA	±1	2R, 2C / No	No	LP, HP*, BP*/ Yes	No	Yes	No	1.49	1.59	NS
16.	2 EXCCTA	±1.25	4R, 2C / Yes	Yes	UF/ No	No	Yes	No	NA	7.62	NS
17.	3 DOCCCII (Fig. 2)	±2.5	2C / Yes	Yes	UF/ Yes	No	Yes	No	19.9	0.318	NS
	4 CCCII (Fig. 3)	±2.5	2C / Yes	Yes	UF/ Yes	No	Yes	No	NA	NA	NS
	3 CCCII (Fig. 4)	±2.5	2C / Yes	Yes	UF/ Yes	No	Yes	No	NA	NA	NS
18.	1 DXCCTA	±1.25	1R, 2C/ Yes	No	UF*/ Yes	No	Yes	No	NA	40	NS
19.	3 CCCII	±3	2C/ Yes	Yes	UF/ Yes	Yes	Yes	No	NA	0.127	NS
20.	3 ZC-CFTA	±1.5	2C/ Yes	Yes	UF/ Yes	Yes	Yes	No	NA	1.157	NS
21.	3 CCCII	±3	2C/ Yes	Yes	UF/ Yes	Yes	Yes	No	32	10	NS
22.	2 OTA, 1 CCIII	±1	1R, 2C/ Yes	Yes	UF/ Yes	Yes	Yes	No	NA	1	NS
23.	2 DVCC	±0.75	3R, 2C/ No	No	UF/ Yes	No	No	Yes for UF realization	0.81	3.18	NS
24.	1 VD-DXCC	±1.25	2R, 2C/ Yes	Yes	LP, HP, BP/ Yes	No	Yes	No	2.23	2.79	NS
25.	2 MO-OFC	±0.75	2R, 2C/ Yes	No	UF/ No	Yes	No	No	NA	1.5	NS
26.	BJT based	±2.7	2C/ Yes	NA	UF/ Yes	NA	Yes	No	4.93	0.1	NS
27.	1 VDTA	±1	1R, 2C/ Yes	No	UF*/ No	Yes	Yes	No	19	7	NS
28.	1 EXCCTA	±0.9	1R, 2C/ Yes	No	UF*/ No	No	Yes	No	NA	2.204	NS
29.	2 CDTA, 1TA	±1.8	1R, 2C/ Yes	No	LP*, BP/ Yes	Yes	Yes	No	21.2	9.95	S
	2 VDTA	±1.8	2C/ Yes	No	LP, BP*/ Yes	Yes	Yes	No	17.4	5.625	S
30.	2 CDTA	±1.8	2R, 2C, No	No	BP*/ Yes	No	No	No	7.79	4	S
31.	3 CDTA	±0.9	1R, 2C, Yes	No	LP, HP*, BP*/ Yes	No	Yes	No	5.9	15.1	S
32.	4 OFCC	±1.5	5R, 2C, Yes	Yes	BP/ Yes	Yes	No	No	NA	1.59	S
33.	2 CDTA, 1CA	±0.9	2C/ Yes	Yes	BP/ Yes	Yes	Yes	No	NA	1	S
34.	4 ECCII	±0.9	2R, 2C/ No	No	BP/ Yes	No	No	No	NA	19.05	S
35.	2 CC-CDCTA (Fig. 9)	±1.25	2C/ Yes	No	LP, HP*, BP/ Yes	Yes	Yes	No	1.5	79.8	S
	3 CC-CDCTA, 1 CCII (Fig. 10)	±1.25	2C/ No	Yes	UF/ Yes	Yes	Yes	No	2.23	79.8	S
Prop. Work	1 CCCTA, 1 EX-CCCTA	±1.25	2C/ Yes	Yes	UF/ Yes	Yes	Yes	No	4.1	20.02	S

*Indicates the obtained current signal for the respective response conducts through a grounded capacitor and/or resistor, hence additional circuitry is required for practical application; NA: Not available; PC: Power Consumption; Full Cascadability: Cascadable both at the input and output, S: Shadow; NS: Non-shadow; CA: Current amplifier

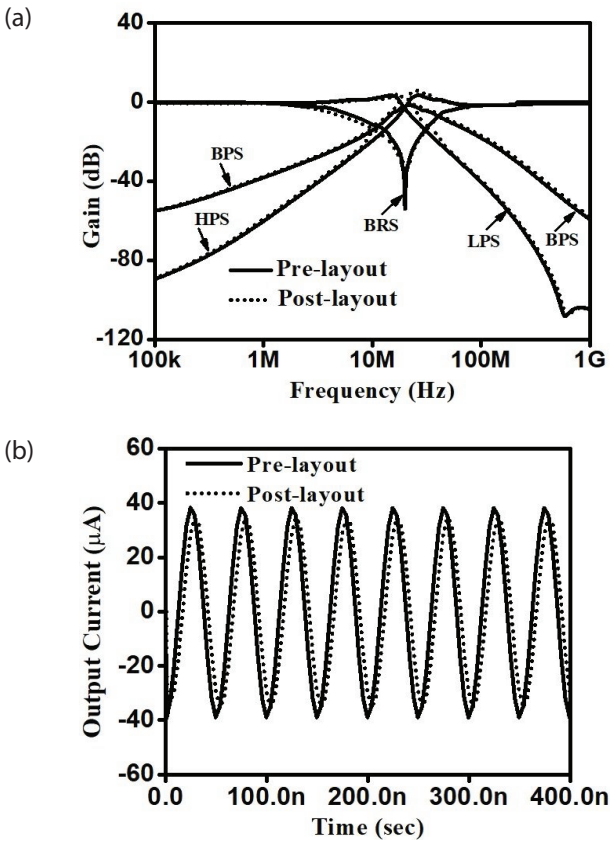

Figure 12: Simulated results (a) gain responses of the SUF for HP, LP, BP, and BR (b) time response of BP output..

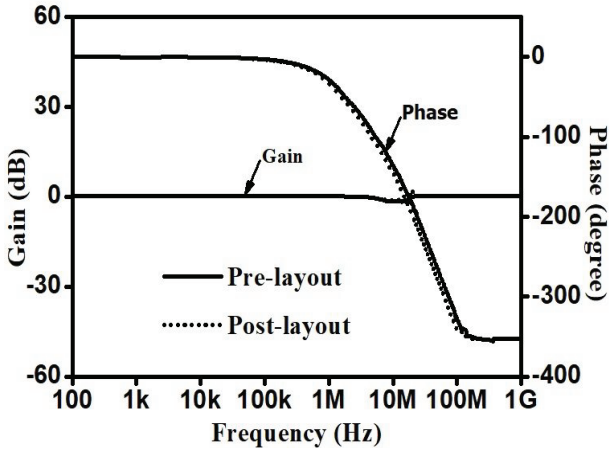

Figure 13: Simulated results of gain and phase response for the all-pass (AP) filter

400 μA, respectively. Whereas the calculated values of frequencies are 20.02 MHz, 37.8 MHz, and 53.49 MHz with a deviation of 1.09%, 2%, and 0.9%, respectively in comparison with post-layout frequencies, for the fixed quality factor. Similarly, the pre-layout simulated bandwidths are 19.7 MHz, 36.86 MHz, and 52.4 MHz vis-à-vis the calculated bandwidths of 20.02 MHz, 37.8 MHz, and 53.49 MHz, respectively. While the post-layout bandwidths are 19.22 MHz, 35.93 MHz, and 51.45 MHz with a deviation of 3.9%, 4.9%, and 3.8%, respectively.

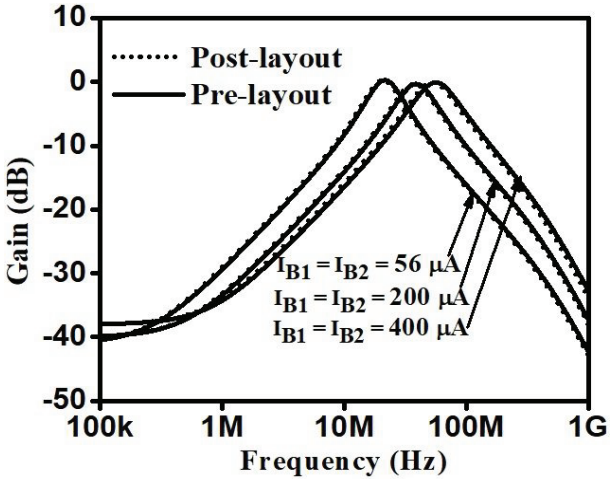

Figure 14: Simulated results of tuning of f_O by varying bias currents (I_{B1} & I_{B2}) of CCCTA for fixed Q_O.

Furthermore, as given in Eq. (15), f_o can also be tuned along with BW without changing the quality factor by varying C_1=C_2=C. The pre-layout simulated responses are shown in Fig. 15, resulting in f_o = 20.1, 9.9, and 2.48 MHz for the capacitor value of C_1=C_2 = 1 pF, 2 pF, and 8 pF, respectively while the post-layout frequencies are 19.62, 9.75, and 2.45 MHz, respectively. In contrast, the calculated results are obtained as 20.02, 10.01, and 2.5 MHz with a deviation of 1.9%, 2.5%, and 2%, respectively, for a fixed calculated quality factor of 1. Similarly, the pre-layout simulated bandwidths are 19.7 MHz, 9.7 MHz, and 2.45 MHz and the post-layout bandwidths are 19.23 MHz, 9.6 MHz, and 2.43 MHz for the calculated bandwidths of 20.02 MHz, 10.01 MHz 2.5 MHz, respectively, with a deviation of 3.9%, 4%, and 2.8%.

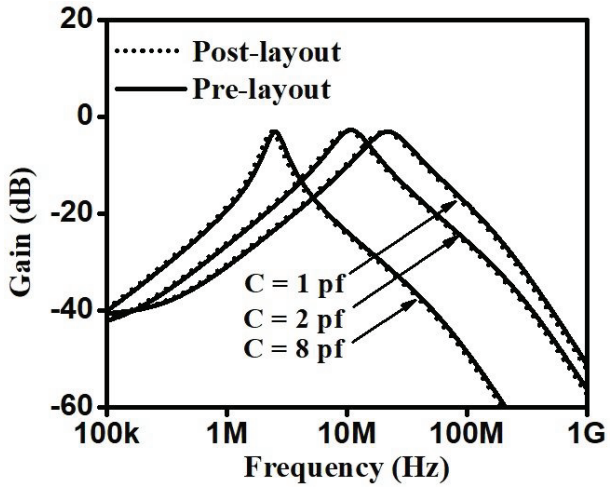

Figure 15: Simulated results of tuning of f_O by varying capacitance value C for fixed Q_O.

The tuning of the quality factor (Q_o) with A_1 (i.e., $g_{m1}^{(2)}$ or I_{C2} of EX-CCCTA) without changing f_o, as per Eq. (15), is validated in Fig. 16 for band pass response. The responses are obtained by varying bias current I_{C2} = 56, 200, and 400 µA of EX-CCCTA. The corresponding pre-layout simulated quality factors are obtained as Q_o = 1.58, 1.27, 0.96, the post-layout quality factors are obtained as Q_o = 1.6, 1.3, 0.97 vis-a-vis calculated values as 1.55, 1.25, 0.95 with a deviation of 3.2%, 4%, and 2.1% respectively.

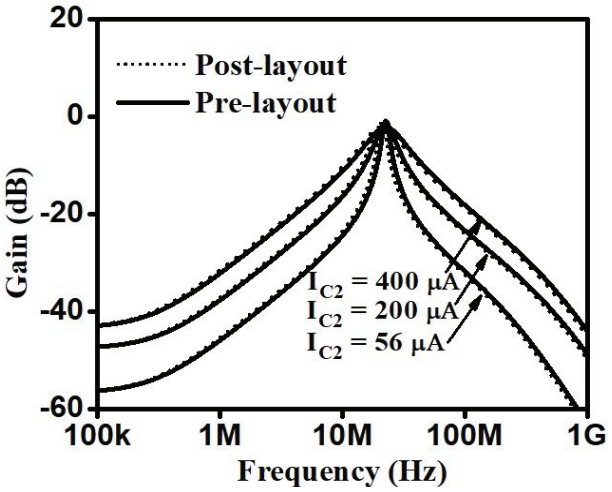

Figure 16: Simulated results of tuning of Q_o by varying A_1 with I_{C2} of EX-CCCTA for fixed f_o.

The tuning of the f_o and Q_o without disturbing BW by varying A_2 (i.e., $g_{m2}^{(2)}$ or I_{C3} of EX-CCCTA) is verified in Fig. 17. For the bias currents I_{C3} = 56, 200, 400 µA, the pre-layout simulated frequencies resulted in 19.8, 21.3, and 23.52 MHz while, the post-layout frequencies are 19.5, 20.9, and 23.2 MHz vis-à-vis the calculated frequencies of 20.02, 21.55, 23.55 MHz with a respective deviation of 2.5%, 3%, and 1.9%. Similarly, the pre-layout simulated quality factors are obtained as 0.94, 1.014, and 1.1 while the post-layout quality factors are 0.93, 1.01, and 1.09 for the calculated quality factors of 0.95, 1.022, and 1.117 with a deviation of 2.4%, 1.1%, 1.8%. The pre-layout and post-layout simulated BW was 21 MHz and 20.9, respectively vis-à-vis calculated BW of 21.07 MHz.

The measure of %THD (Total Harmonic Distortion) for the HP and LP responses as a function of the input signal is given in Fig. 18. It is observed that %THD is low up to 1 mA. The intermodulation distortion (IMD) for the BP filter is simulated using the sinusoidal input signal of 100 µA, 10 MHz with an addition of parasitic sinusoidal signal of 10 µA for the respective frequencies as given in Table 5. The output noise of the BP filter has also been studied, as shown in Fig. 19. The pre-layout and post-layout noise of the shadow filter is 21 aA^2/Hz and 21.4 aA^2/Hz at 1 Hz, and after that, it decays exponentially. Eq. (35) gives the calculation of dynamic range, where the graphical integration of the squared spectrum is obtained from Fig. 19 and the maximum linear swing of the output ($I_{OL,\,max}$), approximately 180 µA and 176 µA, are obtained from Fig. 20 for the pre-layout and the post-layout respectively. The resulted pre-layout and post-layout dynamic ranges are 75.6 dB and 71.5 dB, respectively.

$$Dynamic\ Range = 20 * log_{10} \frac{I_{OL,\,max}}{\sqrt{Int.of\ squared\ spectrum}} \quad (35)$$

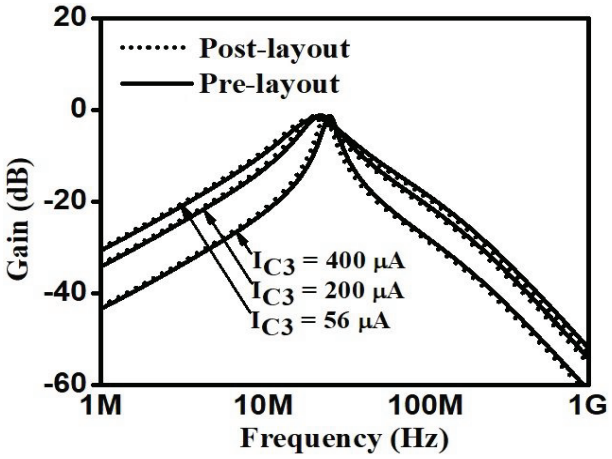

Figure 17: Simulated results of tuning of f_o and Q_o by varying A_2 with I_{C3} of EX-CCCTA.

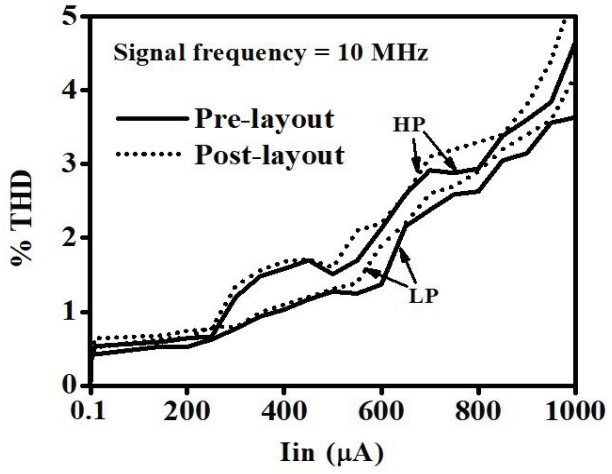

Figure 18: %THD Variation of HP and LP filter.

Table 5: IMD results for the band pass filter.

Frequency for the parasitic signal (MHz)	1	5	8	10	15	18	20	25
% THD	1.61	0.74	1.26	1.68	1.17	1.73	2.91	2.45

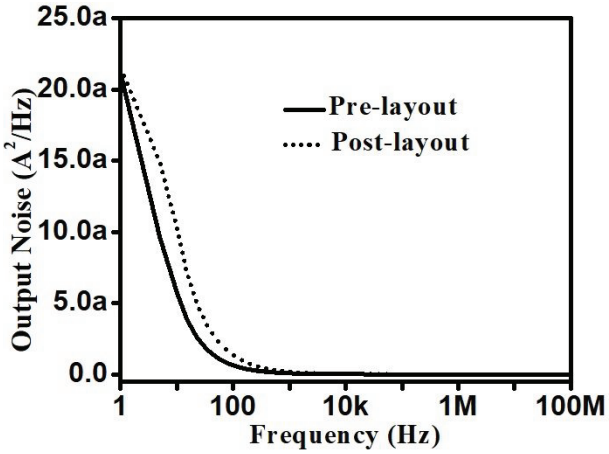

Figure 19: Output noise for the BP.

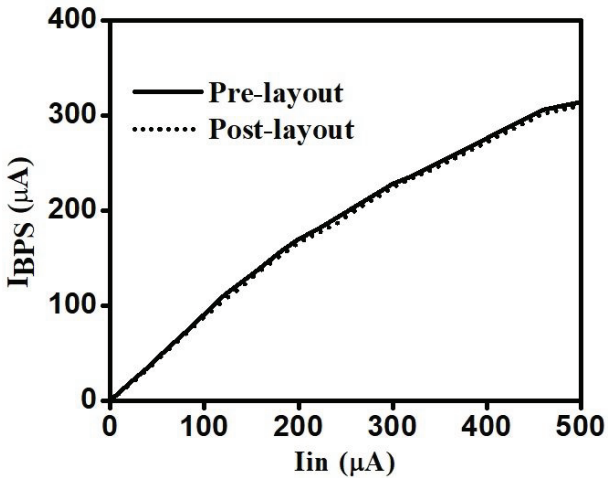

Figure 20: Transfer linearity test for BP output signal.

7 Conclusions

This paper started with presenting two new active building blocks, CCCTA and EX-CCCTA, which are the modified versions of CCTA and EX-CCCII, respectively. The proposed SUF uses only two grounded capacitors and no resistor. It is free from any matching constraints. All the standard responses such as LP, BP, HP, BR, and AP are obtained simultaneously without altering the SUF circuit. It provides the possibility to orthogonally adjust the pole frequency and the quality factor in comparison to NSUF. Moreover, the electronic tuning of filter's various parameters can be performed conveniently. Input and output impedances are low and high, respectively, which makes the filter fully cascadable. Power consumption is found to be low compared to most of the filters in available literature. The theoretical results were verified with post layout simulation in Cadence Virtuoso using TSMC 180 nm technology.

8 Conflict of interest

The authors declare that there is no conflict of interest for this paper. Also, there are no funding supports for this manuscript.

9 References

1. W. Tangsrirat, "Single-input three-output electronically tunable universal current-mode filter using current follower transconductance amplifiers," AEU-Int. J. Electron. Commun., vol. 65, n0. 10, pp. 783-787, Oct. 2011, https://doi.org/10.1016/j.aeue.2011.01.002.
2. C. Wnag, J. Xu, A. U. Keskin, S. Du, and Q. Zhang, "A new current-mode current-controlled SIMO type universal filter," AEU-Int. J. Electron. Commun., vol. 65, n0. 3, pp. 231-234, Mar. 2011, https:doi.org/10.1016/j.aeue.2010.02.010.
3. D. V. Kamat, P. V. A. Mohan, and K. G. Prabhu, "Novel first-order and second-order current-mode filters using multiple-output operational transconductance amplifiers," Circuits Systems and Signal Processing, vol. 29, pp. 553-576, Mar. 2010, https://doi.org/10.1007/s00034-010-9163-y.
4. M. A. Ibrahim, S. Minaei, and H. A. Kuntman, "22.5 MHz current-mode KHN-biquad using differential voltage current conveyor and grounded passive elements," AEU-Int. J. Electron. Commun., vol. 59, no. 5, pp. 311-318, Jul. 2005, https://doi.org/10.1016/j.aeue.20o4.11.027.
5. Y. Lakys, and A. Fabre, "Shadow filters-new family of second order filters," Electronics Letters, vol. 46, no. 4, pp. 276-277, Feb. 2010, https://doi.org/10.1049/el.2010.3249.
6. Y. Lakys, and A. Fabre, "Shadow filter generalization to nth class," Electronics Letters, vol. 46, no. 14, pp. 985-986, Jul. 2010, https://doi.org/10.1049/el.2010.0452.
7. V. Biolkova, D. A. Biolek, "Shadow filters for orthogonal modification of characteristic frequency and bandwidth," Electronics Letters, vol. 46, no. 12, pp. 830-831, Jun. 2010.
8. S. V. Singh, R. S. Tomar, and D. S. Chauhan, "Single CFTA based current-mode universal biquad filter," The Journal of Engineering Research, vol. 13, no. 2, pp. 172-186, May 2016, https://doi.org/10.24200/tjer.vol13iss2pp172-186
9. N. Herencsar, J. Koton, and K. Vrba, "Single CCTA-based universal biquadratic filters employing minimum components," International Journal of Computer and Electrical Engineering, vol. 1, no.3, pp. 307-310, Aug. 2009.

10. S. Minaei, and M. A. Ibrahim, "A mixed-mode KHN-biquad using DVCC and grounded passive elementssuitable for direct cascading," International Journal of Circuit Theory and Applications, vol. 37, pp. 793-810, https://doi.org/10.1002/cta.493.
11. A. Qadir, and T. Altaf, "Current mode canonic OTA-C universal filter with single input and multiple outputs," In: Proceedings of International Conference on Electronic Computer Technology (ICECT' 10), pp. 32-34, Jun. 2010, https://doi.org/10.1109/ICECTECH.2010.5479995.
12. J. Satansup, and W. Tangsrirat, "Single-input five-output electronically tunable current-mode biquad consisting of only ZC-CFTAs and grounded capacitors," Radioengineering, vol. 20, no. 3, pp. 650-656, Sep. 2011.
13. D. Biolek, V. Biolkova, Z. Kolka, and J. Bajer, "Single-input multi-output resistorless current-mode Biquad," In: Proceedings of IEEE European Conference on Circuit Theory and Design, pp. 225-228, Oct. 2009, https://doi.org/10.1109/ECCTD.2009.5274928.
14. R. Senani, V. K. Singh, A.K. Singh, D.R. Bhaskar, "Novel electronically controllable current-mode universal biquad filter," IEICE Electron Express 1, vol. 1, no. 14, pp. 410-415, Oct. 2004, https://doi.org/10.1587/elex.1.410.
15. W. Tangrirat, T. Pukkalanun, and O. Channumsin, "Single VDGA-based dual-mode multifunction biquadratic filter and quadrature sinusoidal oscillator," Informacije MIDEM, vol. 50, no. 2, pp. 125-136, 2020, https://doi.org/10.33180/InfMIDEM2020.205.
16. M. I. A. Albrni, F. Mohammed, N. Herencsar, J. Sampe, and S. H. M. Ali, "Novel electroniacally tunable biquadratic mixed mode universal filter capable of operating in MISO and SIMO configurations," Informacije MIDEM, vol. 50, no. 3, pp. 189-203, 2020, https://doi.org/10.33180/InfMIDEM2020.304
17. E. Yuce, "Current-mode electronically tunable biquadratic filters consisting of only CCCIs and grounded capacitors," Microelectronics Journal, vol. 40, no. 12, pp. 1719-1725, Dec. 2009, https://doi.org/10.1016j.mejo.2009.09.002.
18. A. Kumar, B. Chaturvedi, "Novel CMOS dual-X current conveyor transconductance amplifier realization with current-mode multifunction filter and quadrature oscillator," Circuits Systems and Signal Processing, vol. 37, pp. 2250-2277, Oct. 2017, https://doi.org/10.1007/s00034-017-0680-9.
19. M. Kumngern, "A new current-mode universal filter with single-input five-output using translinear current conveyors," Australian Journal of Eectrical and Electronics Engineering, vol. 9, no. 2, pp. 177-184, Sep. 2015, https://doi.org/10.1080/1448837X.2012.11464322
20. B. Singh, A. K. Singh, and R. Senani, "New universal current-mode biquad using only three ZC-CFTAs," Radioengineering, vol. 21, no. 1, pp. 273-280, Apr. 2012.
21. M. Kumngern, P. Phasukkit, S. Junnapiya, F. Khateb, and S. Tugjitkusolmun, "ECCCII-based current-mode universal filter with orthogonal control of w_o and Q," Radioengineering, vol. 23, no. 2, pp. 687-696, Jun. 2014.
22. T. S. Arora, M. Gupta, S. Gupta, "Current mode universal filter employing operational transconductance amplifier and third generation current conveyor," In: IEEE International Conference on Power Electronics, Intelligent Control and Energy Systems (ICPEICES), IEEE, pp. 1-4, Feb. 2017, https://doi.org/10.1109/ICPEICES.2016.7853305.
23. A. Abaci, and E. Yuce, "A new DVCC+ based second-order current mode universal filter consisting of only grounded capacitors," Journal of Circuits Systems and Computers, vol. 26, no.9, pp. 1750130, Feb. 2017, https://doi.org/10.1142/S0218126617501304.
24. M. A. Albrni, M. Faseehuddin, J. Sampe, and S. H. M. Ali, "Novel dual mode multifunction filter employing highly versatile VD-DXCC," Informacije MIDEM, vol. 49, no. 3, pp. 169-176, 2019, https://doi.org/10.33180/InfMIDEM2019.305.
25. T. Praveen, "OFC based high output impedance current mode SIMO universal biquadratic filter," In: International Conference on Multimedia Signal Processing and Communication Technologies (IMPACT), IEEE, pp. 134-136, Feb. 2012, https://doi.org/10.1109?MSPCT.2011.6150456
26. R. Arslanalp, E. Yuce, and T. A. Tola, "Two lossy integrator loop based current-mode electronically tunable universal filter employing only grounded capacitors," Microelectronics Journal, vol. 59, pp. 1-9, Jan. 2017, https://doi.org/10.1016/j.mejo.2016.11.005.
27. D. Prasad, D. R. Bhaskar, and M. Srivastava, "Universal current-mode biquad filter using a VDTA," Circuits and Systems, vol. 4, pp. 29-33, Jan. 2013, https://dx.doi.org/10.4236/cs.2013.41006.
28. M. Faseehuddin, J. Sampe, S. Shireen, S. H. M. Ali, "Lossy and lossless inductance simulators and universal filters employing a new versatile active block," Informacije MIDEM, vol. 48, no. 2, pp. 97-113, 2018.
29. N. Pandey, A. Sayal, R. Choudhary, and R. Pandey, "Design of CDTA and VDTA based frequency agile filters," Advances in Electronics, vol. 2014, pp. 1-14, Dec. 2014, https://doi.org/10.1155/2014/176243.

30. N. Pandey, R. Pandey, R. Choudhary, A. Sayal, and M. Tripathi, "Realization of CDTA based frequency agile filters," IEEE International Conference on Signal Processing, Computing and Control, pp. 1-8, Nov. 2013, https://doi.org/10.1109/ISPCC.2013.6663403.
31. M. Atasoyu, H. Kuntman, B. Metin, N. Herencsar, and O. Cicekoglu, "Design of current-mode class 1 frequency agile filter employing CDTAs," European Conference on Circuit Theory and Design, pp. 1-4, Oct. 2015, https://doi.org/10.1109/ECCTD.2015.7300066.
32. D. Nand, and N. Pandey, "New configuration for OFCC-based CM SIMO filter and its application as shadow filter and its application as shadow filter," Arabian Journal for Science and Engineering, vol. 43, no. 6, pp. 3011-3022, June. 2018, https://doi.org/10.1007/s13369-017-3058-1.
33. A. Yesil, and F. Kacar, "Band-pass filter with high quality factor based on current amplifier," AEU-Int. J. Electron. Commun., vol. 75, pp. 63-69, May 2017, https://doi.org/10.1016/j.aeue.2017.03.007.
34. M. Atasoyu, B. Metin, H. Kuntman, and N. Herencsar, "New current-mode class 1 frequency-agile filter for multi-protocol GPS application," Elektronica ir Elektrotechnika, vol. 21, no. 5, pp. 35-39, May 2015, https://doi.org/10.5755/j01.eee.21.5.13323.
35. D. Singh, and S. K. Paul, "Realization of current mode universal shadow filter," AEU-Int. J. Electron. Commun., vol. 117, pp. 1-16, Apr. 2020, https://doi.org/10.1016/j.aeue.2020.153088
36. F. Khateb, W. Jaikla, T. Kulej, M. Kumngern, and D. Kubanek, "Shadow filters based on DDCC," IET Circuits Devices Syst., vol. 11, pp. 631-637, Oct. 2017, https://doi.org/10.1049/iet-cds.2016.0522.
37. S. C. Roy, "Shadow filters: a new family of electronically tunable filters," IETE J. Edu., vol. 51, pp. 75-78, Sep. 2014, https://doi.org/10.1080/09747338.2010.10876070
38. M. T. Abuelma'atti, N. R. Almutairi, "New current-feedback operational amplifier based shadow filters," Analog Integr. Circ. Sig. Process., vol. 86, pp. 471-480, Jan. 2016, https://doi.org/10.1007/s10470-016-0691-7.
39. M. T. Abuelma'atti, N. Almutairi, "New voltage-mode bandpass shadow filters," In: 13th International multi-conference on systems, signals & devices, pp. 412-415, May 2016, https://doi.org/10.1109/SSD.2016.7473695.
40. M. T. Abuelma'atti, N. Almutairi, "New CFOA-based shadow bandpass filters," In: 15th International conference on electronics information, and communications, Sep. 2016, https://doi.org/10.1109/ELINFOCOM.2016.7562969.
41. R. Anurag, R. Pandey, N. Pandey, M. Singh, and M. Jain, "OTRA based shadow filters," Annual IEEE India Conference, Mar. 2016, https://doi.org/10.1109/INDICON.2015.7443524.
42. P. Huaihongthong, A. Chaichana, P. Suwanjan, S. Siripongdee, W. Sunthonkanokpong, P. Supavarasuwat, W. Jaikla, and F. Khateb, "Single-input multiple-output voltage-mode shadow filter based on VDDDAs," AEU-Int. J. Electron. Commun., vol. 103, pp. 13-23, May 2019, https://doi.org/10.1016/j.aeue.2019.02.013.
43. A. Yesil, F. Kacar, and S. Minaei, "Electronically controllable bandpass filters with high quality factor and reduced capacitor value: an additional approach," AEU-Int. J. Electron. Commun., vol. 70, pp. 936-943, Jul. 2016, https://doi.org/10.1016/j.aeue.2016.04.009.
44. T. Thosdeekoraphat, S. Summart, C. Saetiaw, S. Santalunai, and C. Thogsopa, "CCCTAs based current-mode quadrature oscillator with high output impedances," International Journal of Electronics and Electrical Engineering, vol. 1, no. 1, pp. 52-56, Jan. 2013.
45. D. Agrawal, and S. Maheshwari, "Current mode filters with reduced complexity using a single EX-CCCII," AEU-Int. J. Electron. Commun., vol. 80, pp. 86-93, Oct. 2017, https://doi.org/10.1016/j.aeue.2017.06.025.

Arrived: 14. 11. 2021
Accepted: 04. 03. 2022

Informacije MIDEM
Journal of Microelectronics,
Electronic Components and Materials
Vol. 52, No. 1(2022), 67 – 67

MIDEM 2022

57th INTERNATIONAL CONFERENCE ON MICROELECTRONICS, DEVICES AND MATERIALS WITH THE WORKSHOP ON ENERGY HARVESTING: MATERIALS AND APPLICATIONS

September 14th – September 16th, 2022
Hotel City, Maribor, Slovenia

Announcement and Call for Papers

Chairs:

Prof. Dr. Tadej Rojac
Assist. Prof. Dr. Mojca Otoničar

IMPORTANT DATES

Abstract submission deadline:
May 1, 2022

Acceptance notification:
June 15, 2022

Full paper submission deadline:
July 31, 2022

Invited and accepted papers will be published in the Conference Proceedings.

Detailed and updated information about the MIDEM Conferences, as well as for paper preparation can be found on

http://www.midem-drustvo.si//

MIDEM

GENERAL INFORMATION

The 57th International Conference on Microelectronics, Devices and Materials with the Workshop on Energy harvesting: materials and applications continues a successful tradition of the annual international conferences organised by the MIDEM Society, the Society for Microelectronics, Electronic Components and Materials. The conference will be held in **Hotel City, Maribor, Slovenia** from **SEPTEMBER 14th – 16th, 2022**.

Topics of interest include but are not limited to:

- Energy harvesting: modelling, materials, devices,
- Novel monolithic and hybrid circuit processing techniques,
- New device and circuit design,
- Process and device modelling,
- Semiconductor physics,
- Sensors and actuators,
- Electromechanical devices, microsystems and nanosystems,
- Nanoelectronics,
- Optoelectronics,
- Photovoltaic devices,
- Electronic materials science and technology,
- New electronic materials and applications,
- Materials characterization techniques,
- Reliability and failure analysis,
- Education in microelectronics, devices and materials.

ORGANIZER:
MIDEM Society - Society for Microelectronics, Electronic Components and Materials, Slovenia

CO-ORGANIZER:
Republic of Slovenia, Ministry of Economic Development and Technology
European Union, European Regional Development fund

CONFERENCE SPONSORS: UL FE, UL FS, IJS, IMAPS, Slovenia Chapter; IEEE, Slovenia Section

Boards of MIDEM *Society* | *Organi društva* MIDEM

MIDEM *Executive Board* | *Izvršilni odbor* MIDEM

Supervisory Board | Nadzorni odbor

Court of honour | Častno razsodišče

Informacije MIDEM
Journal of Microelectronics, Electronic Components and Materials
ISSN 0352-9045

Publisher / Založnik:
MIDEM Society / Društvo MIDEM
Society for Microelectronics, Electronic Components and Materials, Ljubljana, Slovenia
Strokovno društvo za mikroelektroniko, elektronske sestavne dele in materiale, Ljubljana, Slovenija

www.midem-drustvo.si